FRIEDRICH-ALEXANDER
UNIVERSITÄT
ERLANGEN-NÜRNBERG
TECHNISCHE FAKULTÄT

Institute of Micro- and Nanostructure Research

In situ heating and combined electrical measurements: Principle, setup and correlative workflow

Bachelor Thesis

Submitted by
Julian Kauth

Supervisors
Lilian Vogl, M.Sc.
Prof. Dr. rer. nat. habil. Erdmann Spiecker

Friedrich-Alexander-Universität Erlangen-Nürnberg
Department of Materials Science and Engineering
Institute of Micro- and Nanostructure Research
Interdisciplinary Center for Nanostructured Films (IZNF)
Prof. Dr. rer. nat. habil. Erdmann Spiecker

Erlangen, September 28, 2020

CENEM
Center for Nanoanalysis and Electron Microscopy

GRK 1896
in situ microscopy

Abstract

The major contribution to power consumption in microelectronic devices is due to the internal resistance of interfaces and conducting wires. Metallic thin film deposition is used to create such wires and interconnects, but has some disadvantages. Wth the help of novel processing routines, the performance of metallic conductive pathways can be greatly improved.

The goal of this study is to investigate the influence of the microstructure – especially the grain size and thin film morphology – on the electrical conductivity of thin metal films and how their impacts change in response to heat treatment. A thin metal film is deposited onto an isolating substrate and the grain size, as well as the resistivity is measured in the as deposited state. Several samples are then heated to different temperatures and investigated in regards to their grain size, grain orientation, area coverage and resistivity. The results are correlated and an optimal heating duration is determined.

To get an *in situ* insight into the microstructure during heating, a program was developed to measure, record and display the change in resistance while heating. The heating process was recorded using a light microscope and the thin films were analysed *ex situ* with electron microscopy after heat treatment. Grain sizes were measured using the line intersect method on images taken via electron microscopy, grain orientation was determined using electron backscatter diffraction, the area coverage was calculated from the recorded *in situ* light microscopy video, and the resistivity was measured with a four point measurement before and after heating. These measures were analysed with regard to their influence on conductivity. The highest impact is contributed by the interplay between grain growth and dewetting. An optimum in conductivity is formed between the two extremes of a thin film with small grains and a high resistivity due to grain boundary scattering and a dewetted thin film consisting of monocrystalline, but disconnected particles. This was proven with our measurements and shows that an improvement in resistance is achievable for thin metal films with a simple heat treatment, reducing the loss of energy in the conductive pathways of micro electronics. More

research could also enable an easy way to manufacture transparent electrodes by controlling the dewetting process more precisely, forming a percolated, but transparent network of metal bridges instead of isolated particles after heating.

Contents

1 Introduction

Thin metal films are used in a wide range of applications today, as functional materials, such as ferroelectric materials in high frequency electronics [1], actuators in micro-electro-mechanical systems [2] or chemical sensors [3], as conductors in microelectronics and as transparent conductive electrodes in solar cells [4,5,6,7,8].

As such, the study of thin metal films can improve performance or longevity of these devices. Due to their large surface area when compared to their volume, thin films tend to form particles at temperatures well below the melting point of the bulk material. This phenomenon is called solid-state dewetting [9] and can lead to device failure during manufacturing or operation of a device that incorporates such thin films. However, elevated temperatures also lead to grain growth, which in turn improves the electrical conductivity [10, 11]. If the heat treatment is well controlled however, it can improve the conductivity and alter the thin film morphology. To optimize the conductivity of thin films it is therefore of interest to find the best heat treatment to reach this conductivity without making the thin film discontinuous, or – in the case of a transparent conductive electrode – to find the right tradeoff between conductivity [12] and transmissivity [13].

The dewetting process during heat treatment is analyzed with *in situ* light microscopy and correlative, *ex situ* scanning electron microscopy is used to study the grain size of the area imaged with the light microscope. To complete the study, transmission electron microscopy provides a close look at the microstructure, which reveals defects like twin grain boundaries after heat treatment. Moreover, correlative *in situ* electrical measurements are used to study the relationship between electrical behavior and grain size of the thin gold films and an *in situ* measurement setup for conductivity changes during heating is established.

Using this setup of *in situ* and correlative microscopy methods, the interplay of the different factors is studied and the thin film is optimized in regard to its conductivity. The best grain size is determined for a chosen thin film thickness and heat treatment.

A representation of the workflow is summarized in figure 1.1. To get a reference value before heat treatment of the deposited metal layer, the conductivity of the sample is determined via four point measurement. During heat treatment in the light microscopy stage, the *in situ* two point setup is used to display and analyse the relative conductivity changes. After the heating process a four point measurement is performed again. The combination of the different measurements allows for an overall characterisation and comparison of the electrical data. Additionally, correlative electron microscopy is used to complement the microstructural analysis.

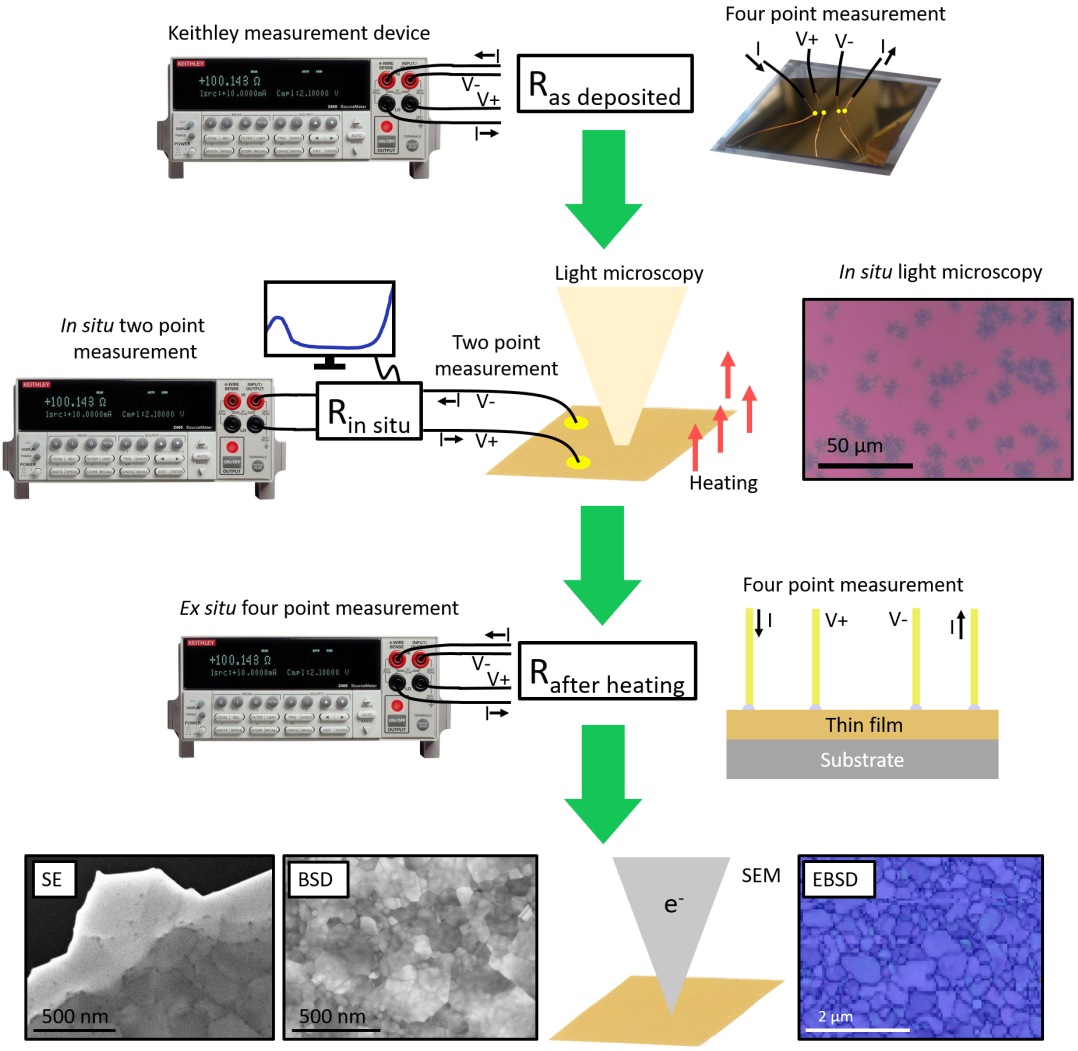

Figure 1.1: Workflow of this thesis. A thin gold film was deposited and studied in regards to its resistivity. After heating to a certain temperature, the layer is quickly cooled off and the grain size, grain orientation, area coverage, and resistivity are determined.

2 Background

In this chapter the theoretical background will be explained. An overview of percolation theory will be given and the mechanisms behind solid state dewetting are explained. After a short look at the method used to deposit the thin gold films that are studied in this work, different electrical measurement techniques are explained.

2.1 Percolation theory - conductive pathways

In order to conduct electricity between two points in a conductive thin film on an isolating substrate a path needs to exist between those two points to allow charge carriers to flow through. When the thin film is continuous with no holes, the electrons are free to move and the thin film is conductive. When the free movement is restricted – e.g. by a change in the morphology of the thin film – the conductivity decreases. With increasing hole density and hole size a point will be reached at which no conductive path exists and therefore the thin film will become non-conductive. To prevent the sudden loss of conductivity due to depercolation it is important to quantify the effect of hole growth on the electrical properties and to determine how much area needs to be covered in order to optimize the thin film for good conductivity.

This is the topic of Percolation Theory [14]. A modern use case is the study of conductive pathways in electrical devices. Next to thin films this topic is also interesting for electrodes made of different materials, e.g. metal nanowires [6,15,16]. The trade off between conductivity and transmissivity is an important balance to strike, in order to construct the most efficient electrode possible. An example of a conductive, percolated film and a discontinuous, non-conductive film can be seen in figure 2.1. The top row shows *ex situ* electron microscopy images of a heated film, the bottom row shows the corresponding schematic. The images follow the development from a continuous, conductive film (image 2.1**(a)**) to a discontinuous, non-conductive state (image 2.1**(c)**).

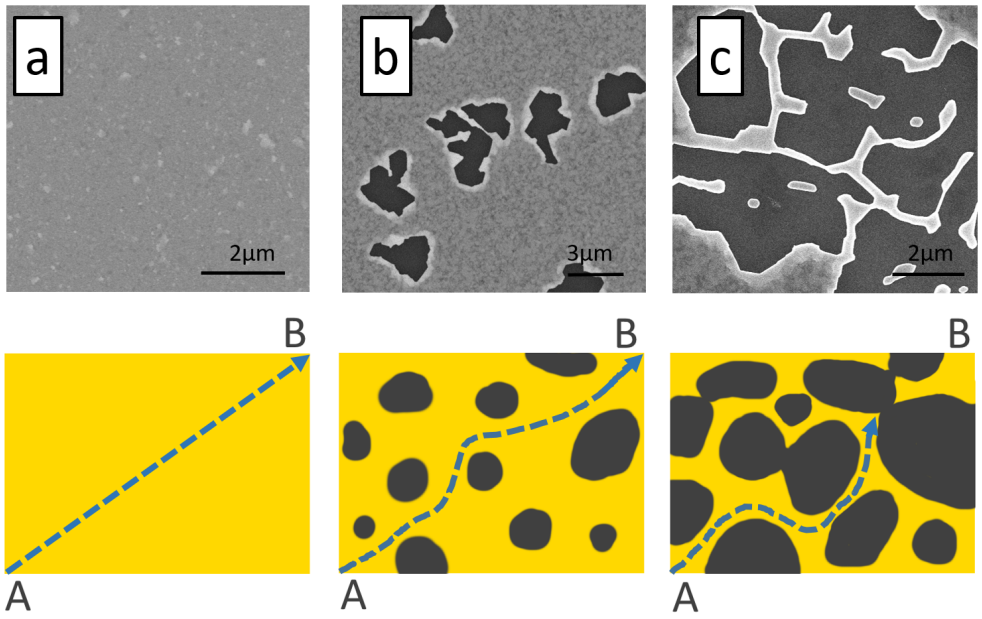

Figure 2.1: Example of a conductive, percolated film on the left and a non-conductive, non continuous film on the right. Bottom figures show the schematic development of the thin film during heating, the blue arrow illustrates the loss of conductivity. The top images are experimental images, taken with a Scanning Electron Microscope after heat treatment.

2.2 Solid-state dewetting

Wetting is the process of a substance covering the surface of another structure [17, 18]. Dewetting describes the exact opposite process, when a continuous film breaks up and no longer covers the full surface. While the process of dewetting is usually known for a liquid on a solid surface, when it comes to nanometer sized structures this phenomenon can also be seen with solid thin films on a solid surface [9]. If the temperature is sufficiently high to allow for long distance material migration [19, 20] the thin film will transform into small particles, even at temperatures below its melting point. Since the dewetting material is a solid rather than a liquid, the process is called *solid-state dewetting*. A sketch of that process can be seen in figure 2.2**(a)**. Images below show the corresponding light microscopy (figure 2.2**(b)**) and electron microscopy (figure 2.2**(c)**) images. The

images depict the development from the continuous film on the left, to a partially continuous, partially dewetted layer in the center and the fully dewetted particles on the underlying substrate on the right.

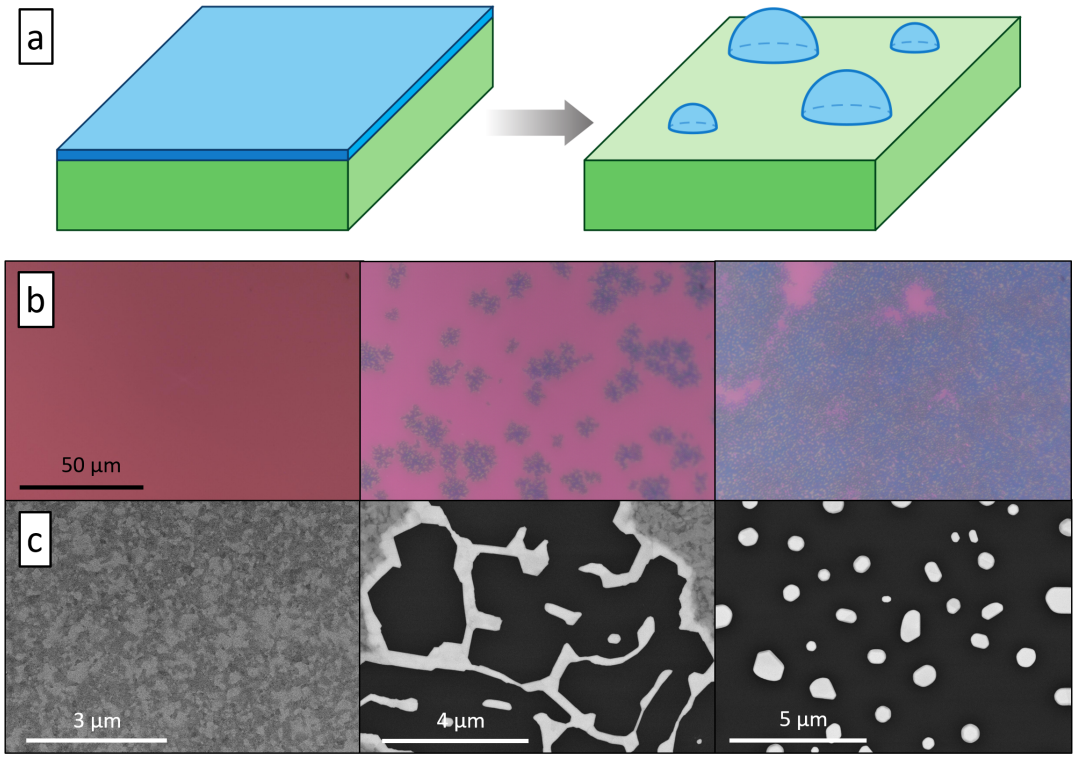

Figure 2.2: ***(a)****: Sketch of the dewetting process [9]. Example images of the dewetting process of a* 20 nm *thin gold film on a silicon oxide substrate are displayed underneath.* ***(b)****: The process as seen under the light microscope.* ***(c)****: Scanning electron microscopy images of the changing thin film morphology during dewetting.*

The driving force behind this phenomenon is the surface energy of the thin film as well as the interfacial energy between the cover and the substrate. The higher the surface energy, the less stable the film [9].

On a continuous film the process of dewetting begins with the formation of holes. In a polycrystalline material the atoms at grain boundaries have a higher energy than those within grains. When the thin film is heated to high temperatures those atoms diffuse away from the energetically unfavorable places at grain

boundaries and move to and along the interfaces of the film [9].

The movement of atoms away from grain boundary junctions and other high energy positions causes local thinning of the thin film. If enough material is moved away, a hole is formed. Material is further transported away from the hole due to the curvature at the edge. Capillary forces deform the film material further, causing the hole to grow. Due to capillary instabilities the retracting edge forms a rim which will eventually be separated from the continuous thin film [21] and leave isolated particles on the substrate [9, 22].

2.3 Electron beam physical vapor deposition process

There are two general ways to create nanoscale materials: bottom up and top down [23]. A top down process begins with a large piece of material that is treated to break up into smaller pieces repeatedly until the desired size is reached, while the bottom up process builds up the nanomaterial from atoms or molecules.

The bottom up process is advantageous for thin film development because it enables covering a large surface and at the same time gives fine control over the thickness and structure of the deposited material. Several types of bottom up processes are available for thin film development, like Atomic Layer Deposition [24] and Sputter Deposition [25]. For this project an Electron Beam Physical Vapor Deposition (E-Beam PVD) method was used [26].

A sketch of the system can be seen in figure 2.3. The E-Beam PVD works by heating the material that is to be deposited, using an electron beam to introduce energy. In the vacuum chamber the material is free to evaporate and is not stopped by gas molecules on its way away from the source. It is then deposited on the substrate that is positioned opposite of the crucible.

The E-Beam PVD was chosen for this work due to the fine grain structure that is produced in the process. This makes it possible to study the development of grain growth during the following heating experiments. Additionally, the thin films are continuous at a very low film thickness and a minimal surface roughness increases the conductivity of thin films [27, 28, 29].

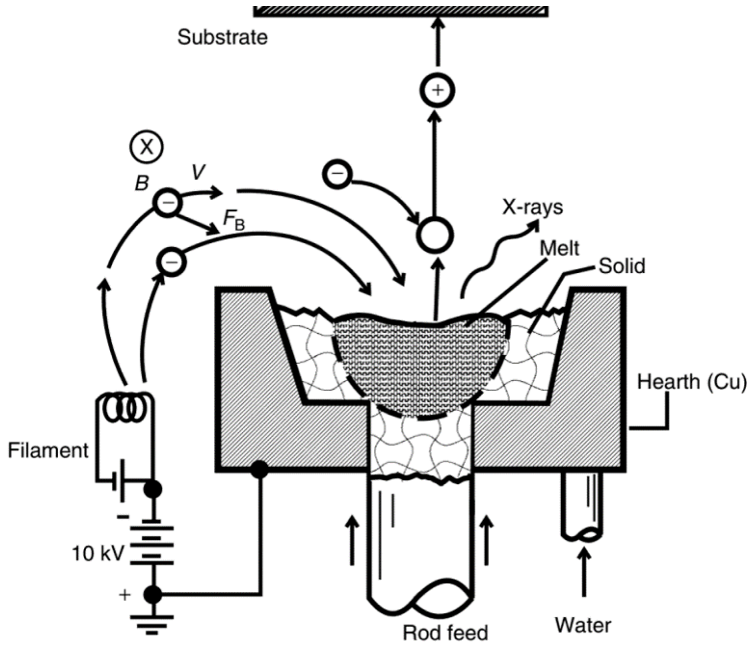

Figure 2.3: Sketch of an Electron Beam Physical Vapor Deposition system. The source material is heated by bombardment with highly energetic electrons. The evaporated material condenses on the substrate placed above [26].

2.4 Electrical measurement

Electrical conductivity is an important material property for many applications, as it determines the amount of energy lost as heat when conducting electricity through that material. To determine the electrical resistance of a material UI curves are required. For this measurement current is passed through the sample and both the current I and the voltage U are recorded. According to Ohm's law the resistance is then given via equation 2.1 [30]. This assumes a steady state of electron flow and the resistance to be constant – in regards to the applied voltage, applied current and for the duration of the measurement. If the resistance is not constant, either with regards to the applied voltage, to the forced current, or if a measurement is performed for longer periods of time, a modified version of the equation has to be used [31]. The derived version can be seen in equation 2.2 and is called *differential resistance*.

$$R = \frac{U}{I} \tag{2.1}$$

$$R_{diff} = \frac{dU}{dI} \tag{2.2}$$

where :

R = resistance

U = voltage

I = current

R_{diff} = resistance at a certain point on the voltage-current plot

dU = a small change in the applied voltage

dI = a small change in the measured current flow

The principle setup for a resistance measurement can be seen in figure 2.4**(a)**, which shows the two probes contacting the sample. A voltage is applied trough the probes and the current measured. This method is called a two point measurement and is the simplest way to measure resistance. It has one significant drawback because the resistance of the probes, the contact resistance between probes and sample, and the resistance of the wires to and from the measurement device are also included in the measurement. This setup is therefore inadequate to measure small resistances accurately. However, for *in situ* techniques the relative change in resistance can be easily measured with this method.

One way to work around that restriction is the the four point measurement. It uses four contact points instead of two. According to Ohm's law, a conductive material that is in a steady state of current flow only shows a drop in voltage if current is flowing between the two points of measurement. When only two probes are available to contact the sample, the current runs through the two tips that also measure the voltage and the aforementioned parasitic resistances are therefore always included in the measurement. With four probes it is possible to use two to force current through the sample and use the other two to measure the voltage drop that occurs due to this current. The contacts of the voltage

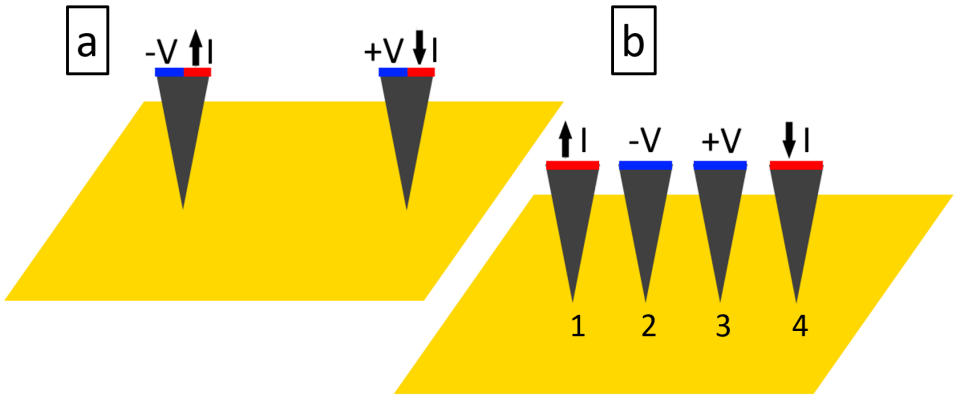

Figure 2.4: Sketch of the measurement setup for ***(a)****: a two point measurement on the left and* ***(b)****: a four point measurement on the right. The two point measurement will always be influenced by the resistance of the wires used to contact the thin film, as well as the resistance of the contacts themselves. The four point measurement circumvents this by not sending any current through the wires that are used to measure the voltage drop.*

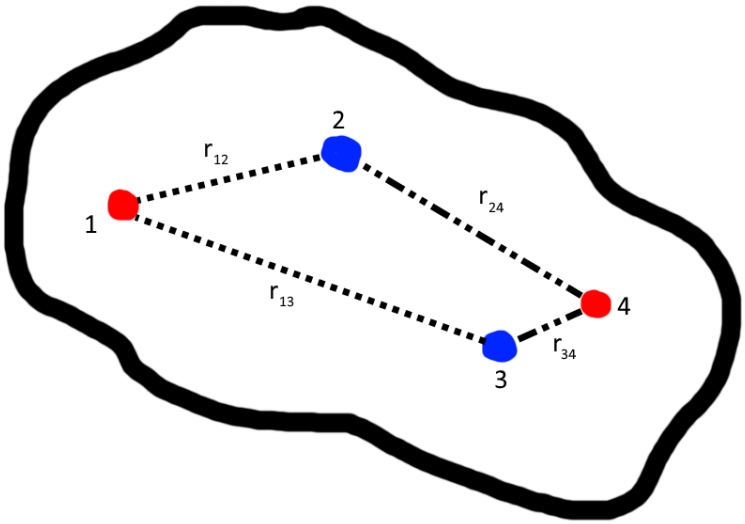

Figure 2.5: Realistic example of the probe placement on a wafer. Contacts 1 and 4 are used to pass current through the thin film, contacts 2 and 3 are used to measure the drop in voltage between them. The distances r_{12}, r_{13}, r_{24}, r_{34} are used to calculate the correction factor when the probes are not placed perfectly equidistant in one line.

sensing wires and the wires themselves do not carry any current and therefore are not contributing to the measured drop in voltage. This allows the precise measurement of very small resistances.

To use the four point method, the probes are placed in a straight line on the sample as seen in figure 2.4**(b)**. Current is passed through the two outermost points 1 and 4, and the voltage is measured between the inner two probes 2 and 3.

If the probes are placed in a perfectly straight line and the sample is sufficiently large compared to the probe spacing [32], the resistance of the sample can be calculated according to equation 2.3 [33].

$$\rho = \frac{U}{I} \cdot \frac{\pi}{\ln 2} \cdot t \tag{2.3}$$

where :

ρ = resistivity

U = voltage

I = current

t = film thickness

Such a perfect placement is difficult to do by hand, however. Figure 2.5 shows a realistic placement of the contact points. The red points 1 and 4 show the points where current is forced through the sample, blue points 2 and 3 show where the voltage drop is measured on the sample. Distances between two points A and B are marked by r_{AB} and are required to calculate the resistivity with such a probe placement.

If the probes are not placed in a perfectly straight line, equation 2.3 is expanded to equation 2.4 to correct for the difference in voltage drop across the two voltage sensing probes [33]. When the spacing of the probes is of the same order of magnitude as the wafer dimensions, an additional geometric correction factor is introduced. Experimental correction factors are available in literature [34].

$$\rho = \frac{U}{I} \cdot \frac{2\pi}{\ln \frac{r_{31} r_{24}}{r_{34} r_{21}}} \cdot t \cdot C(\text{shape}) \tag{2.4}$$

where :

r_{AB} = distance between points A and B

$C(\text{shape})$ = correction factor for thin film shape, found in literature

The equations discussed above all result in a value for the measured resistivity. Another often used measurement is the resistance or, when discussing transparent electrodes, the sheet resistance. The relation between resistance, resistivity and sheet resistance is shown in equation 2.5.

$$R = R_{sq} \cdot \frac{l}{w} = \rho \cdot \frac{l}{wt} \tag{2.5}$$

where :

R = resistance

R_{sq} = sheet resistance

ρ = resistivity

l = length of the layer between probes

w = width of the layer between probes

t = thickness of the layer

As can be seen there are different ways to measure the resistivity of thin films. A four point measurement determines the exact value and a two point measurement can offer insight to *in situ* resistance changes during morphology development of the thin film. In this work the four point method was used to determine the exact resistivity of the deposited thin film and the two point method was used to perform an *in situ* resistance measurement. The combination of both allows for a precise characterization of the electrical properties of the thin film.

3 Methods

In order to study the development of thin film morphology during heating, several imaging techniques were used. The phenomenon of dewetting during heating was studied *in situ* in a light microscope. Both brightfield and transmission modes were used to image the changing thin film morphology. While the film was heated under the microscope the electrical resistance was measured. At different stages the heating was interrupted and the sample cooled down quickly to analyse the grain structure in a scanning electron microscope (SEM) and a transmission electron microscope (TEM). This allows for the study of a certain region of interest in regards to several properties, like grain size evolution and changing electrical resistance as well as macro- and microscale structure. The results were correlated, with a special focus on the influence of grain size and thin film morphology on the electrical resistance during heating.

3.1 Light microscopy

The light microscope is a fundamental tool used in science. A set of lenses refract the beam and following geometric rules the image becomes magnified. Since the image is constructed with light in the visible part of the electromagnetic spectrum, it can be seen directly with one's own eyes or a regular camera. A sketch of a simple lens configuration can be seen in figure 3.1 [35]. Reflection mode (figure 3.1**(b)**) illuminates the sample from above and creates contrast by light scattering on the surface of the sample, allowing this mode to be used for bulk samples. In transmission mode (figure 3.1**(a)**) the sample is illuminated from below and light has to pass trough the material to reach the objective lens. Contrast is created by light attenuation and a transparent sample is required for this type of imaging. Both types of imaging were used in this work.

When light passes through an aperture or a lens, the light rays are diffracted and create an interference pattern. This leads to a small, concrete point being displayed as an Airy disk, where the representation of the object in the image

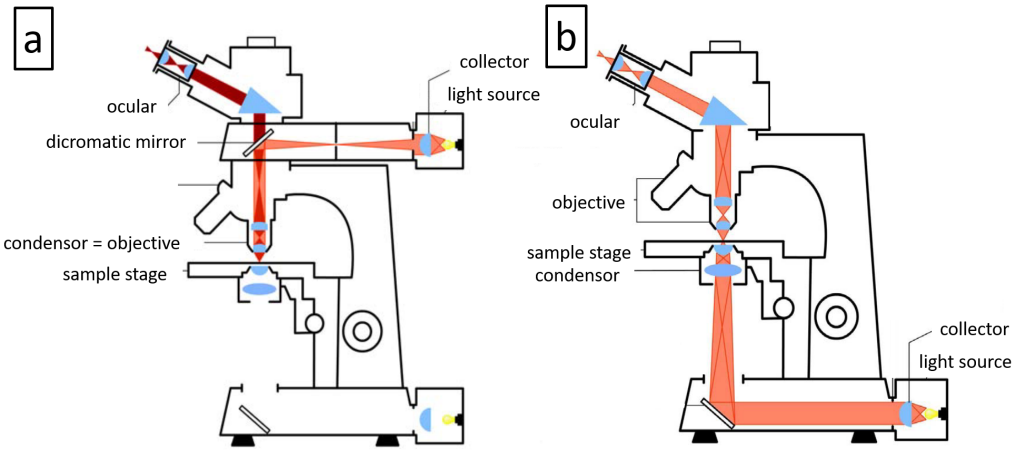

Figure 3.1: Example sketch of the lenses in a light microscope. The Microscope is sketched in black, lenses are displayed in blue and the path of light from the light source to the eyes is shown in orange and red (adapted from [35]). ***(a)****: The left setup works with light that is reflected from the sample towards the objective lens.* ***(b)****: On the right the configuration of light source and lenses is set for transition mode. Here the light has to pass through the sample to reach the objective lens.*

plane is displayed as a bright center spot, lined with concentric rings. This bright area around the center spot can interfere with other nearby objects that are projected onto the image plane. An example of Airy disks around two objects, as well as the intensity profile along the line trough both center spots can be seen in figure 3.2. The distance decreases from figure 3.2**(a)**, where the two points are easily distinguishable, to figure 3.2**(c)**, where the two spots appear as a single one. If non-circular apertures or lenses are used, the diffraction pattern no longer forms concentric rings.

In order to differentiate two points in the image, their central spots must not overlap. The maximum resolution possible with this restriction in mind is defined by the Rayleigh criterion as shown in equation 3.1, where the minimal resolvable distance is defined as the radius of the Airy disk r_{Airy} [37].

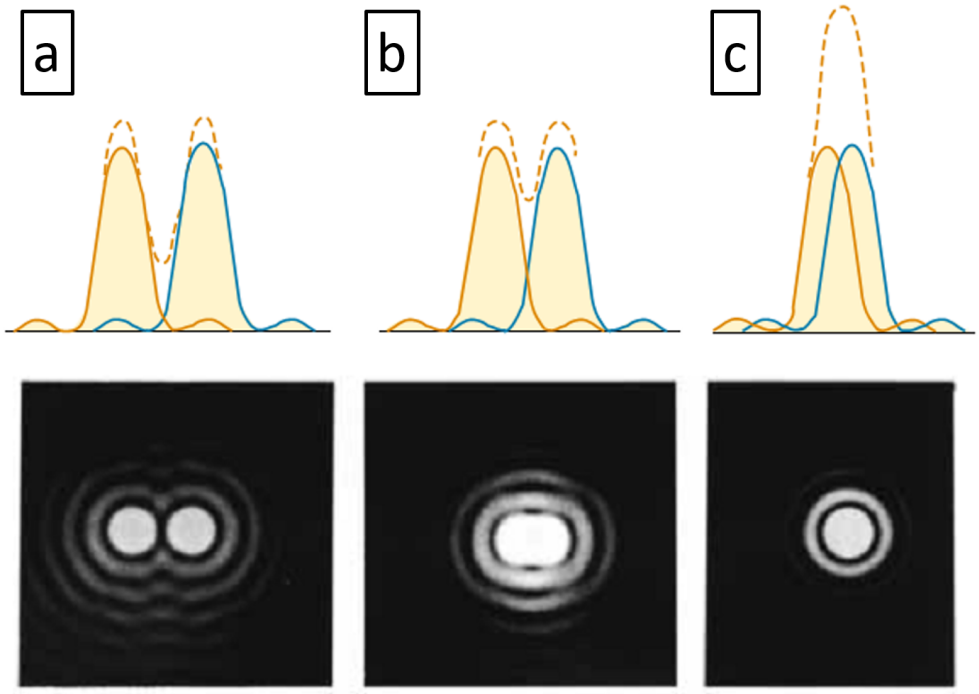

Figure 3.2: Diffraction patterns of two points. The top row shows the light intensity across a line profile in the image, the bottom row shows images of the corresponding Airy disks. ***(a)****: The points are separated and can be resolved individually.* ***(b)****: The two Airy disks overlap such that the maxima of one is on the minimum of the other. They are at the limit of what can be resolved according to the Rayleigh criterion.* ***(c)****: The points are together close enough such that they are no longer distinguishable [36].*

$$r_{Airy} = 0.61 \frac{\lambda}{\sin \alpha} \tag{3.1}$$

where :

r_{Airy} = radius of the projected Airy disk

λ = wavelength of the light used to image the sample

α = half the angle of convergence

The same formula can be reached with other assumptions in mind. Abbe defined the resolution limit, based on the two slit experiment, to be reached

when there are no longer two local maxima reaching the screen, or in the case of a microscope, the objective lens. The first maximum after the center ray is defined by equation 3.2. This would result in a resolution limit as shown in equation 3.3. If only one of the two maxima to both sides of the center beam has to hit the lens however, the angle between the center spot and the first maximum can increase and the resulting equation 3.4 defines a limit similar to the one defined by Rayleigh [37].

$$\sin \alpha = \frac{\lambda}{d} \tag{3.2}$$

$$d \geq \frac{\lambda}{\sin \alpha} \tag{3.3}$$

$$d \geq \frac{\lambda}{2 \cdot \sin \alpha} \tag{3.4}$$

where :

d = minimum distance between two points below which they are not distinctly resolvable

An additional limiting factor is the refractive index of the medium between the objective lens and the specimen. It inversely affects the resolution limit and can be increased by immersing the sample in oil. The maximum resolution is then defined by equation 3.5.

$$d \geq \frac{\lambda}{2 \cdot n \cdot \sin \alpha} = \frac{\lambda}{2 \cdot NA} \tag{3.5}$$

where :

n = index of refraction between the sample and the objective lens

NA = numerical aperture of the objective lens

The resolution therefore depends on the wavelength, the angle of convergence and the index of refraction between the lens and the sample. The part of the electromagnetic spectrum that is visible with the naked eye is limited and the

index of refraction can be varied, but only within limits. The angle of convergence can be changed by moving the lens closer to the sample or by using a larger lens. However, this is limited to a half angle of 90°. It also incurs a penalty in that the depth of focus decreases with an increasing angle of convergence. This makes it necessary to find a compromise between influence on resolution, depth of sharpness and working distance.

Errors can also be introduced by imperfect shapes of the lenses – called spherical aberration – as well as by the difference in the index of refraction of the lens material for different wavelengths – called chromatic aberration. This limits the resolution in both light microscopy as well as electron microscopy.

3.1.1 Contrast: brightfield and darkfield

There are several imaging modes available in a light microscope. Two basic ones are brightfield and darkfield imaging. A sketch of the path that light will travel in these configurations of a microscope can be seen in figure 3.3**(c)** and figure 3.3**(d)**, respectively. In brightfield imaging the image is taken from the same direction from which the sample is illuminated. This leads to a picture that is bright when there is no sample deflecting the light and dark whenever there are shapes that do not scatter the light, but let it pass or reflect it away from the objective lens. In darkfield imaging the opposite is true: without any sample in front of the objective, the image will be dark. If there is a sample that scatters the light or reflects it towards the objective lens, there will be a bright spot on the sensor. This can help to see shapes and sizes better as a clearer contrast is created. Figure 3.3**(a)** shows a brightfield and figure 3.3**(b)** a darkfield image of gold particles on silicon oxide. The brightfield image shows the blue color of the silicon oxide substrate and the particles appear darker as they reflect the light away from the objective lens. In darkfield mode the edges of the particles appear bright as they reflect and scatter the light towards the objective lens and the substrate appears dark.

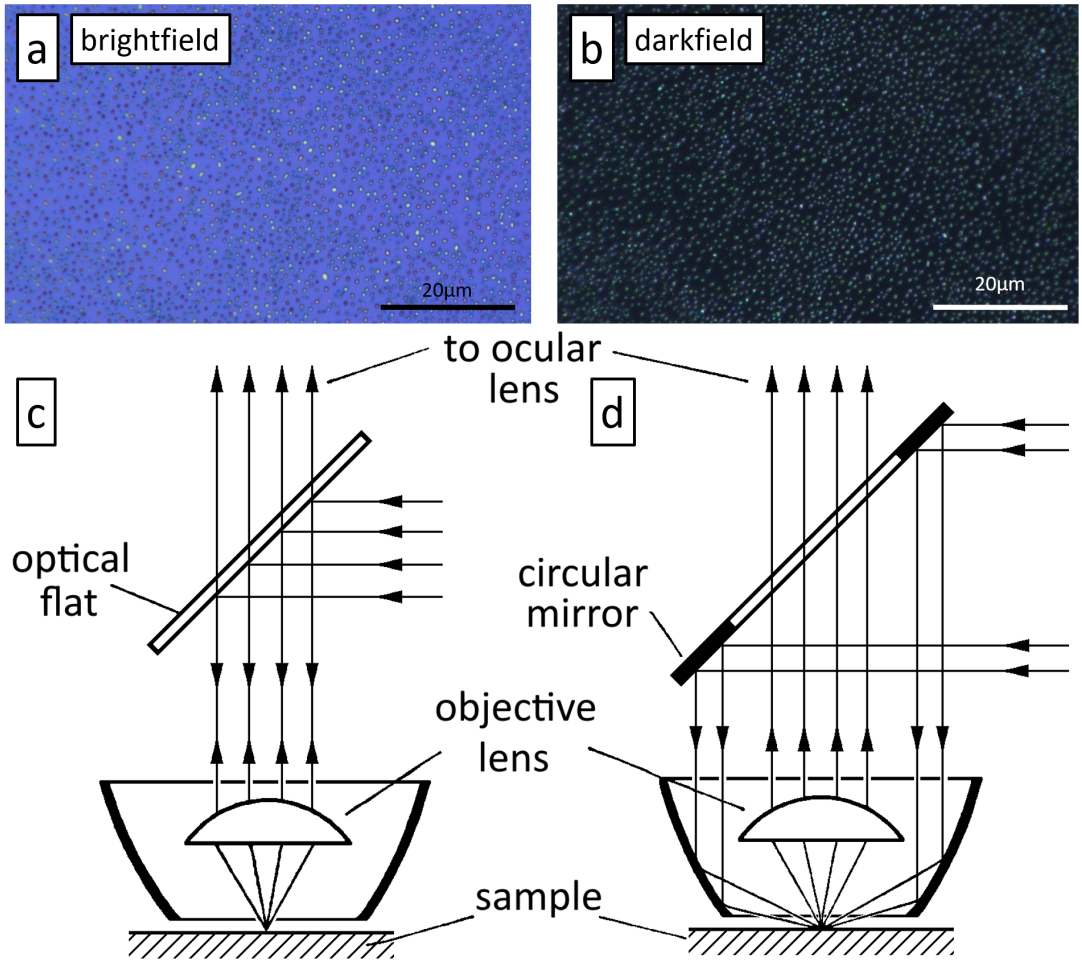

*Figure 3.3: An example of brightfield ((**a**)) and darkfield ((**b**)) microscopy. In brightfield mode, the substrate is bright and the particles appear as dark or golden spots, depending on how they reflect the light. The darkfield image shows the particles as bright parts against the black substrate. A sketch of the path of light in brightfield mode ((**c**)) and darkfield mode ((**d**)) can be seen below. In brightfield mode, the reflected light is responsible for most of the brightness on the sensor. In darkfield microscopy scattered light creates the image (figure adapted from [38]).*

3.1.2 Heating stage: TS1200 with electrical contacts

In order to measure the resistance of the sample during heating a Linkam TS1200E heating stage was used. This allows for precise temperature control while imag-

ing and has two contacts to measure the resistance of the sample. It is able to heat the crucible to temperatures of up to 1200 °C with a temperature stability of 1 °C and a maximum cooling and heating rate of 200 °C per minute. It enables both brightfield and darkfield as well as transmission mode imaging. Gas inlets and outlets allow precise control of the composition of the atmosphere around the sample. The stage requires the use of microscope objective lenses with a particularly long working distance of at least 8.6 mm and a maximum angle of convergence of 11.3° if the sample is not placed at an elevated position in the crucible [39].

The resistance of the sample was measured during heating using the two contacts in the heating stage. The resistivity was determined after heat treatment with a four point measurement, so that the *in situ* measured change of resistance could be correlated with the absolute value of the thin film resistivity.

A picture of the stage is shown in figure 3.4, along with a sketch of a sample prepared for heating as well as a schematic that shows the long working distance required for this heating stage.

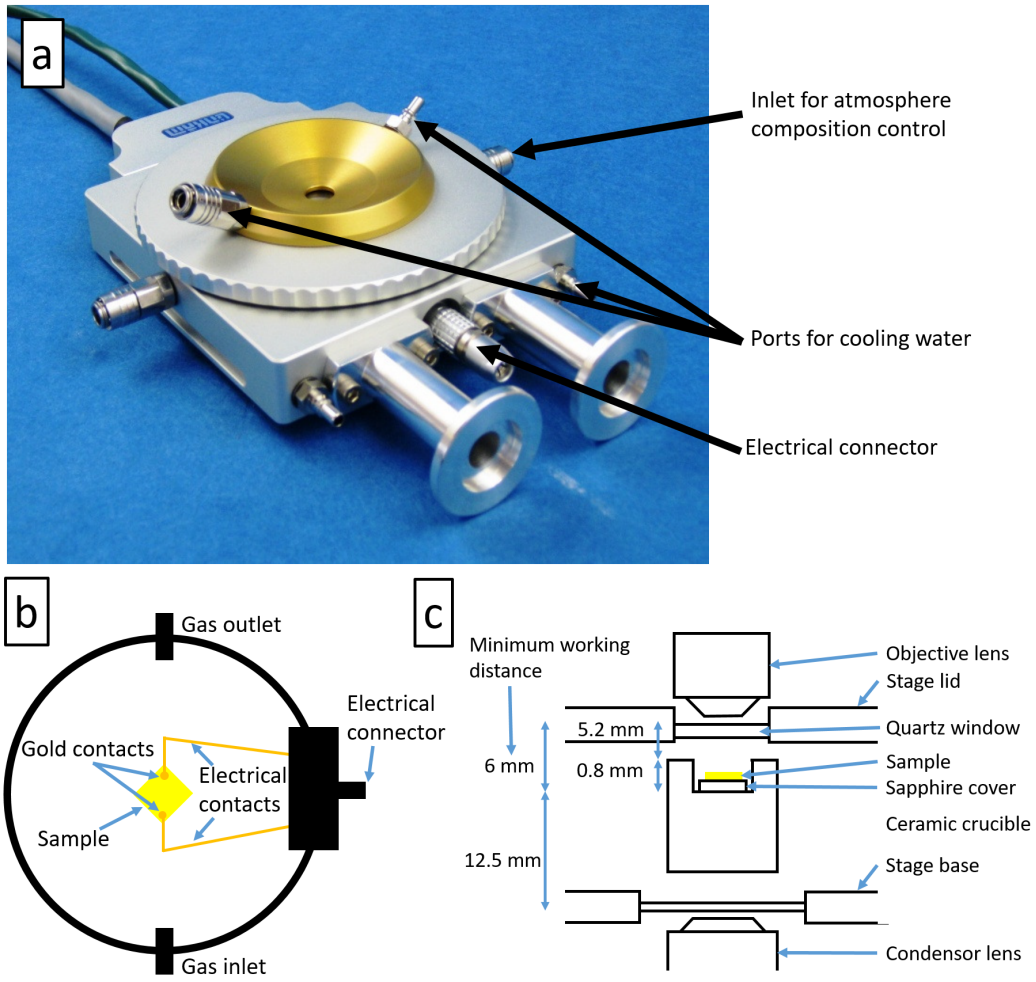

Figure 3.4: The TS1200E heating stage used for the experiments. ***(a)****: Picture of the heating stage with labeled connections.* ***(b)****: Sketch of the setup for an experiment. The sample is placed in the heating crucible and connected with gold wires to the electrical connector. Contact paste is applied to the wires and thin film to decrease parasitic contact resistance.* ***(c)****: Sketch of the heating stage from the side. The construction requires the use of a microscope with a long working distance of at least* 8.6 mm *[39].*

3.2 Scanning Electron Microscopy

A scanning electron microscope uses electrons instead of photons to image a sample. The part of the electromagnetic spectrum that can be used in light microscopy is limited. While there are several methods that improve the resolution beyond the size that is can be resolved according to Abbe (equation 3.4) and Rayleigh (equation 3.1), the wavelength is limiting the resolution. The advantage of using electrons instead of visible light like in the light microscope, is that the wavelength of the electrons can be controlled by the acceleration voltage. This enables the SEM to reduce the wavelength of the accelerated particles and increase the resolution. While the wavelength of the accelerated electrons can be reduced to the size of atoms, other effects emerge that limit the resolution or practicality of using higher energies.

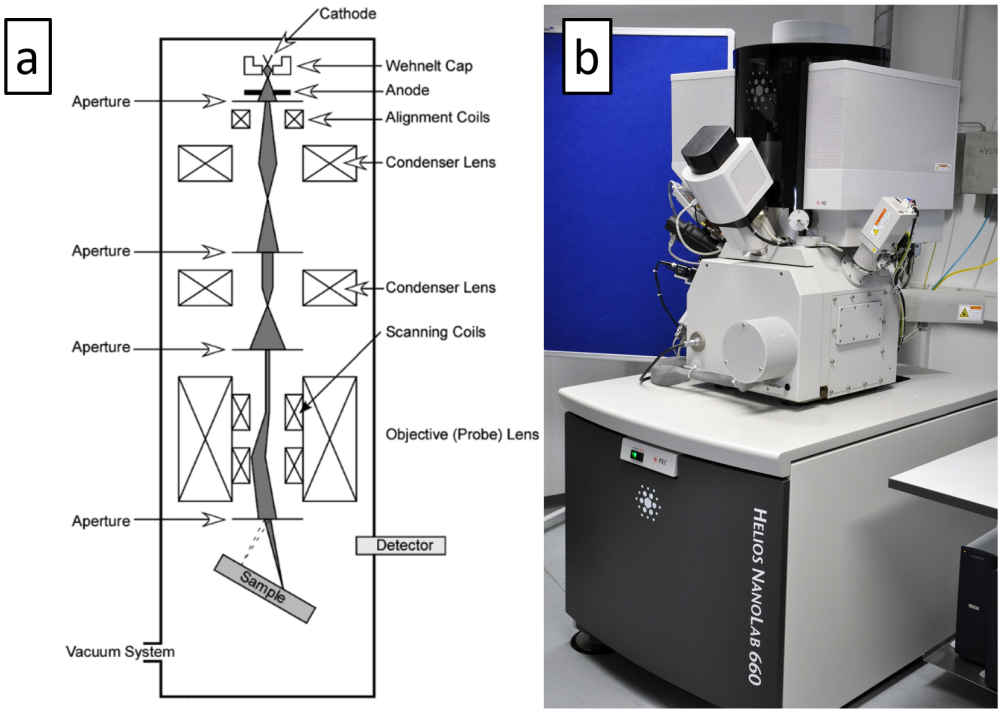

Figure 3.5: Configuration of a Scanning Electron Microscope [40]. On the right the microscope used in this work, a FEI Helios Nanolab 660 dualbeam FIB/SEM [41] can be seen.

The SEM consists of an electron source that emits and accelerates electrons, electromagnetic or electrostatic lenses that focus the source to a point, and scanning coils to direct the electron beam to different points on the sample. The image is captured by scanning the beam across the sample and measuring the response with different detectors. The strength of the response at a point determines the brightness of the pixel in that place. A sketch of the arrangement of these parts can be seen in figure 3.5. The microscope used in this work, a FEI Helios Nanolab 660 dualbeam FIB/SEM [41] is also shown. It features an additional Focused Ion Beam (FIB) that can be used to remove or deposit material at microscopic scales.

Due to the particle/wave duality of small particles the wavelength of an accelerated electron can be calculated with equation 3.6 [42]. For sufficiently high acceleration voltages the volume of interaction determines the size of the smallest resolved distance.

$$\lambda = \frac{h}{p} = \frac{h}{m \cdot v} = \frac{h}{\sqrt{2m_0 E(1 + \frac{E}{2m_0 c^2})}} \tag{3.6}$$

where :

λ = wavelength of the accelerated particle

h = Planck's constant

p = relativistic momentum of the particle

m = relativistic mass of the particle

m_0 = rest mass of the particle

E = kinetic energy of the particle

v = speed of the accelerated particle

c = speed of light in a vacuum

When an electron hits the surface of a sample, it interacts with the atoms in it and gives rise to several phenomena. They can be separated by the location at which they occur as seen in figure 3.6, which shows the incident electron beam and the resulting interaction volume. The generated signals show different information about the sample, like chemical composition (X-Rays), material

and channeling contrast (Backscattered Electrons) or surface features (Secondary Electrons), depending on the location of where the signal is generated and what characteristics the signal has.

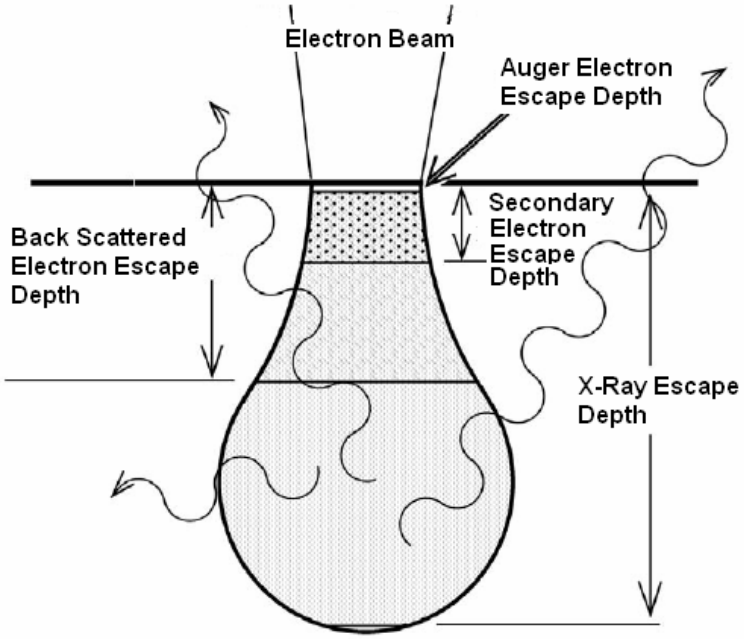

Figure 3.6: Interaction volume of an electron beam with a sample [43].

3.2.1 Secondary Electrons and Backscattered Electrons imaging

One image mode is the method of Secondary Electrons (SE) imaging. They are generated by inelastic scattering of the incident beam. Due to their low energy of less than 50 eV they only escape the sample and reach the sensor when created close to the surface. The signal is therefore mainly generated on a spot the size of the probe that is projected on the sample and allows for a very high resolution [44]. SE can be detected with an Everhart-Thornley Detector that consists of a charged cage to attract the low energy electrons, a scintillator and a photomultiplier in order to detect the signal.

Backscattered Electrons (BSE) are incident electrons that exit the sample after one or more elastic scattering events. They retain most of their energy.

Detecting this kind of electrons is nowadays done by a semiconductor ring above the sample. Due to their high energy BSE can not be efficiently attracted to the detector. Instead the detector has to cover as large of an angle around the incident site as possible in order to collect many BSE. Different materials scatter the incoming electrons differently and therefore allow for phase contrast. A plot of the different intensities of the SE and BSE intensities can be seen in figure 3.7 [45], which shows the yield in SE and BSE as a function of atomic number. Yield describes the number of SE and BSE that are generated per incident primary electron. While the SE yield stays almost constant for materials with an atomic number above 10, BSE show an increase in yield for the entire periodic table that diminishes at high atomic numbers, but never flattens of. This difference in yield results in a grayscale contrast of different materials in the BSE image.

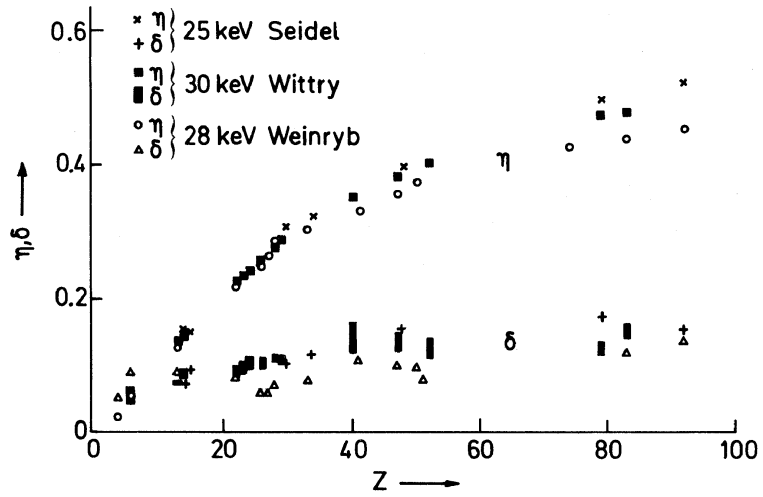

Figure 3.7: Increase of BSE (η) and SE (δ) yield with increasing atomic number Z. The difference in BSE yield between different atoms allows for a simple material contrast [45].

3.2.2 Electron Backscatter Diffraction

If the sample is tilted relative to the incident beam, BSE can be used to determine the crystal structure at the point of incidence. In the same way the SEM constructs a grayscale image by scanning the sample, a detector for Electron

Backscatter Diffraction (EBSD) can be used to construct an image of the grain orientation. The detector configuration can be seen in figure 3.8(**a**).

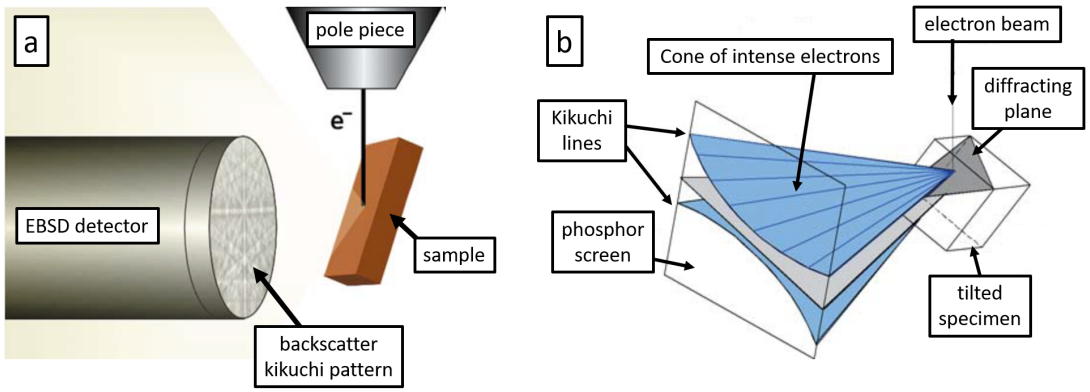

Figure 3.8: ***(a)****: Configuration of EBSD measurement. The sample is tilted at a high angle and the EBSD detector is perpendicular to the electron beam.* ***(b)****: Process of generating Kikuchi lines. A crystallographic plane diffracts the BSE that leave the sample [46].*

The electrons from the beam are scattered near the incidence site and due to the large angle of the surface relative to the incident beam a lot of the scattered BSE are able to leave the sample. If they make their way out of the sample, some of them will fulfill the Bragg condition as described in equation 3.7 [47].

$$2{\cdot}d \cdot \sin\Theta_{maximum} = n \cdot \lambda \tag{3.7}$$

where :

d = lattice parameter of the material

Θ = angle between incidence beam and planes of the crystal lattice

n = any integer

λ = wavelength of the incident electrons as described in equation 3.6

This leads to an accumulation of intensity along the conic section to which they are diffracted. Due to the arrangement of the detector and the sample these conic sections can be approximated by lines. The resulting lines on the detected

image are called Kikuchi bands and correspond to the lattice planes in the crystal that is imaged. An illustration of this can be seen in figure 3.8**(b)**. The pattern of Kikuchi bands is characteristic for each crystal structure and – depending on which lines are seen – the orientation of the crystal can be determined. A sketch of the different patterns corresponding to different crystal orientations can be seen in figure 3.9**(a)**. Figure 3.9**(b)** shows a real image of a backscatter Kikuchi diffraction pattern. In figure 3.9**(c)** the diffraction planes of the image in figure 3.9**(b)** are highlighted and the zone axes labeled.

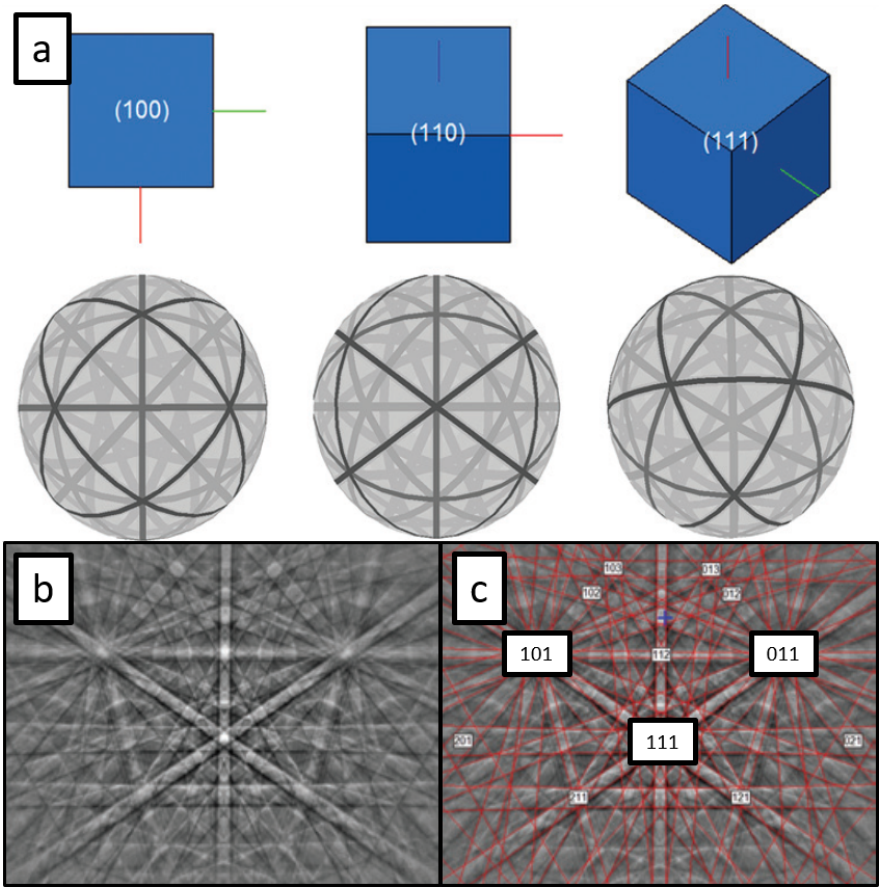

Figure 3.9: Characteristic backscatter Kikuchi diffraction patterns. ***(a)****: Sketch of the patterns and the corresponding crystal orientations of a cubic structure.* ***(b)****: Real image of a backscatter Kikuchi diffraction pattern.* ***(c)****: The same pattern as in* ***(b)****, but the diffraction planes are marked and the zone axes labeled [48].*

3.3 Transmission Electron Microscopy

Compared to an SEM, a Transmission Electron Microscope (TEM) can use a much higher voltage to accelerate the electrons. TEM samples have to be transparent to the high velocity electrons, because the detectors are located along the path of the electrons. A sketch of the lens configuration of a TEM can be seen in figure 3.10, along with a picture of the FEI Titan Themis^3 300 [49] used in this work. In a TEM the electron source, lenses, sample and detector are all placed in one line. The lenses can be used to put the sample both in an image as well as a diffraction plane of the electron beam, resulting in either location or diffraction information to be imaged on the sensor. The TEM relies on different detection mechanisms than the SEM. While both BSE and SE can be created in a TEM due to the interaction of the electron beam with the sample, the detectors are in line with the electron beam and image the sample with the transmitted electrons. This enables both spacial information and diffraction information to be gained from the sample. Magnifications of up to atomic resolution are possible, as well as diffraction patterns to study the grain lattice [50].

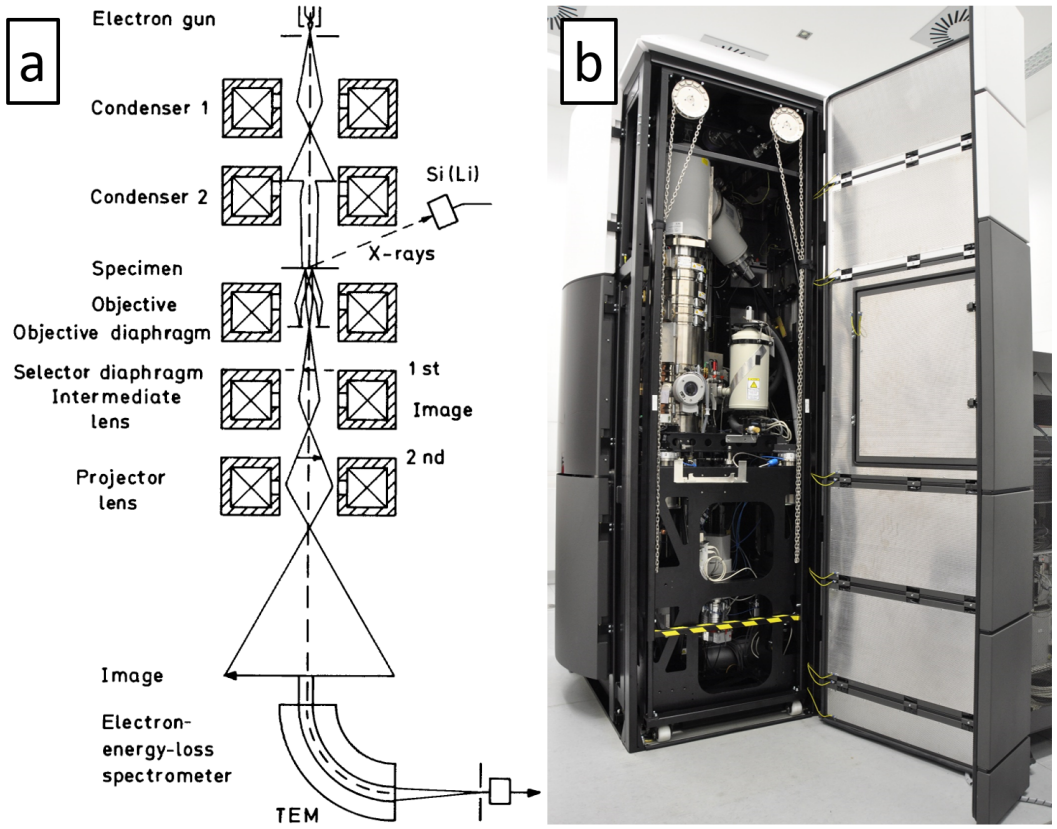

Figure 3.10: Schematic of the electron path in a TEM. Lenses, sample placement and sensor positions for X-ray and electron energy loss spectroscopy are also shown [50]. On the right a picture of the microscope used in this work, a Titan Themis^3 300 [49], can be seen.

4 Experimental setup

In this chapter the experimental setup will be explained. The goals of the experiments are to accurately determine the resistivity before heating, to observe the thin film development during heating with the light microscope and to measure the resistivity and grain size after heating to different temperatures, in order to find the parameters to optimize the electrical conductivity of the deposited thin film.

4.1 Creation of Thin Film

For the experiment gold thin films were prepared on two different substrates. One on a silicon wafer with a 500 nm silicon oxide layer for use in experiments with electrical measurements. The silicon wafers were cut in order to fit into the microscope and cleaned with acetone to provide a system without any unknown influences as far as possible. Other samples were prepared on a silicon nitride TEM grid. In the center of these samples only the silicon nitride supports the thin films. This allows for the samples to be viewed in a TEM as well as using the transmission mode of the light microscope. The substrates were chosen for their isolating quality as to not influence the electrical measurement of the thin film.

The wafers were coated with a 20 nm thin gold film. For this the Electron Beam Physical Vapor Deposition system (E-Beam) HVB 130 by Winter-Vakuumtechnik [51] was used. An image of the deposition system can be seen in figure 4.1, showing the interior with the sample holder at the top, the vent to the vacuum system in the middle and the crucible with gold at the bottom (**(a)**) as well as the exterior, including the control interface at the right and the closed vacuum chamber at the left (**(b)**). The deposition rate used was 0.5 Å per second.

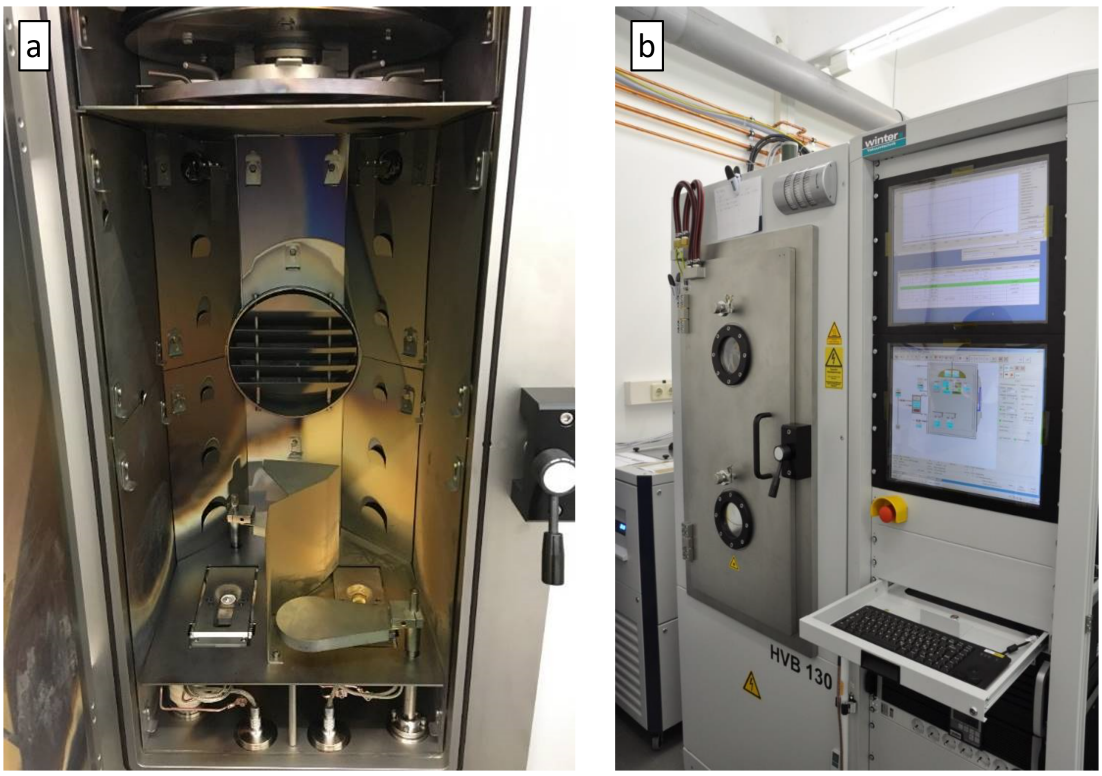

Figure 4.1: Picture of the Electron Beam Physical Vapor Deposition system HVB 130 by Winter-Vakuumtechnik [51] used for this work. A: Vacuum chamber with the material source at the bottom and the sample holder at the top. B: A view of the system at work (Image from [52]).

4.2 Heating of the thin film

The thin films were heated using a Linkam TS1200E heating stage. The experiments were started at 20 °C and the temperature was increased by 30 °C per minute. During heating the crucible was flushed with nitrogen. Removing the oxygen from the atmosphere around the wafer prevents any further oxidation of the silicon in the wafer and minimizes the build up of stresses. With less stress in the thin film, bulging can be reduced and bubble formation prevented (see discussion in chapter 6.2). The increased nitrogen content when compared to ambient air increases the temperature needed to dewet the wafer [53].

Having only two contacts available for *in situ* measurements does not allow

to determine the resistivity, as the resistance of the wires and the contact points influence the measurement. However, it is possible to observe the total change in resistance in the wire, contacts and thin film system, resulting in a resistance measurement relative to the starting resistivity. Thanks to the automated *in situ* two point measurement I developed, determining the regime of conductivity of the thin film can be done *in situ* while heating. Once the desired regime is reached, the heating process is stopped and the sample is cooled down at a rate of 200 °C per minute in order to preserve the microstructure as best as possible. Multiple wafers were prepared and cooled after heating to 76 °C, 172 °C, 393 °C, 650 °C and 698 °C within 2, 5, 12, 20 and 23 minutes, respectively. These temperatures were chosen based on the measured *in situ* resistance.

4.3 Electrical measurement

When doing electrical measurements it is important to create a good contact. If this is not the case, parasitic resistance at the points of contact will influence the measurement. In order to achieve good connectivity, Acheson Silver DAG 1415 [54] contact paste was used for experiments when no elevated temperatures were needed. For experiments with high temperatures PELCO conductive gold paste [55] was applied to the contacts.

After placing the sample in the crucible of the heating stage, gold wires are inserted which hold the wafer in place and provide a connection to the electrical port in the heating stage. Gold paste is then applied to improve the contact between the thin film and the wires. This setup can be seen in figure 4.2, the wafer and contacts are at the center and the electrical connector is at the right of the image.

The main part of this work incorporates three electrical measurements: before, during and after heat treatment. Due to the limitations of the heating stage only a two point measurement was possible during heating. Values gained during heating therefore only allow for a relative reading of the whole system instead of an accurate measurement of the thin film resistivity. The readings before and after were performed with a four point setup in order to measure the exact resistivity

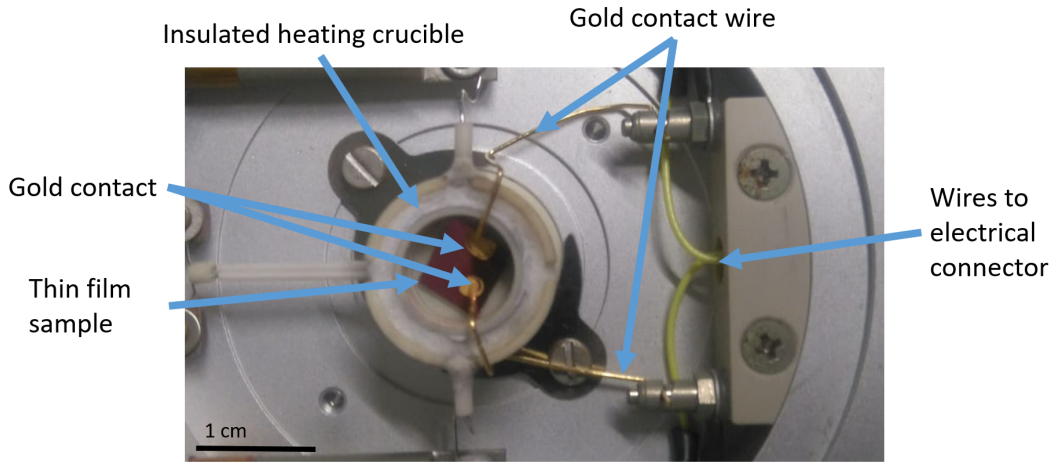

Figure 4.2: An example of a wire to thin film contact. Gold paste was used to provide a good electrical conductivity. The wafer is in an isolating crucible, gold wires are connected to the thin film with the gold contact paste. The electrical contacts that lead outside the heating stage are seen on the right.

and eliminate all parasitic contact resistances. A schematic of the workflow for electrical measurements can be seen in figure 4.3.

For the measurements a Tektronix Keithley 2400 Source Measure Unit [56] was used. It allows for the measurement and source of electrical current of up to 1 A and voltage of up to 200 V. The measurement accuracy changes with the absolute value and starts at 300 pA for a current measurement and 300 µV for a voltage measurement [56]. Accurate two and four point measurements can be easily implemented with the integrated sweep functions. More complex tasks can be coordinated using the serial port of the device and a computer. Python was chosen to implement the logic for communicating via the serial interface. To ease the data analysis, a script was developed to automate the measurement. Using the serial port, instructions were sent to, and data read from the device.

For the four point measurement before and after heating, a sweep was performed. During the sweep measurement the device applies different levels of voltage sequentially from −0.1 V to 0.1 V and measures the current drawn. The resulting scatter plot of current measurements on the x axis and voltage values on

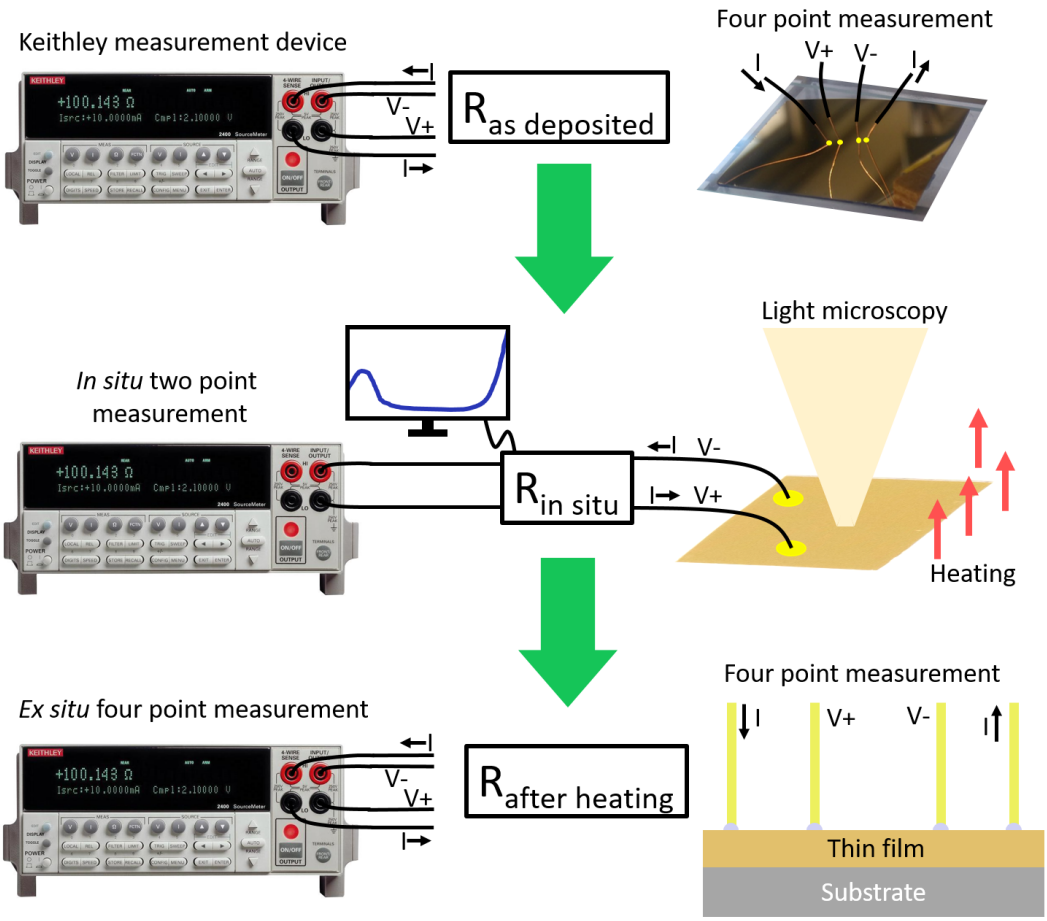

Figure 4.3: Workflow of the electrical measurements. The resistivity is determined accurately before and after heat treatment with a four point measurement, and an in situ two point measurement is performed during heat treatment.

the y axis can then be analysed. If the individual data points of the measurement all lie on a straight line the resistance of the wafer can be calculated by fitting a line to the data and using Ohms law as shown in equation 2.1 to calculate the resistance. If the points are not on a line, but instead form a curve with positive curvature, the resistance is increasing during the measurement. If the curvature of the resulting plot is negative, the resistance is decreasing. A changing differential resistance indicates that the contact is not perfect and needs to be redone or left to settle for longer.

For the heat treatment the script was modified. A sweep would take too long and fail to give the resistance at a single point in time. Instead only a single measurement at a certain level of voltage was taken continuously. The resulting values were saved together with the time of the measurement. In a system where no voltage is generated, a single point of measurement is enough to determine the resistance.

Because the measurement of the resistance at a defined voltage level takes less than a second, the results can be directly visualized. While the sample is heated, its current resistance is shown. This allows for the live correlation between resistance and *in situ* light microscopy observed morphology as well as targeted interruption of the heat treatment to study the microstructure at defined resistance values.

5 Results

5.1 Thin film thickness

The exact thin film thickness was determined using an Atomic Force Microscope (AFM). Using tweezers the gold film was scratched and the underlying siliconoxide exposed. Due to the difference in hardness the siliconoxide was not damaged and a sharp difference in height between the gold layer and the oxide was created. This contrast was then imaged using the AFM. The unprocessed data can be seen in figure 5.1**(a)**. The height data gained from the measurement was corrected in order to remove any inclination of the sample present in the experiment. This allows the visualization of the height difference as seen in figure 5.1**(b)**. Plotting the count of points measured per height level then shows the difference in elevation for the silicon oxide and the surface of the gold film. The plot can be seen in 5.2. This difference in height is the thickness of the deposited gold layer. The measurement was performed at three different points on the wafer to account for potential film thickness differences which could develop due to uneven deposition rates. The resulting film thickness was determined to be $(19.79 \pm 0.36)\,\mathrm{nm}$. The AFM used to perform the experiment in this work can be seen in figure 5.1**(c)**.

5.2 Hole development during heat treatment

The first step in dewetting is the creation of small holes. These holes then grow into large patches of dewetted area until the former thin film is only left as small particles on the underlying substrate. An example of this development can be seen in figure 5.3. Images **(a)-(f)** show the evolution of a 50 nm gold layer upon heating as seen in the light microscope. The continuous film starts to form holes and starting at these defects the film retracts, the holes grow and merge together. In the end only particles remain on the substrate. This is seen in the light microscope by the blue color of the substrate replacing the gold color of the thin film. Images 5.3**(g-i)** show a 20 nm thin gold film annealed for different amounts of time. In the SEM the actual morphology is resolved and

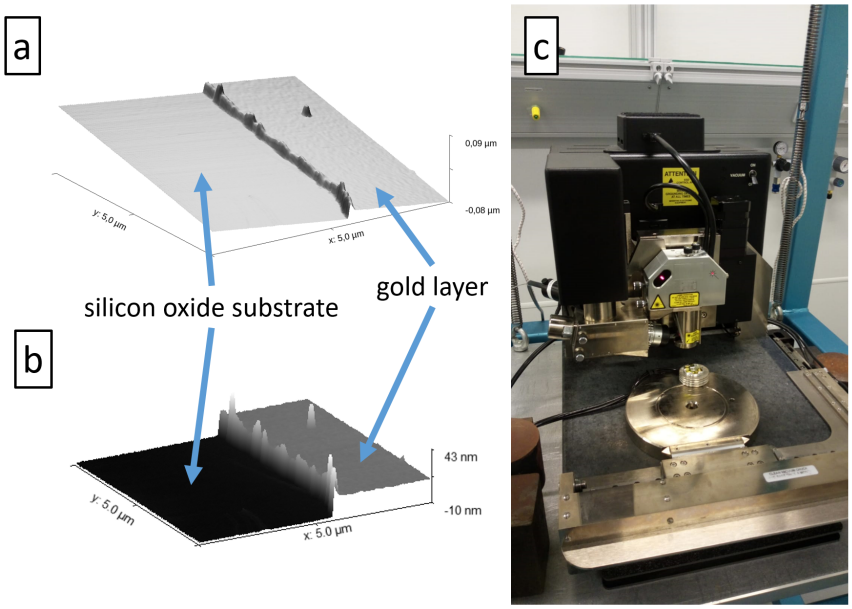

Figure 5.1: ***(a)****: Unprocessed data from the AFM. The difference in height from the gold thin film to the substrate can be seen, but in this state cannot be precisely calculated.* ***(b)****: Processed data from the AFM to be level. This can be further analysed to calculate the thickness of the gold layer.* ***(c)****: The AFM used in this work to determine the exact thin film thickness.*

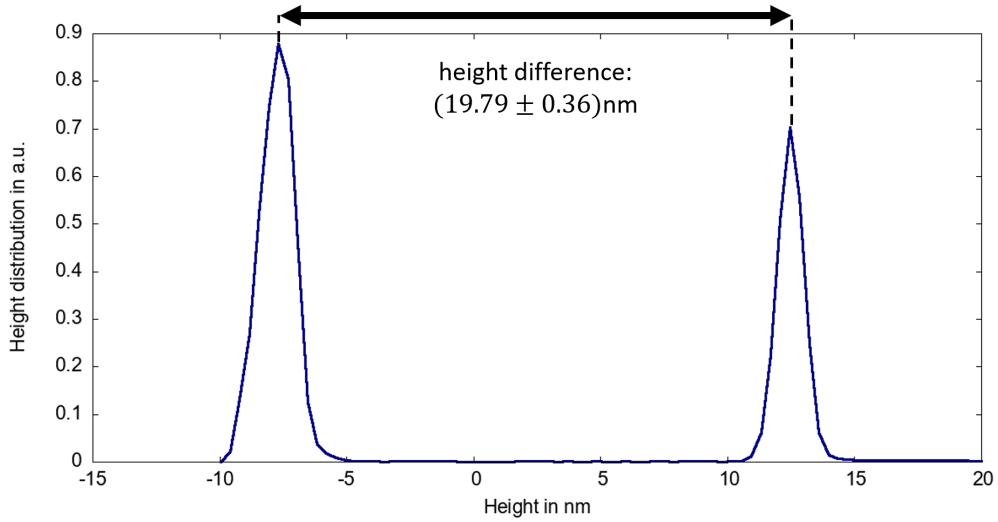

Figure 5.2: The resulting height distribution of the imaged area. The difference in the peaks is the thickness of the gold film.

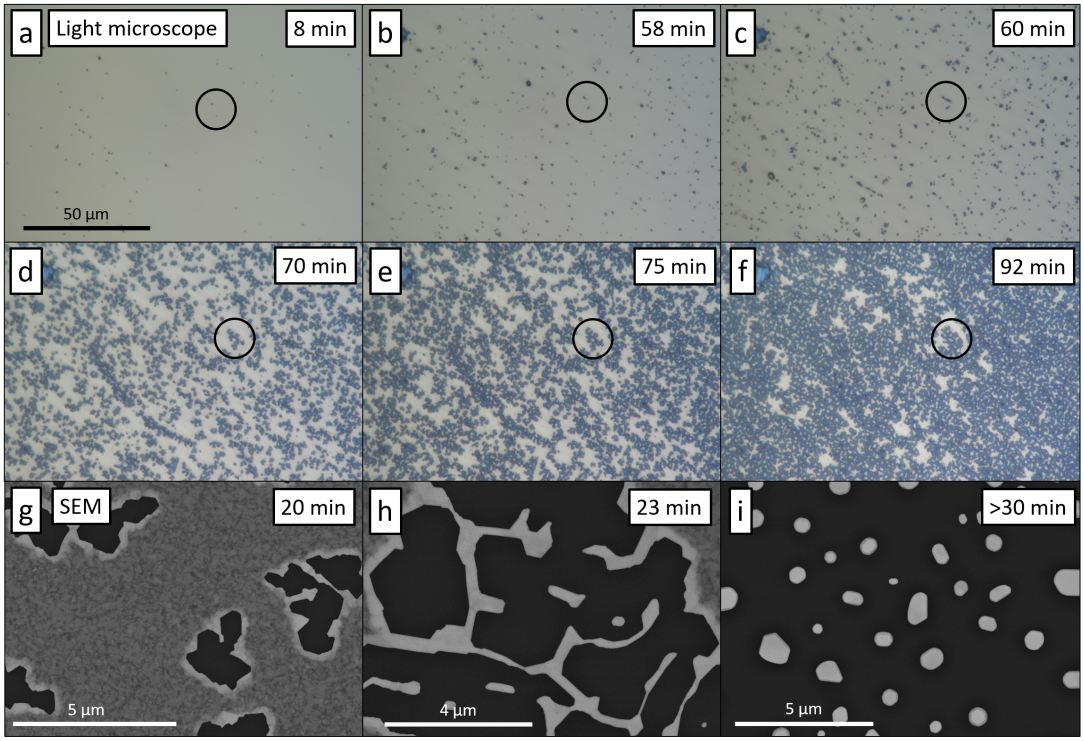

Figure 5.3: The development of thin film morphology during heating. The continuous film starts to form holes, these holes grow and connect until only particles remain. ***(a-f)****: the development of a* 50 nm *thin film as seen in the light microscope. The black circle follows the change from hole to dewetted film on a fixed spot on the wafer. The scale bar in* ***(a)*** *applies to all light microscope images.* ***(g-i)****: ex situ SEM images of a* 20 nm *thin gold film.*

single particles are visible. Thin film thickness directly influences the velocity of the thin film morphology changes, which is the reason behind the different heating durations shown in figure 5.3.

Using video information recorded during heating of the wafer, it is possible to determine the area that is still covered by the thin film and where the underlying substrate is already exposed. This process was automated using the open source computer vision library OpenCV [57] and its flexible, context independent binarisation function `adaptiveThreshold`. In order to determine the values for the arguments `blocksize` and the constant `c`, correlative constant thresholds were

applied to selected frames using ImageJ [58]. The values of `blocksize` and `c` were chosen to be `150` and `2` respectively as those lead to the best conformity between the automatically produced images of OpenCV and those manually determined with the help of ImageJ. Using this approach the area coverage during heating can be correlated with the *in situ* resistance measurement. The reasons behind these decisions are discussed in chapter 6.4.

As can be seen in figure 5.4 the dewetting leads to a reduction in thin film area coverage, which leads to an increase of resistance. The graph in figure 5.4**(a)** shows the area coverage and the relative resistance as determined by the *in situ* two point measurement for context. The resistance measurement is included in graphs to provide an easy reference between the measurements of the different thin film characteristics. While the changes in resistance during the first 10 minutes of heating are significant, the visual appearance of the thin film does not change. Small holes that are visible in SEM images after only 12 minutes of heating are too small to be picked up by the light microscope. Only after 23 minutes of heating the dewetting process becomes visually apparent in the light microscope and a significantly reduced area coverage is calculated. Beginning at 25 minutes the holes start to grow, resulting in a rapidly increasing fraction of dewetted area. At the same time the resistance increases as more and more material is cut off from the current conducting path, leading to a reduced cross section available for the charge to flow. Despite this effect counteracting gains in conductivity due to improvements in the thin film microstructure, the resistance only goes above the initial resistance after more than 35 % of area are dewetted. Images 5.4**(b-e)** show the thin film as recorded in the light microscope and are the basis for the calculation of the area coverage during heating. Images from 10 minutes to 29 minutes of heating show the development of the thin film from a continuous layer to patches of continuous film and dewetted areas. Images 5.4**(f-i)** are the binarized form of the light microscope images above. The fraction of yellow and violet corresponds directly to the area coverage as displayed in the graph 5.4**(a)**. Even though the binarization picks up on small discolorations of the thin film early on that are not part of the dewetting process, the area coverage value is still

accurate as these discolorations do not influence the calculated area coverage in any significant way.

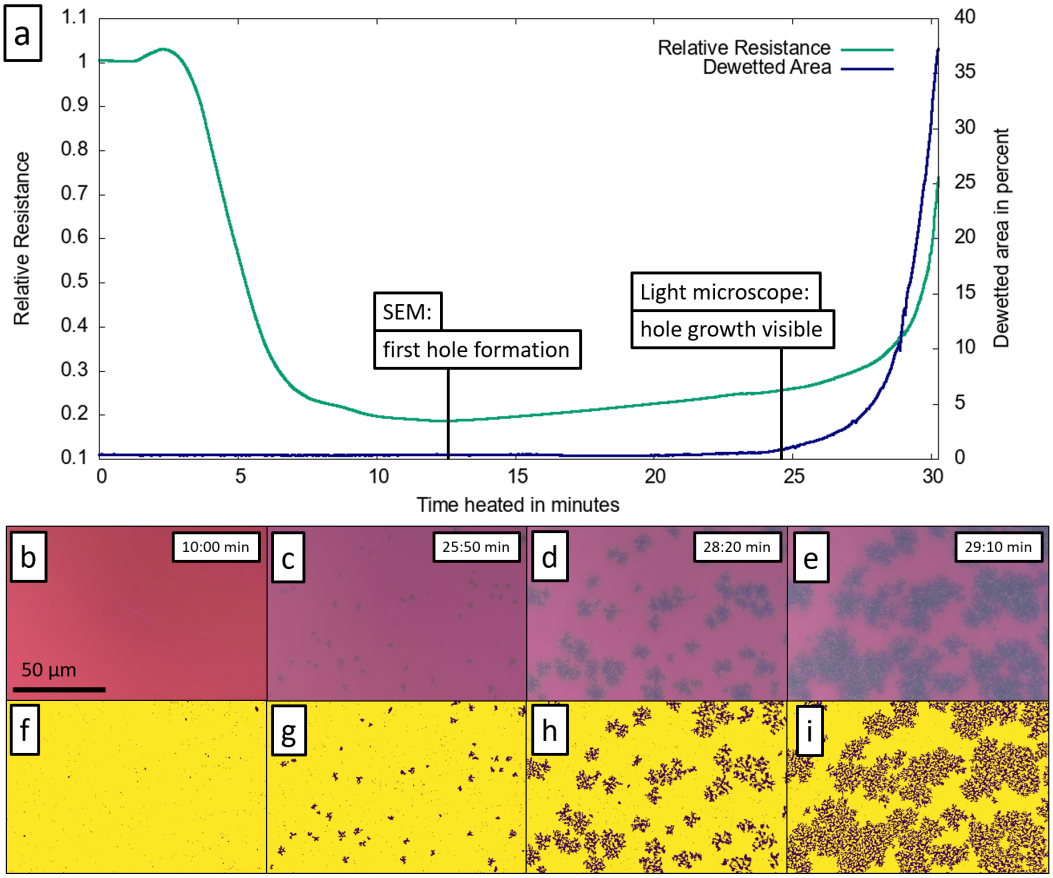

Figure 5.4: Example of how the area coverage influences the conductivity across the thin film. Pictures below show the development of the thin film during heating. The top row of pictures ***(b-e)*** *are as recorded in the light microscope, the bottom row* ***(f-i)*** *shows the binary form from which the computer calculates the area that is covered. While the SEM images show small holes after only* 12 minutes *of heating, they are too small to be picked up by the light microscope. The binarization picks up on small discolorations of the thin film, but this does not influence the calculated area coverage in any significant way.*

The SEM images show that the first holes are formed sooner than is visible in the light microscope and before any effects on the *in situ* resistance are detected.

As shown in figure 5.5, the first holes start to appear after 12 min of heating, at which point the temperature reaches 393 °C. The other two images show hole growth after 20 min, 650 °C and 23 min, 698 °C of heat treatment. The change in area coverage can be seen, as increasing temperature and heating time result in the retraction of the thin film. During retraction the grains at the rim of holes grow and protrude from the thin film [59].

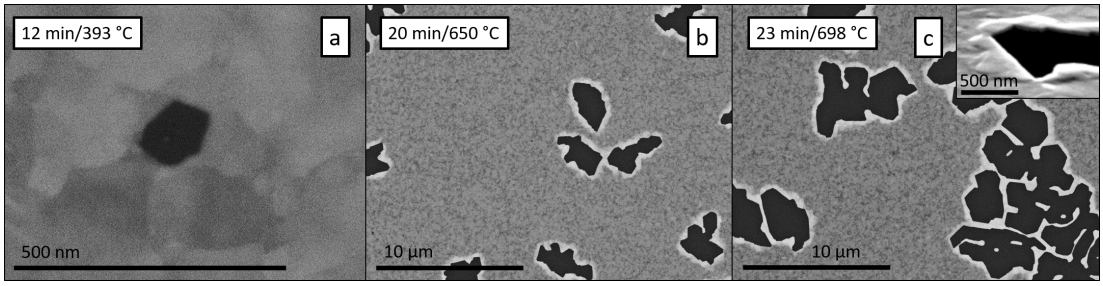

*Figure 5.5: Micrograph taken with the SEM. The first wafer (**(a)**) was heated for only* 12 minutes *and up to* 393 °C*. At this stage the first holes are visible. Wafer two (**(b)**) and three (**(c)**) show much larger holes as they were heated for* 20 min*,* 650 °C *and* 23 min*,* 698 °C *respectively. The inset on the third micrograph shows the rim of a hole.*

The samples with a transparent silicon nitride screen were used to perform an experiment using the transmission mode in the light microscope. Using the video data recorded during the heat treatment allows for the extraction of a relative transmissivity value. No experiment was performed with a specific wavelength filter, but a sum of the brightness of the pixel values shall be used as a simple analogy. The silicon nitride membrane on which the 20 nm gold film was deposited influences the transmission as well. Figure 5.6 shows some of the frames used in this analysis, from 5.6**(a)** showing the first pale signs of holes to 5.6**(i)** displaying a fully dewetted area. The total dewetting time and further the significant hole growth after 20 minutes is comparable to the behavior of the gold film deposited on a wafer with a 500 nm silicon oxide layer.

As can be seen in figure 5.7, when looking at the grayscale images the transmissivity decreases with the time the thin film was heated. The blue color channel of the RGB images provides a better contrast, however and shows the trans-

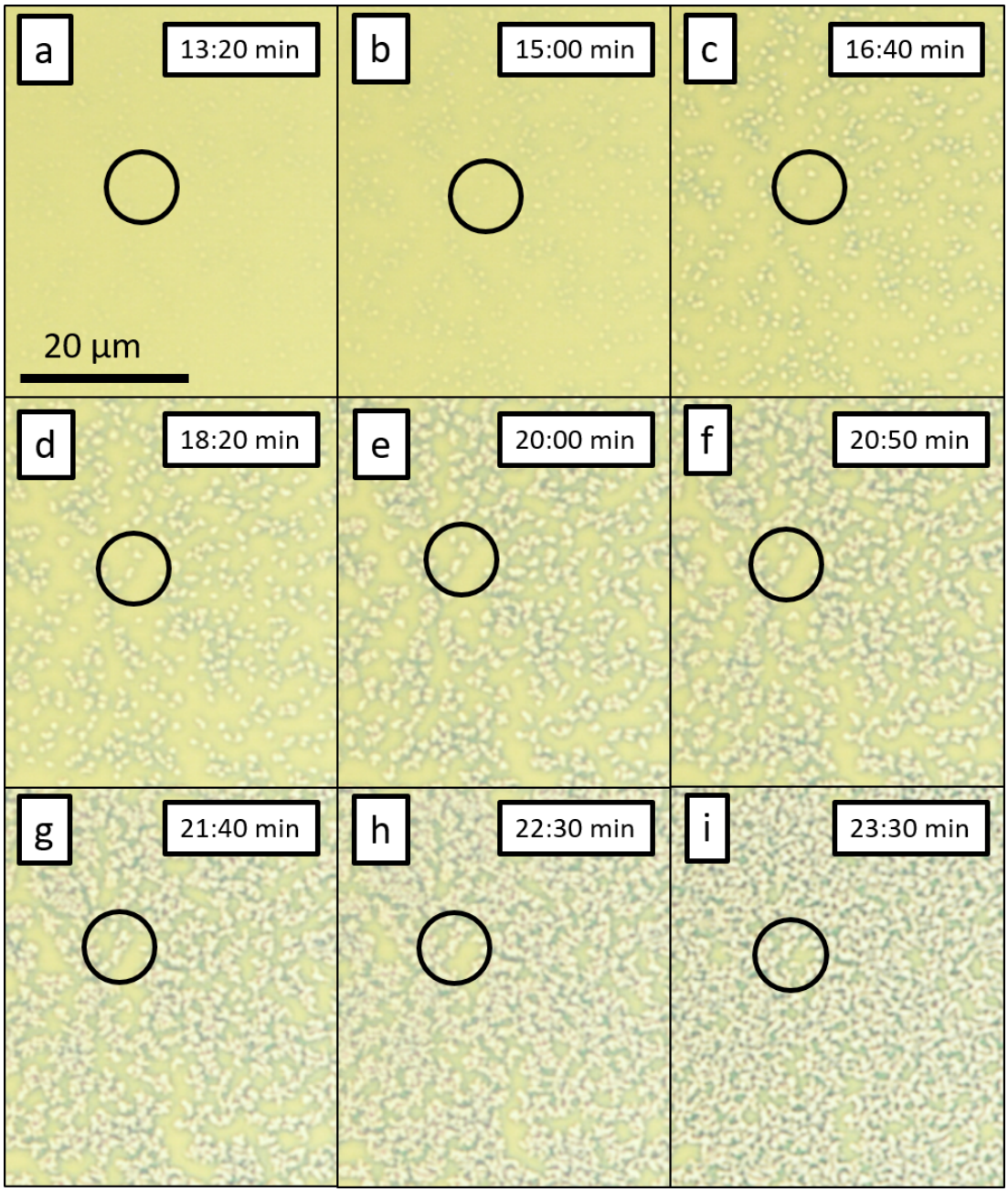

Figure 5.6: Selected frames from the video used for transmissivity analysis. While the dewetted parts are brighter than the areas with continuous film, the average brightness is reduced. The scale bar in ***(a)*** *applies to all images* ***(a-i)***

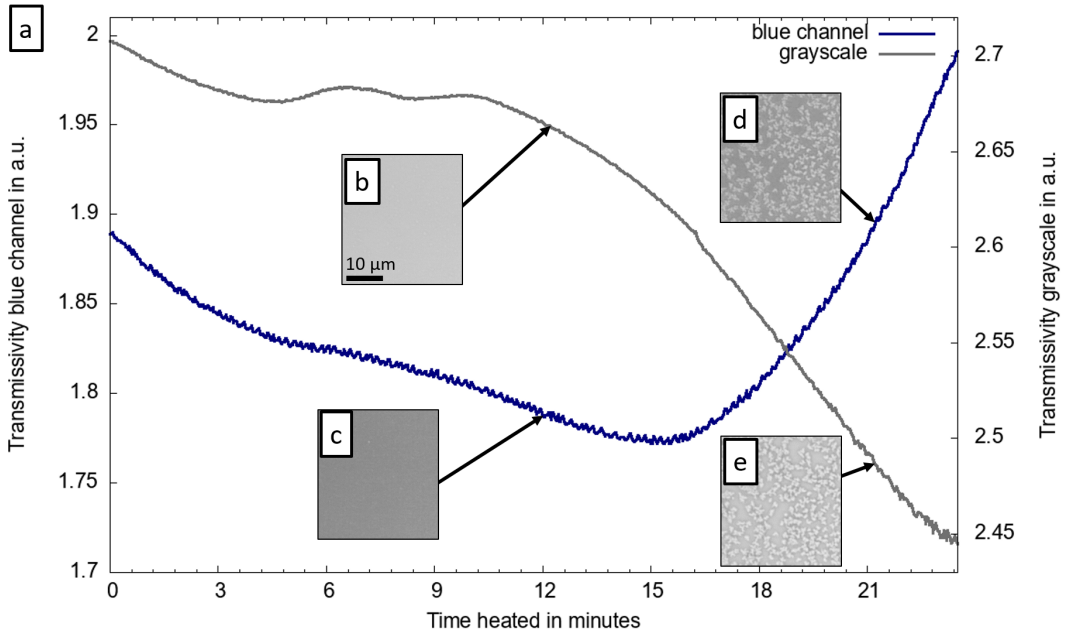

Figure 5.7: ***(a)****: Cumulative grayscale and blue channel values per frame as they are developing with increasing dewetted area. The graph shows a decline in the intensity of the light that makes up grayscale images, but a rise in intensity of the blue channel images. The insets* ***(b-c)*** *show the film before the dewetting process and insets* ***(d-e)*** *show the dewetting process. Scale bar in* ***(b)*** *applies to* ***(b-e)****. An improved contrast between covered and dewetted area when filtering for blue light is apparent.*

mission increasing with decreased area coverage. Insets **(b)** and **(c)** show the grayscale and blue channel image of the continuous film, insets **(d)** and **(e)** the dewetted layer. Changes in exposure time of the camera sensor in the microscope were corrected for.

Samples with a transparent window also allow for analysis of the thin film in a TEM. Figure 5.8 shows two micrographs. Because of the accurately resolved grain boundaries – as seen in images 5.8**(a)** and 5.8**(b)** – the grain size can be precisely determined with the line intersect method, which will be described in chapter 5.3. Images 5.8**(c)** and 5.8**(d)** show the dewetted state on the silicon nitride substrate. The TEM analysis reveals twin grain boundaries, which are characteristic for annealed metal films [60]. An increase in twin grain boundaries

with increasing heating time is a known phenomenon [61], as well as the influence of grain boundaries, including twins, on the electrical conductivity [62].

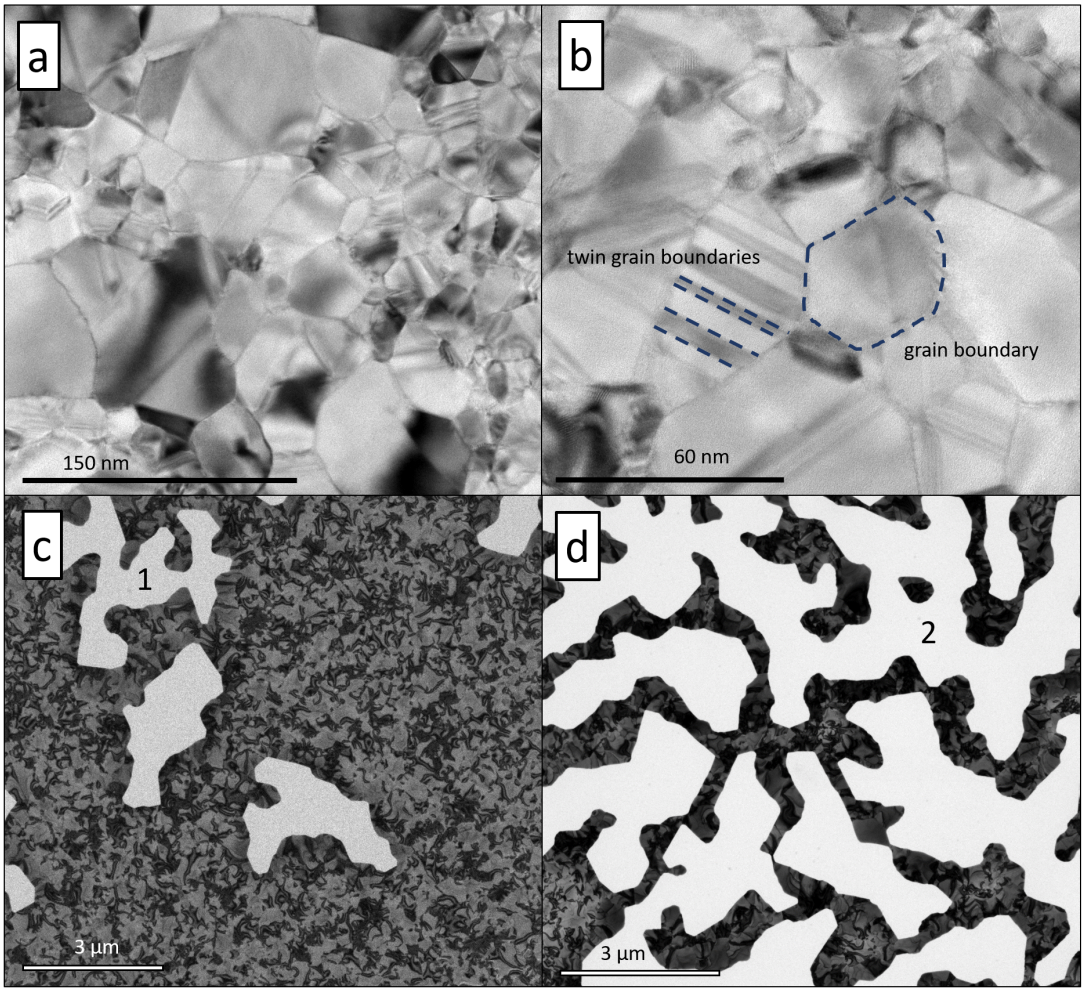

Figure 5.8: Micrographs taken with the TEM. ***(a)****: The high resolution of the TEM allows for precise grain size analysis with the line intersect method.* ***(b)****: both regular and twin grain boundaries can be seen with the TEM.* ***(c)****: The dewetting process begins with the formation of holes that grow and branch out (1).* ***(d)****: The different substrate does not hinder the dewetting process. The grown holes leave single particles and thin bridges of material (2).*

5.3 Grain size and its dependence on temperature

Temperature treatment directly influences the grain size of the heated material. While nanoscale grains are frozen in an unfavorable state when the temperature is low, they move towards an energetically more stable state when the atoms gain mobility due to increasing temperatures [63]. This leads to grain growth as an atom in the grain has a lower energy than a grain on an interface or grain boundary. In thin films this also leads to particle formation when heated long enough or to high temperatures [64].

The line intersect method was used to determine the grain size for the samples that were heated to different temperatures. For this a line pattern was overlaid on BSE images taken with the SEM and marks are placed whenever one of these lines intersects a grain boundary. The grain size can then be calculated by measuring the distances between the marks on a line. An example of this method is shown in figure 5.9 using an TEM image. Grain boundaries are emphasized with red, the helper lines that give the line intersect method its name are shown in blue.

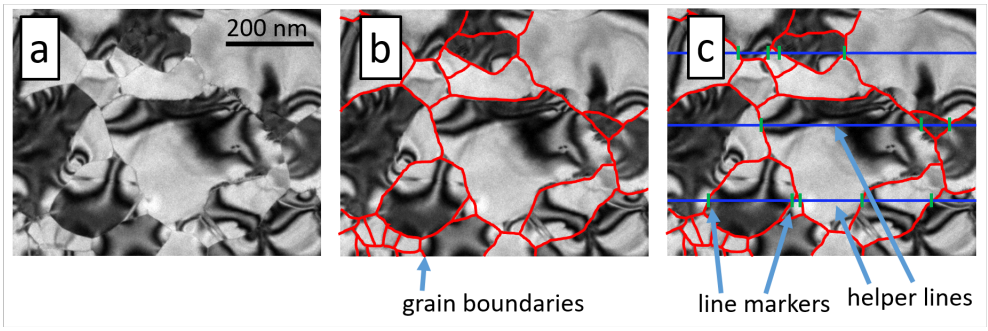

Figure 5.9: Example of the line intersect method. The blue lines provide a reference to measure the grain size. Whenever a grain boundary intersects one of these lines a mark is placed. Together with the scale, the distance between the marks results in the grain size distribution. Color and size of the lines and markers are emphasized in the figure for illustrative purposes.

The resulting values for the average grain size and the standard deviation of the data can be seen in table 5.1. Starting with a value of 36 nm in the measurement of the wafer heated for 2 minutes, the grain size rises continuously with

increasing heating duration.

Table 5.1: The average and standard deviation of the measured grain sizes. Line intersect method was used to determine the grain size after different heating times. The samples were cooled quickly after heating in an attempt to freeze the grain structure.

Heated for/minutes	Interrupted at/°C	Grain size/nm
2	76	36 ± 13
5	172	38 ± 12
12	393	102 ± 57
20	650	203 ± 95
23	698	220 ± 109

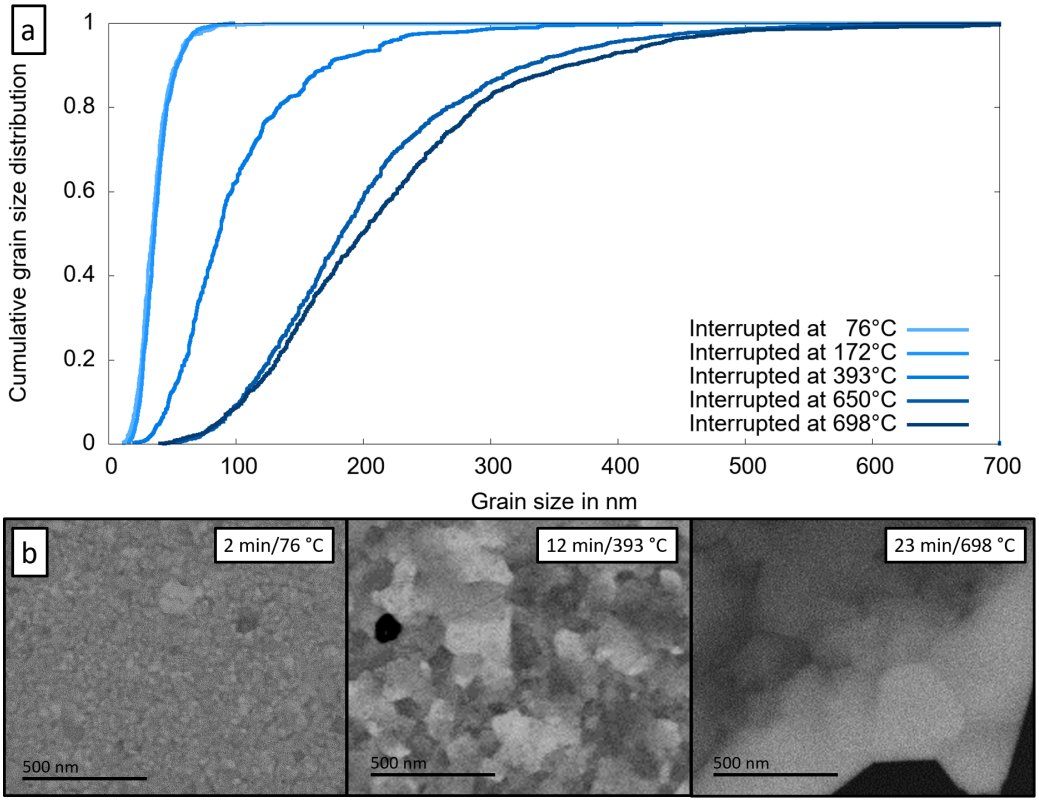

Figure 5.10: ***(a)****: Cumulative grain size distribution of the different samples. With increasing heating time the grains grow and the distribution spreads out.* ***(b)****: Representative BSD images of different heating stages.*

Figure 5.10 shows the cumulative grain size distribution and gives a more intuitive impression of the values presented in the table. The diagram illustrates the change in average grain size and the standard deviation visually, from the steep slope of the curves when the grain size has a low standard deviation in the beginning, to the flat, drawn out graph of the distribution with a high standard deviation after a longer heating experiment.

To visualize these values in the context of the measured resistance, they can be seen in figure 5.11 together with a reference curve of the *in situ* measured two point resistance in the system during heating. The grain size steadily increases with increasing heating time and temperature, with the exception of the measurement after 5 minutes of heating. Formation of the first holes after 12 minutes of heating and the start of the dewetting process at 20 minutes of heating does not keep the grains from growing. The final size of the grains is limited by the size of the particles that are formed in the dewetting process, and the size of the formed particles in turn is defined by the thickness of the deposited thin film [9, 65].

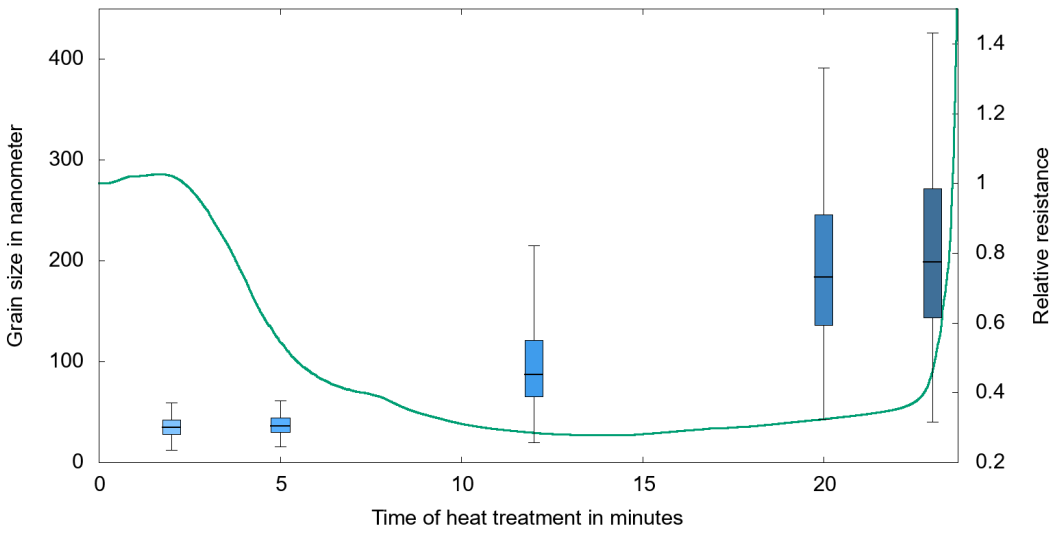

Figure 5.11: Box plot of the grain size of the interrupted samples together with a reference curve of the in situ measured two point resistance during heating.

5.4 EBSD measurements

In order to determine the orientation of the grains at different stages during heating, EBSD measurements were performed. For one sample with an untreated thin film and every heated sample, a grain orientation map was recorded, showing the orientation of the thin film at every pixel of the image. Using the Kikuchi patterns from the EBSD measurement, the orientation of the crystal at that point in the thin film can be determined. Resulting maps can be seen in figure 5.12 and show the development of the grain size as well as the grain orientation. While the resolution does not allow for a quantitative grain size analysis, it is apparent that the small grains at the beginning form into large grains during the heat treatment, leading to isolated monocrystalline particles when the film is fully dewetted. The grain orientation can be clearly seen despite the low resolution. An inverse pole figure gives a better view on the orientation of the grains in the image and is shown in figure 5.13. As can be seen in the untreated film, there is a dominant orientation in the [1 1 1] direction. In comparison to the film heated to 698 °C, it becomes apparent that the grains move to further concentrate to point along the [1 1 1] direction.

5.5 Resistivity measurement before heat treatment

In order to determine the exact resistivity of the deposited thin film, a four point measurement was performed on samples in the as-deposited state. The resistivity measurement was performed on thin films with a thickness ranging from 5 nm to 120 nm. Figure 5.14**(a)** shows a photograph of the deposited gold thin films. The difference in thin film thickness results in a visible color gradient from the dark color of the underlying silicon oxide towards the gold color of the deposited film that becomes more pronounced with increasing thickness. The resistivity measurement reveals at which thickness the thin film becomes non-conductive, because parts of it are no longer connected. The resulting measurements of sheet resistance are plotted in figure 5.14**(b)** and show the inverse sheet resistance together with the deposited film thickness. A low value therefore corresponds to a high sheet resistance of the thin film. When plotting the inverse sheet resistance

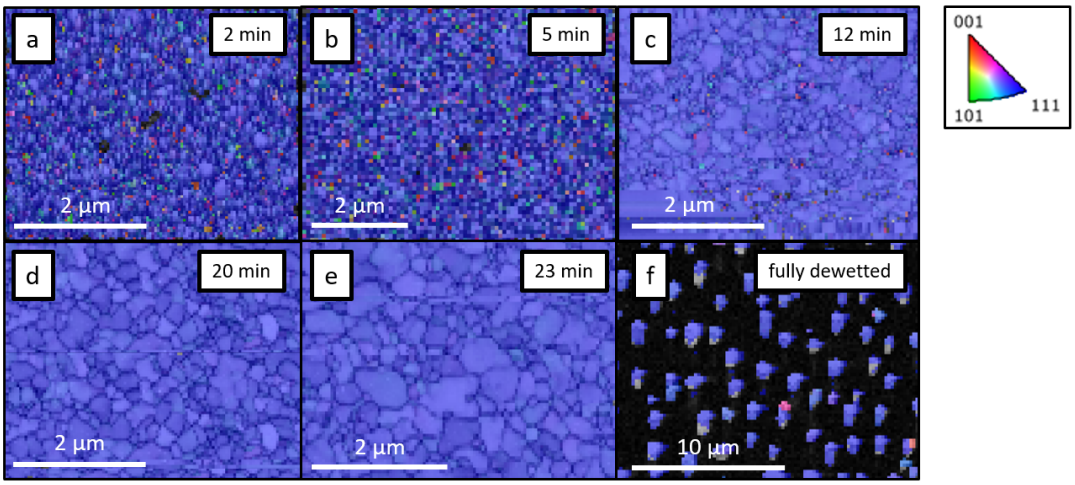

Figure 5.12: EBSD maps of samples heated to different temperatures, from untreated up to a fully dewetted state. Coloring is done in reference to the inverse pole figure of the out of plane orientation. The general trend in grain size growth and the orientation of the thin film is visible.

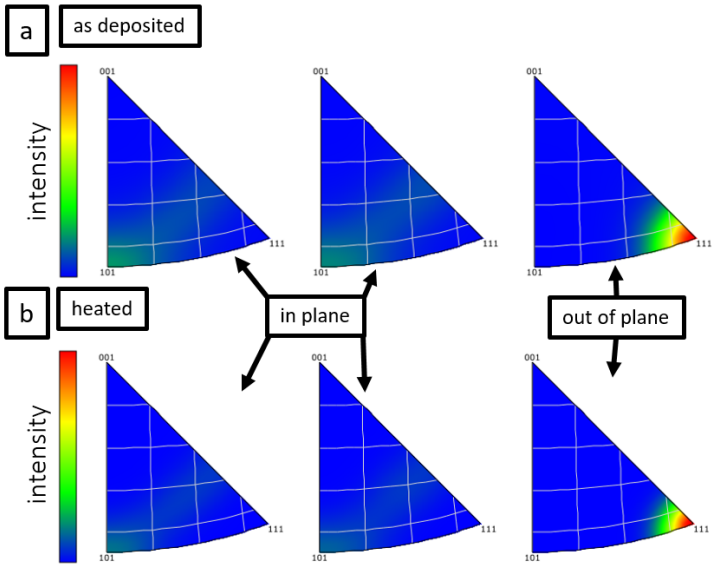

*Figure 5.13: Inverse pole figures of the EBSD data in figure 5.12, from the untreated sample **(a)** and the sample heated to 698 °C **(f)**. While the heating does result in a slight change and concentration of the orientation, the grains start closely aligned already.*

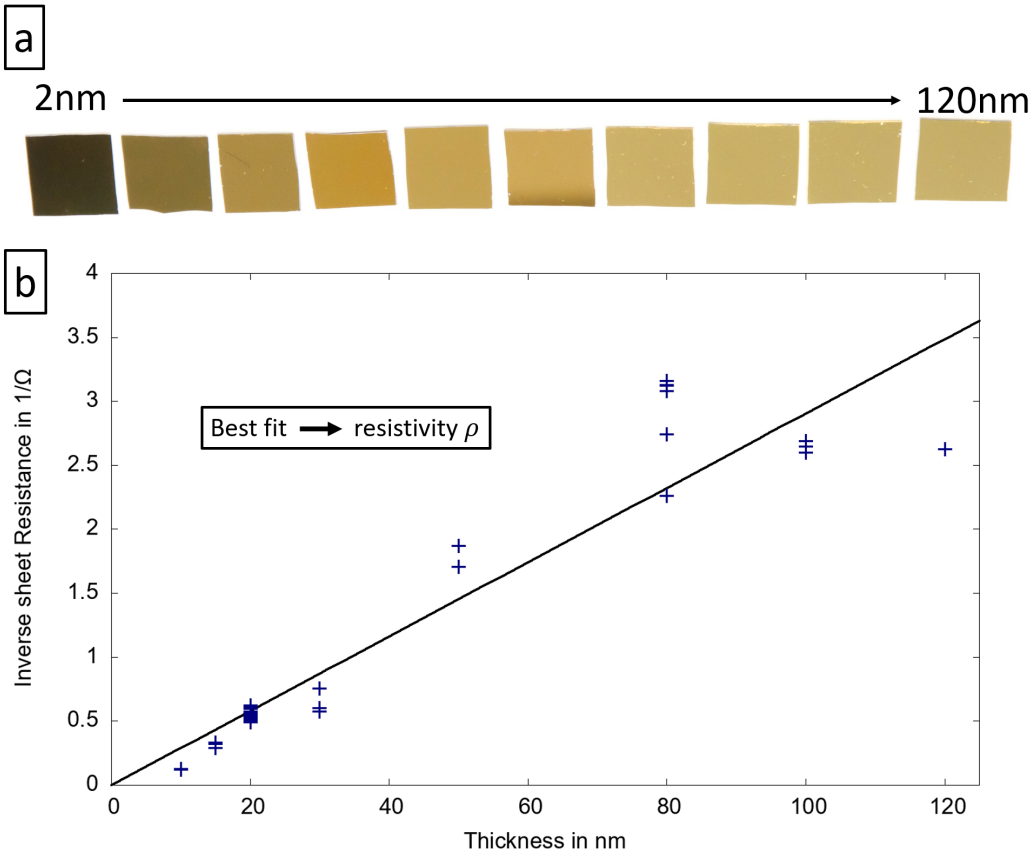

Figure 5.14: ***(a)*** *The difference in thin film thickness from* 2 nm *to* 120 nm *results in a visible color gradient. The dark color shows more of the underlying silicon oxide, the thicker films show a more golden color. When using a layer of only* 2 nm *or* 5 nm *thickness, the film was not continuous and carried no electricity. It was therefore excluded from the experiment.* ***(b)*** *The measured sheet resistance for the gold thin film with a thickness ranging from* 10 nm *to* 120 nm*. There is no increase in sheet resistance at a film thickness of* 20 nm*, which is evident by the marks for this thickness all lying on the line of best fit.*

over the film thickness, a linear fit results in the resistivity of the thin film, as given by equation 2.5. The measured values are higher and more spread out than the true values, because no correction factors have been applied (see appendix B).

This measurement was done across a wide range of thin film thicknesses to

make sure the resistivity does not increase due to island formation in ultra thin films, but only due to the decrease in thickness. With this method no island formation could be found for films with a thickness of 20 nm, which were used for the following experiments.

The resulting resistivity of the deposited gold layer was determined to be $(26.92 \pm 0.74)\,\mathrm{n\Omega\,m}$. The resistivity of bulk gold is $(22.20 \pm 0.26)\,\mathrm{n\Omega\,m}$ [66,67,68], but the resistivity of thin films is higher [69], depending on the quality of the interfaces and the amount of defects, like grain boundaries, in the thin film.

5.6 Resistance change during heating

For every wafer that was contacted electrically during heating, the change in resistance was recorded. This allows for a direct insight into the electrical properties during the experiment. An absolute value for the electrical resistance does not represent the actual resistivity correctly, as the two point measurement introduces parasitic resistances in the wires and contacts. Different samples will also show a different distance of the contact probes on the thin film.

Figure 5.15 shows an example curve recorded during the process. The interesting parts are the significant drop in resistance from three to 13 minutes (figure 5.15 part 1) and the sharp rise in resistance starting at 23 minutes (figure 5.15 part 2). Reason for the change in resistance in part 1 is the curing of the contact paste, which improves the contact between the wire and the thin film, and the grain growth, which removes grain boundaries that increase the resistance due to scattering of electrons [70, 71, 72, 73]. Despite being allowed to settle for more than twelve hours, the optimum conductivity of the contacts was only reached by heating. The sharp rise in resistance at the end of the measurement in part 2 is due to increased hole growth. As more material is cut off from the current conducting path, the cross section that is available for the charge to flow is restricted further, which leads to an increase in resistance according to equation 2.5.

In figure 5.16 the change in appearance during heating can be seen. The images are extracted from the video recorded during heat treatment. As seen in pictures 5.16**(a-c)** no noticeable change is visible using light microscopy. The

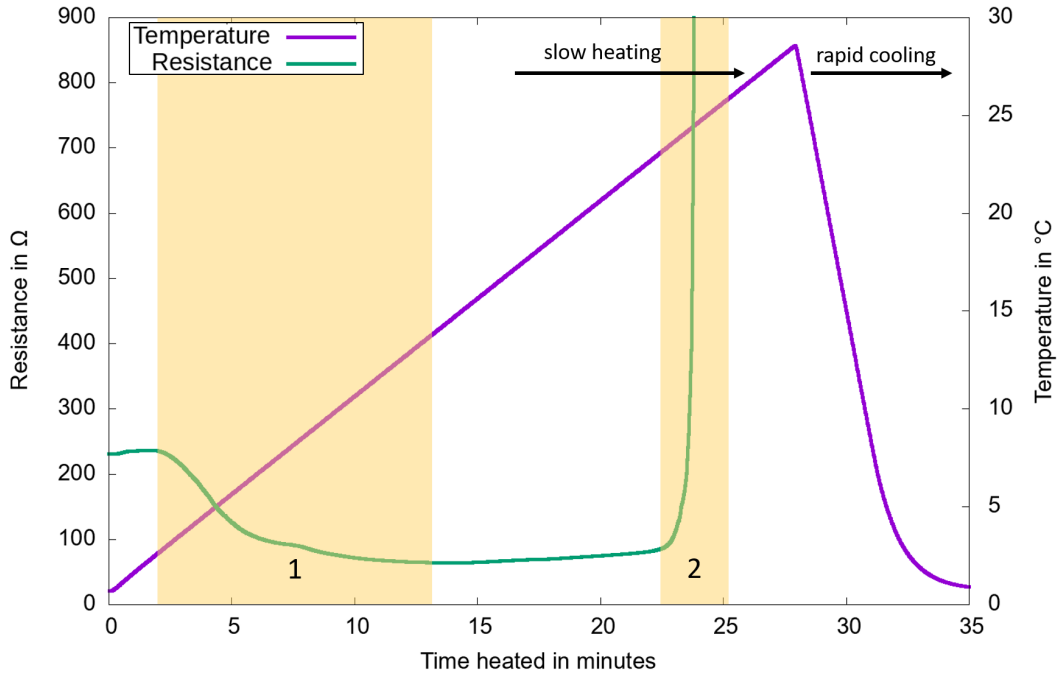

Figure 5.15: An example for one of the recorded resistance and temperature graphs. The temperature is increased by 30 °C *per minute up to* 850 °C*, at which point it is decreased at a rate of* 200 °C *per minute in order to freeze the microstructure.*

corresponding images 5.16**(g-i)** from the electron microscope show a change in grain size. Starting with image 5.16**(d)** the hole formation and subsequent hole growth can be seen in the images taken with the light microscope. Image 5.16**(d)** shows more, but smaller holes than image 5.16**(e)**, which was heated 3 minutes longer. This is due to small variations in the deposited thin film. The grains size increases further as seen in the micrographs 5.16**(j-l)**, taken with the electron microscope. Pictures 5.16**(f)** and 5.16**(l)** show a fully dewetted wafer. While single particles are visible in the light microscope, the resolution is not enough to properly image them. The SEM can resolve the shape of the gold particles, however.

The same *in situ* resistance measurement was also attempted with the samples used in transmission mode. Due to their small size of 2 mm and the resulting contacting problems, no complete measurement run could be performed. As such

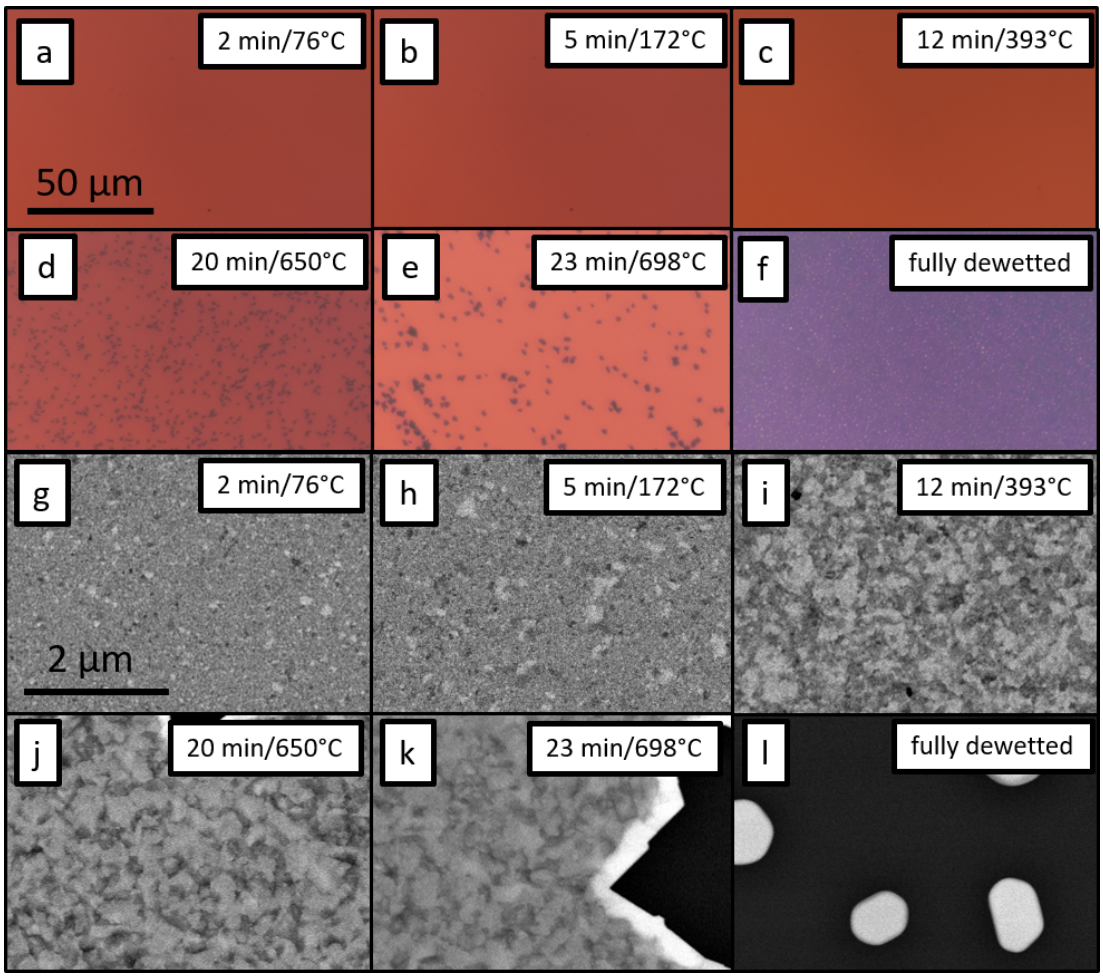

*Figure 5.16: The development of the thin film with increasing heating time and temperature. The top row (**(a-f)**) shows frames from the video recorded during heating in the light microscope. The bottom row (**(g-l)**) shows images taken with the SEM after cooling down the wafer.*

only the fact that the general trend of the *in situ* measurements of both transmittance and reflection samples show no significant deviation from each other will be stated.

5.7 Resistivity measurements after heat treatment

Because the heating stage only provides two points for electrical contact, the resistivity can not be measured while heating. In order to determine the resistivity

of the wafers after treatment, a four point measurement was performed after the samples were quickly cooled down. This complements the *in situ* two point measurement and allows to put the *in situ* resistance into context.

Placing four probes on a wafer that fits into the heating stage – and is therefore smaller than 1 cm in any direction – proved to be a tricky challenge, but was solved with the support of a helping hand tool. The measurement was performed under a stereo microscope, which allows the exact reading of the probe distances. Using ImageJ [58], the distances between the probes and the shape of the rectangle were measured in order to apply the correct factors for the resistivity measurement.

The resulting resistivity and sheet resistance values can be seen in table 5.2. Figure 5.17 shows the results in a plot together with the *in situ* resistance curve as well as the bulk resistivity [66, 67, 68] to put the results into context. The third measurement after 5 minutes of heating is abnormally high due to scratches introduced when contacting the wafer for the four point measurement. Removed material decreases the area of the thin film that is able to carry current and therefore increases the resistance. Some of the measurements are lower than the bulk value of gold, but fit well to the *in situ* resistance value. Reasons why the measured resistivity is lower than the bulk resistivity are discussed in chapter 6.6.

Table 5.2: The measured resistivity and sheet resistance after heat treatment.

Heated for/minutes	Interrupted at/°C	Resistivity/nΩ m	Sheet resistance/Ω
untreated	untreated	26.9	1.35
2	76	21.4	1.07
5	172	30.7	1.54
12	393	16.7	0.84
20	650	18.2	0.91
23	698	113.3	5.67

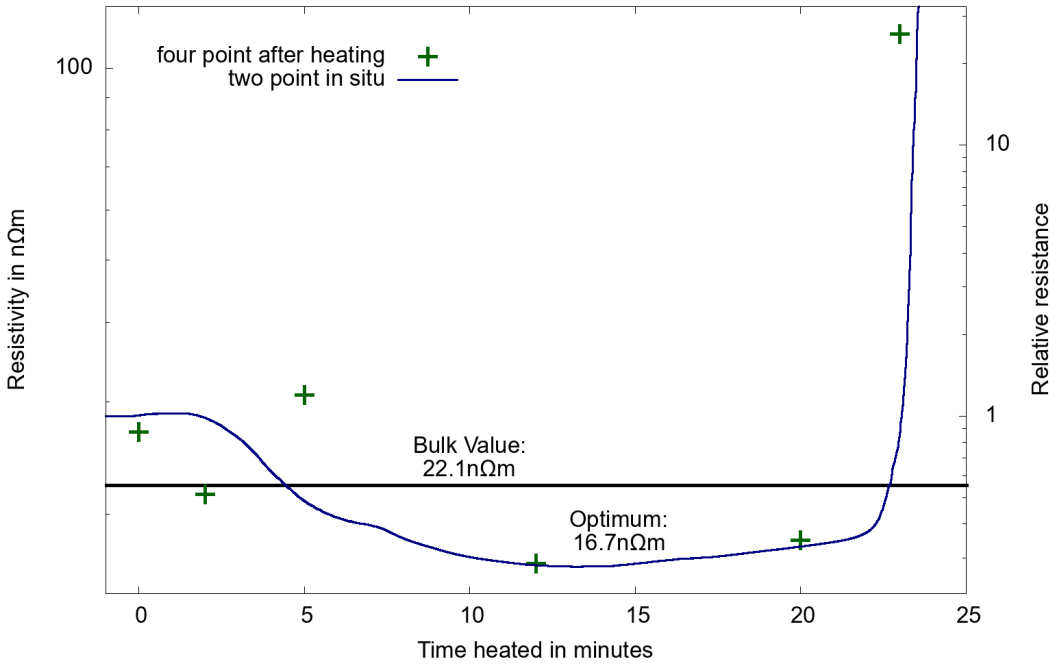

Figure 5.17: Resistivity measurement after heating. The green plot provides a reference to the in situ two point measurement.

6 Discussion

The aim of this work was to find the optimal grain size to maximize electrical conductivity of the deposited thin film. Different parameters were measured – with a focus on grain size and resistivity – to correlate the development of the thin film during heating. In this chapter the results presented in the previous chapter 5 will be analyzed in depth and discussed.

6.1 Influences of silver contact paste on dewetting behavior

The first experiments were done with silver contact paste [54] to connect the wires with the thin film. This provides a good contact, but is only possible for experiments that are not subject to elevated temperatures. As silver has a lower melting point than gold [66] and is fully miscible for all mixture ratios [74], it diffuses into the gold thin film near the contact and the resulting alloy has a lower melting point than pure gold. As dewetting is a temperature dependent phenomenon, a lower melting point leads to dewetting behavior at lower temperatures. The resulting non-homogeneous dewetting behavior can be seen in figure 6.1. The thin film is continuous far away from the contact point, but fully dewetted near the silver paste. A region between the dewetted silver-gold alloy and the silver contact is continuous as well.

For the correlative test series, only gold paste [55] was used. This does not lower the melting point of the thin film and therefore leads to consistent dewetting in the gold layer. The dewetting behavior when contacting the thin film with gold paste can be seen in figure 6.2**(a)**. Images 6.2**(b)** and 6.2**(c)**, captured in the light microscope and SEM respectively, show parts of the thin film with higher magnification and homogeneous dewetting between contacts.

6.2 Bubble formation during heating

When heating the thin film above 690 °C, bubbles start to form. This leads to a delamination of the gold layer from the silicon oxide substrate. Figure 6.3 shows

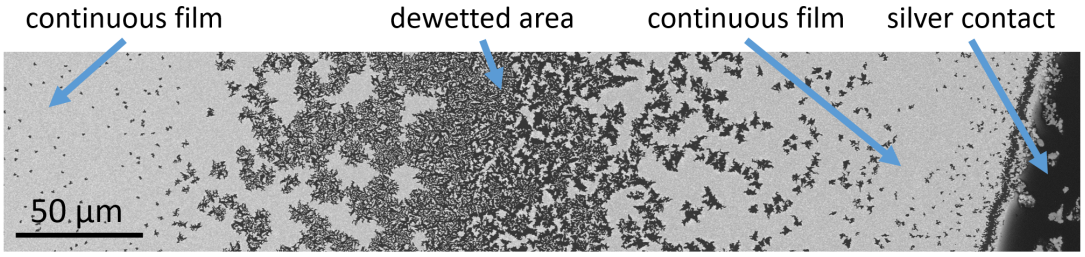

Figure 6.1: Image taken with a SEM showing the dewetting behavior close to a silver contact. Starting from the contact point is a continuous thin film with small holes. At a distance of about 200 µm *from the silver paste the gold film is dewetted, turning continuous again further away from the contact.*

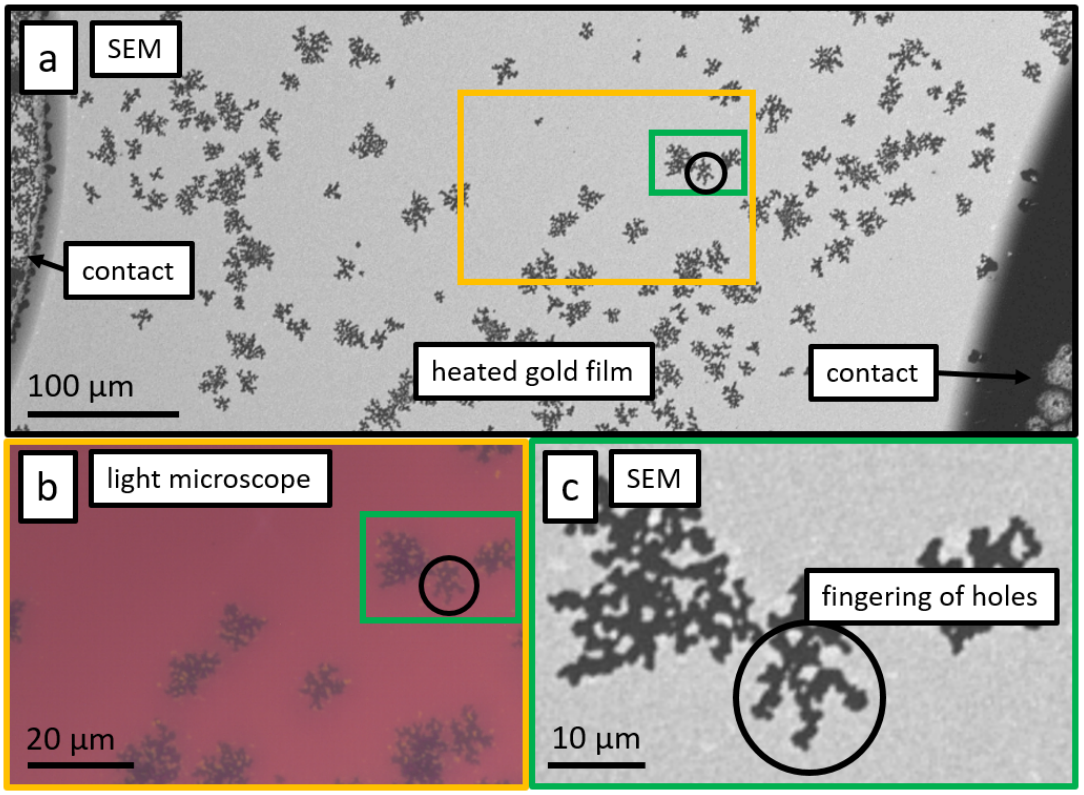

Figure 6.2: Dewetting process of the thin film when contacted with gold paste. ***(a)****: Overview of the thin film between contacts. No increased dewetting rate can be seen near the contacts.* ***(b)****: Area captured in situ with the light microscope.* ***(c)****: Part of the light microscopy image shown with a higher magnification and in the SEM.*

the bubbles as seen in the light microscope as well as SEM micrographs of the collapsed bubbles after cooling down the wafer.

Bubble formation is a known phenomenon in thin film systems [75, 76]. The driving force behind this behavior is the oxidation of residue between the thin film and the substrate and the build-up of thermal stresses. Despite the bubbles not preventing dewetting of the thin film as seen in figure 6.3(**c**), experiments with bubble formation were excluded from the following evaluation. For further experiments the heating stage was flushed nitrogen before heating to prevent oxidation and the formation of bubbles.

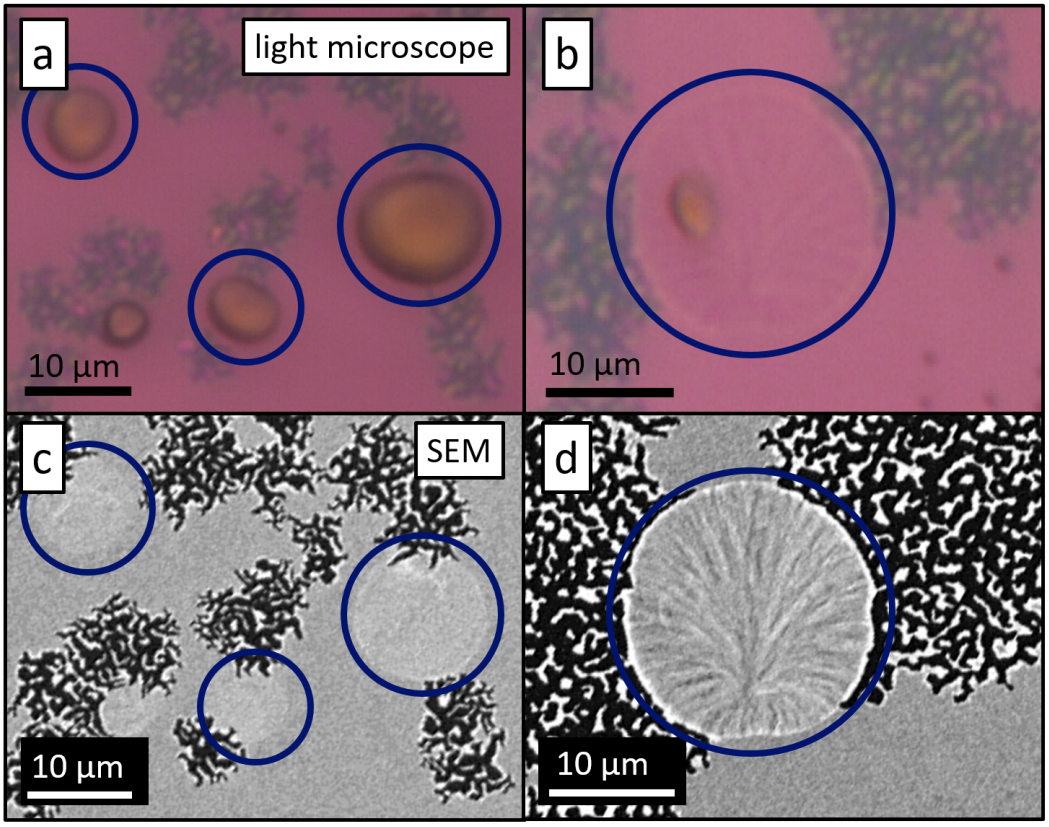

Figure 6.3: If the atmosphere contains oxygen, bubbles can form during the heat treatment. ***(a)****: Inflated bubbles as seen during heating.* ***(b)****: Collapsed bubble in the light microscope.* ***(c)****: SEM micrograph of collapsed bubbles that already dewetted. The remaining thin film after bubble formation and deflation is more resistant against dewetting than the normal thin film.* ***(d)****: A non-dewetted, deflated bubble in the SEM.*

6.3 Transmissivity change during dewetting

Considering the dewetting behavior, an increase in transmissivity and a decrease in area coverage with increasing heating time is expected. Figure 6.4 shows the development from a continuous film to the fully dewetted state. Figure 6.4**(a)** shows the thin film in the as deposited state with a very small grain size. After the thin film is dewetted to a non-conductive state, the area coverage is minimized. An example of this state can be seen in figure 6.4**(b)**. In figure 6.4**(c)** the transition from a continuous film to the dewetted parts of the layer can be seen.

The development of area coverage with increased dewetting was confirmed with the help of a binarization function of the *in situ* light microscopy images. The change in transmissivity could be correlated to the change in area coverage with an intensity measurement of the blue channel of the RGB images but not by measuring the intensity of the grayscale images.

Figure 6.5 shows a close up of the dewetting process in transmission mode. The image 6.5**(a)** shows a TEM micrograph of the edge of dewetted areas. Images 6.5**(b-d)** were taken with the light microscope and show the same part of the dewetting process, but are displayed in color (6.5**(b)**), grayscale (6.5**(c)**) and were filtered for the blue channel (6.5**(d)**).

A drop in transmissivity is calculated with decreasing area coverage of the thin gold film when using grayscale images instead of the blue channel of the RGB images, as was shown in figure 5.7. This is an unexpected result, given that dewetting leads to higher transparency as more and more substrate is uncovered. Inspecting the covered and dewetted parts of the sample also shows a higher light attenuation for the parts covered with the thin film when compared to the uncovered areas.

A likely reason for the decrease in calculated transmissivity of the grayscale images is the increase in thickness near holes in the thin film. The material from the hole accumulates at the rim of the holes as part of the dewetting process [59]. This increases the thickness of the grains at the edge of holes and leads to a higher attenuation of the light passing through the thin film near dewetted areas, making the edge of holes appear darker in the recorded images.

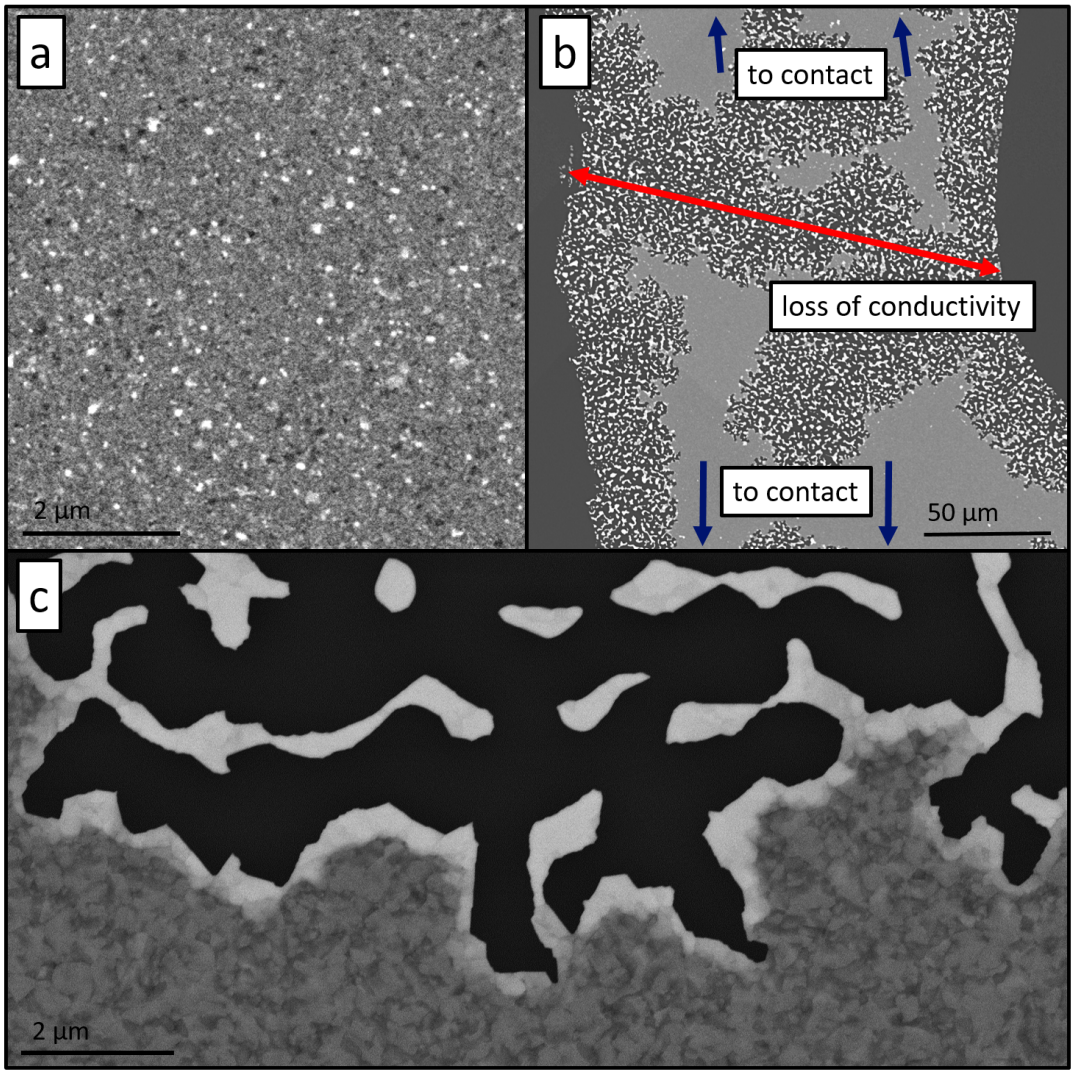

*Figure 6.4: Development from a continuous film (**(a)**) to a non-continuous film that shows the substrate in many parts which were previously covered (**(b)**). No electricity can flow between the two contact points. Image **(c)** shows the transition from the dewetted to the continuous part.*

When using the blue channel of the RGB images, a simple preprocessing of the input data is performed, filtering the image by the wavelength to which the blue pixel detectors are sensitive to. This filter effect darkens the thin film parts of the image relative to the dewetted areas and increases the correlation of the

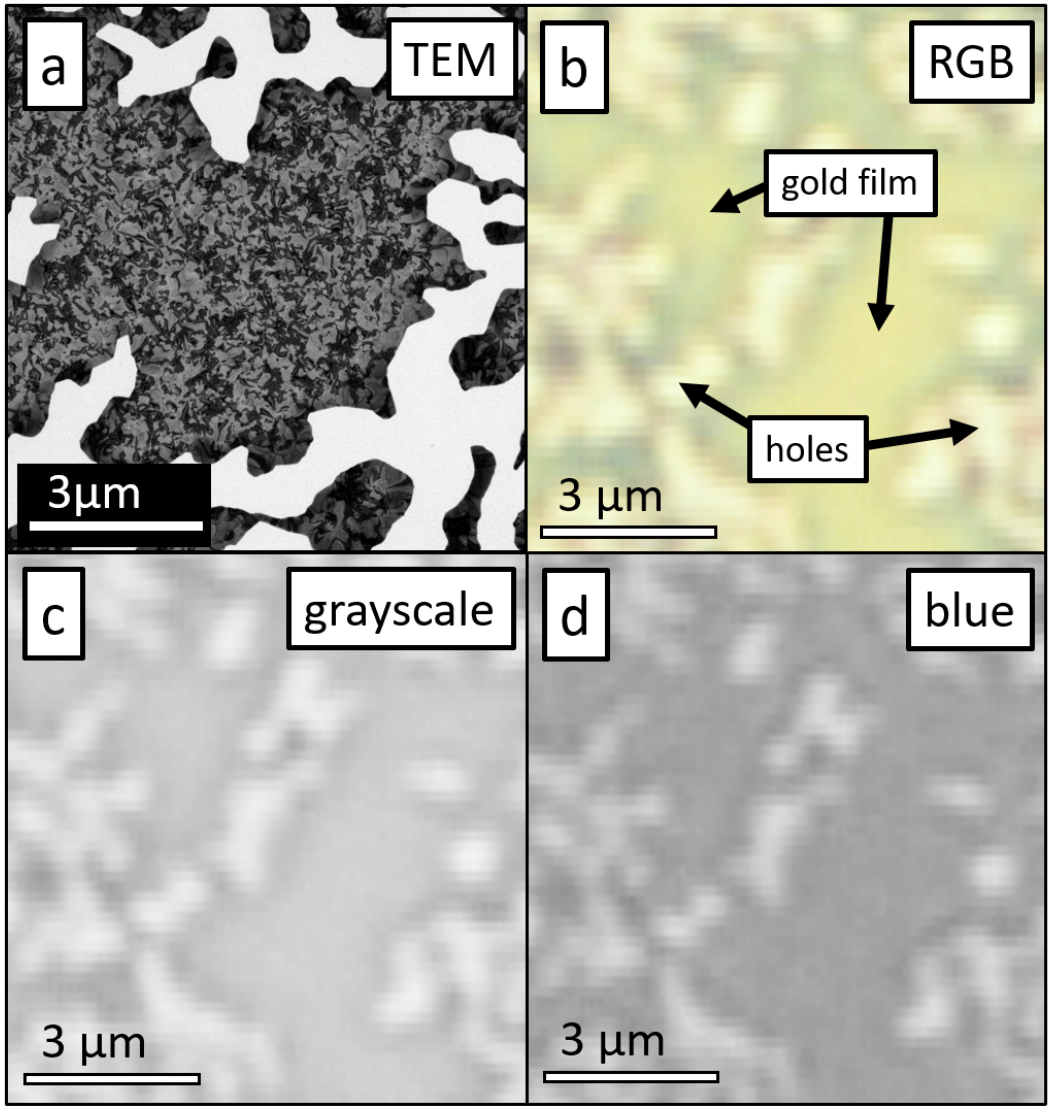

Figure 6.5: Close up of the transition from thin film to substrate. ***(a)****: TEM image of the transition from thin film to substrate.* ***(b)****: Light microscopy image with all three color components. The transition from thin film (yellow) to substrate (white) shows a discoloration.* ***(c)****: Grayscale light microscopy image. The rim is still darker than the thin film, but the difference is less visible than in in the RGB image.* ***(d)****: Blue channel of the original RGB image. Filtering for this color results in a much darker film with less contrast to the rims, but an improved difference to the dewetted area.*

calculated transmissivity value with the perceived change in brightness. Filtering the image with the blue pixel detectors is therefore a better measurement than using the grayscale image.

The value of the calculated grayscale transmissivity value is tainted by the increased light attenuation at the edge of holes, which gives the impression of decreasing transparency. While the effect is minimized by using the blue channel to segment the data before analysing it, the drop in transmissivity value up to 15 minutes into heating shows that the effect can not be fully eliminated. An additional important indicator is therefore the area coverage during heat treatment. As the pixels at the edge of the thin films – which appear darker than the pixels of the continuous film – have to be counted as either covered or not covered in the area coverage analysis, they can not skew the result of the area coverage measurement as much as a pixel with no brightness value can skew the result of the transmissivity value.

6.4 Area coverage development during heating

Analyzing large data sets, like the frames extracted from the *in situ* light microscopy video requires computational support. Determining the area coverage of a frame computationally is done by separating the image into a bright and a dark area. There are several methods available to determine the split automatically. In this work a constant threshold, Otsu binarization [77] and an adaptive threshold were considered.

Generally a simple solution is preferred, like a constant threshold for all images in the sequence. Such a straight forward approach was not possible in this work, because exposure of the camera sensor changes during the experiment. This introduces jumps in the measured area coverage as well as coverage values of exactly 0 or 1, which is never the case when analyzing the recorded frame manually.

Otsu binarization works well in frames where the brightness distribution of all pixels is bimodal. It automatically calculates the best threshold for every frame by minimizing the intra class variance of intensity [77]. This threshold is then applied

to the whole frame. The method did not segment the frame as intended for this work, as the thin film is often unevenly illuminated under the light microscope. A single threshold then leads to the computer viewing the brighter part of the image as fully covered and the darker part as fully dewetted.

In order to get rid of the uneven brightness across the image, a local average brightness level has to be subtracted from the base image. One approach would be to fit a function – with the pixel coordinates as input and the brightness value as output – to the image. Subtracting this best fit from the input image leaves only the local brightness differences. Another solution is to blur the image with a very large blur radius. This removes any details and only leaves the uneven illumination visible. This background can then be subtracted from the input image, resulting in only leaving the local brightness differences as well. For this work the Gaussian background calculation was chosen, as defining a function to properly fit the uneven illumination without being skewed by the brightness difference of dewetted and covered areas is difficult. Additionally, OpenCV [57] has a mathematical equivalent to the Gaussian background subtraction already implemented with the `adaptiveThreshold` function.

The difference between a binary and a locally adaptive threshold can be seen in figure 6.6. Image 6.6**(a)** shows the input image that has to be divided into area that is covered with the gold thin film and area that shows the substrate. Figure 6.6**(b)** shows the light intensity background of the grayscale image. Due to uneven illumination in the light microscope the dewetted area at the bottom left of the input will have the same color as the covered area at the top right of the image. This is corrected for by the intensity background. The inset shows a high contrast version to better visualize the differences that throw off the constant threshold binarization. To highlight the difference between the `adaptiveThreshold` function and the constant threshold, images 6.6**(c)** and 6.6**(d)** show the binarized version of the grayscale input shown in figure 6.6**(a)**. The constant threshold overestimates the area coverage in the darker bottom left corner of the image and underestimates the coverage in the brighter top right corner. Because of this uneven illumination the area coverage can only be accurately determined with

the `adaptiveThreshold` function that takes the background illumination into account.

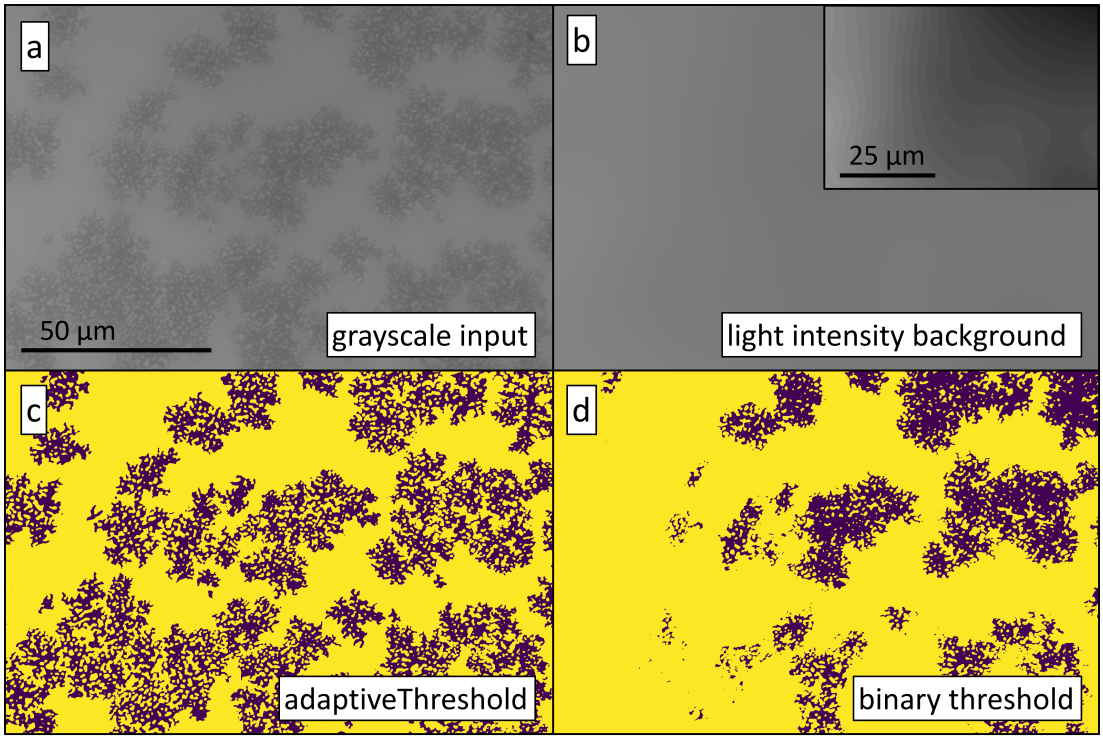

Figure 6.6: The process behind the calculation of the ***`adaptiveThreshold`*** *function. Scale bar in* ***(a)*** *applies to images* ***(a-d)****.* ***(a)****: The grayscale input image.* ***(b)****: Light intensity background of the input image.* ***(c)****: Image binarized with the* ***`adaptiveThreshold`*** *function.* ***(d)****: Image binarized with a constant threshold.*

A critical task when using such automated methods of evaluation is to determine the constants that are passed to the function. This has no analytical solution and must be done manually. For this task selected frames were analyzed by hand with the help of ImageJ [58] and a true value of area coverage determined. The same frames were analyzed with the automated technique with different arguments to the function. The two results were then correlated to determine the best values for the constants `blocksize` and `c` to be `150` and `2` respectively. The correlating plots can be seen in figure 6.7.

In order to increase the transmissivity and decrease the area coverage, better

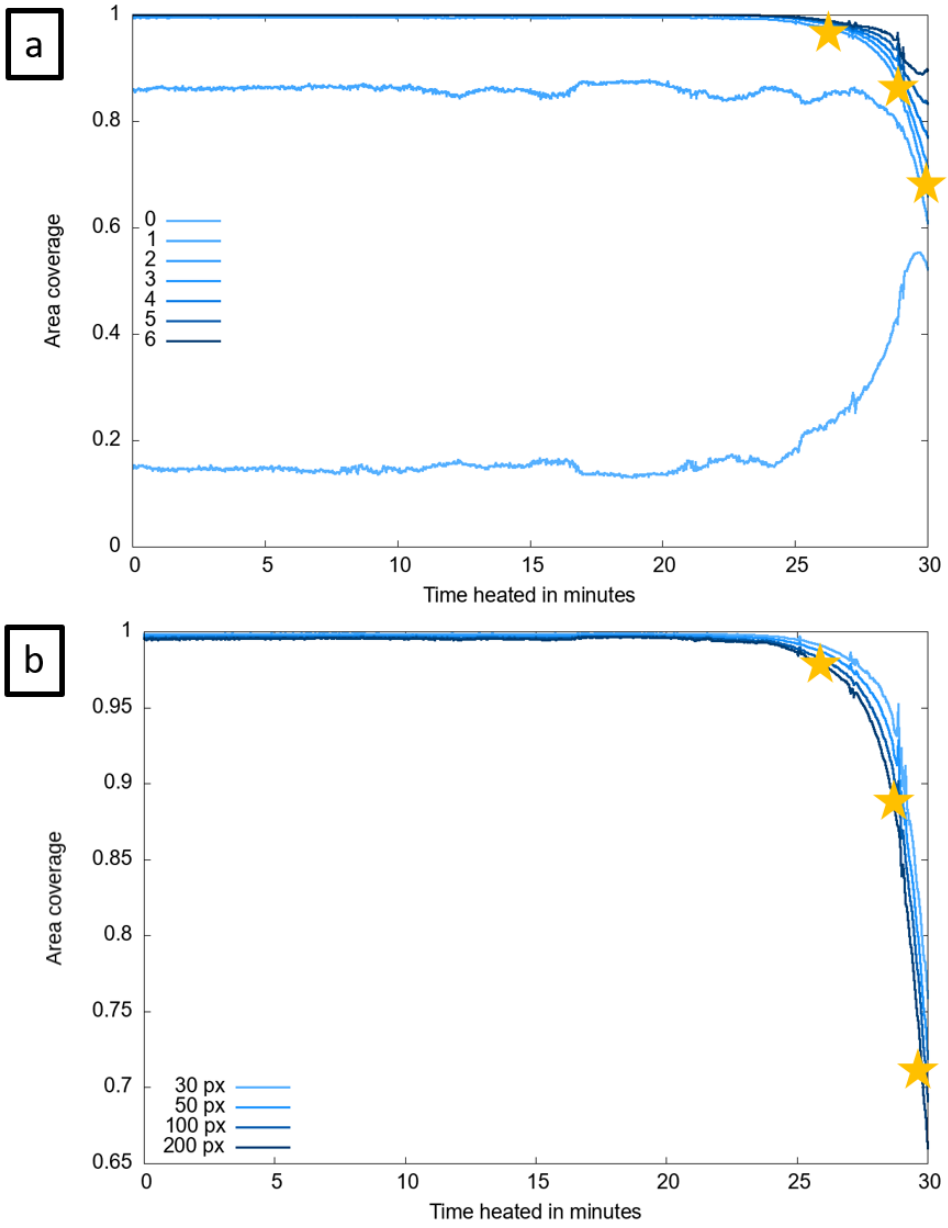

Figure 6.7: Plots of the area coverage with different arguments. Manually determined coverage values are shown as yellow stars. ***(a)****: Changing the value of* `c` *has great effect on the calculated area coverage.* ***(b)****: The* `blocksize` *doesn't have as great of an effect, but the plot shows that small values overestimate the area coverage.*

control of the dewetting process is needed. If local defects can be eliminated and the samples heated equally across the whole thin film area, a uniform dewetting process would be possible. Another concept for improvement is the use of prepatterned substrates [78,79,80]. The dewetting process can be controlled by creating areas that require high deformation in the thin film or high interfacial energies between the thin film and the substrate for the thin film to be stable. Using a pattern of high and low energy places, the dewetting process can be regulated and forced into a predetermined shape.

6.5 Influence of the temperature on grain size and grain orientation

In general, during heat treatment grain growth and a coarsening of the microstructure is expected [81]. This phenomenon can be used to influence the electrical properties of the material by eliminating defects [70,71,72,73]. As grain boundaries are a type of defect they scatter the electrons and increase the resistance. An increase in grain size also reduces the number and area of grain boundaries in the thin film, thus leading to an increase in conductivity. This can also be seen in figure 5.17 which shows the four point measurements after heat treatment.

The same phenomenon of grain growth can be seen in thin films where it ultimately leads to particle formation [64, 82]. Examples of this are shown in figure 6.8. TEM images 6.8**(e-h)** are of the same sample as the light microscope images 6.8**(a-d)**, respectively. The phenomenon of grain growth can also be seen in concrete numbers in table 5.1. Since grain boundaries are the main reason for the increased resistivity of thin films [10,11], the heat treatment and the resulting grain growth improves the conductivity of the deposited gold layer.

The expected result of the EBSD measurement of the untreated wafer was a thin film of randomly distributed grains. During the unheated deposition process, the grains should be too slow to rotate towards a uniform, energetically favorable position. Instead the measurement reveals an almost uniform grain orientation of the untreated film, which suggests that the grains are free to rotate in the

deposition process and do not need the very high temperatures of the heat treatment to do so. This suggests that the deposition process already produces high temperatures or that the deposited atoms have enough energy to move towards an energetically favorable state.

Another explanation could be that the EBSD measurement can not detect the small grains of the E-Beam deposition process. The initial film has an average grain size of 36 nm, while the EBSD measurement was set to a pixel size of 40 nm. This means that the results for a single pixel in the EBSD map of the unheated thin film are not necessarily the EBSD measurement of one single grain, but might be the result from the illumination of multiple grains with different orientations. A comparison of the change in grain orientation from the untreated to the heated sample is nevertheless possible and an inverse pole figure of the grain orientations is shown in figure 5.13.

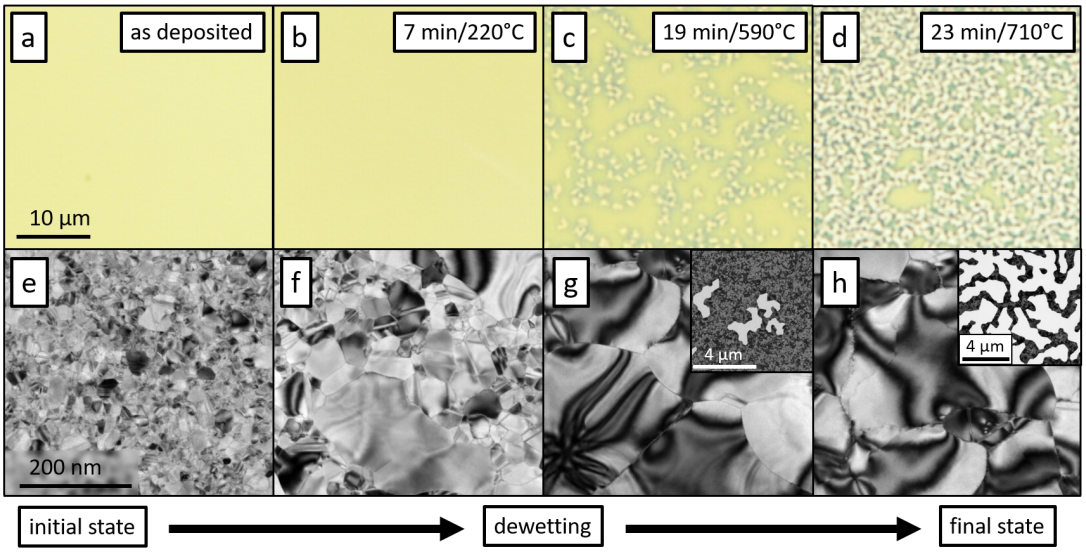

Figure 6.8: Development of grain growth seen in the TEM. ***(a-d)****: Images of the heated samples taken by the light microscope in transmission mode. The scale bar in* ***(a)*** *applies to images* ***(a-d)****.* ***(e-h)****: Corresponding views of the samples in the TEM. The stark grain growth between the different samples is clearly visible. Scale bar in* ***(e)*** *applies to images* ***(e-h)****. Insets in figures* ***(g-h)*** *show the morphology of the sample at a lower magnification.*

6.6 Correlating resistivity with grain size and dewetting behavior

Optimizing the resistance of the thin gold film was the main focus of this work. The best resistivity value measured was reached after heating for 13 minutes to 393 °C, resulting in a measured resistivity of 16.7 nΩ m, a stark improvement when compared to the resistivity of the untreated thin film of 26.9 nΩ m. This is lower than the value of (22.20 ± 0.26) nΩ m for bulk gold [66, 67, 68]. As is predicted in theory [27, 29] and shown in literature [83, 84], thin films have a higher resistance than bulk material for any current passing through them, due to their large interface to volume ratio and their many defects – predominantly grain boundaries [10,11] – when compared to bulk material. These characteristics cause electrons passing through the thin film to be scattered and slowed down, reducing the conductivity and increasing the resistance of the thin film due to structural properties that are not found in the bulk material. Despite the absolute value of resistivity being measured as below the bulk value, a clear decrease in resistivity can be seen when comparing the four point measurements after heating to different temperatures.

Figure 6.9**(a)** shows the *in situ* resistance, the bulk resistivity and the *ex situ* measured resistivity with increasing heating duration. The lowest value of the thin film resistivity is reached after 12 minutes of heating. Images 6.9**(b-d)** show the development of the thin film morphology that correlates with the *ex situ* measured resistivity values. The advancing dewetting behavior restricts the cross section of the thin film and increases the resistivity after longer durations of heating.

As can be seen in figure 6.9 the four point measurements show an improvement in resistivity with longer heating duration until the counteracting morphology change due to dewetting increases the resistivity again. While some of the absolute values of the four point measurements are below the bulk resistivity – and therefore include a systematic error – the deviation from the bulk value is in the range of the deviation between measurements (as seen in figure 5.14 and

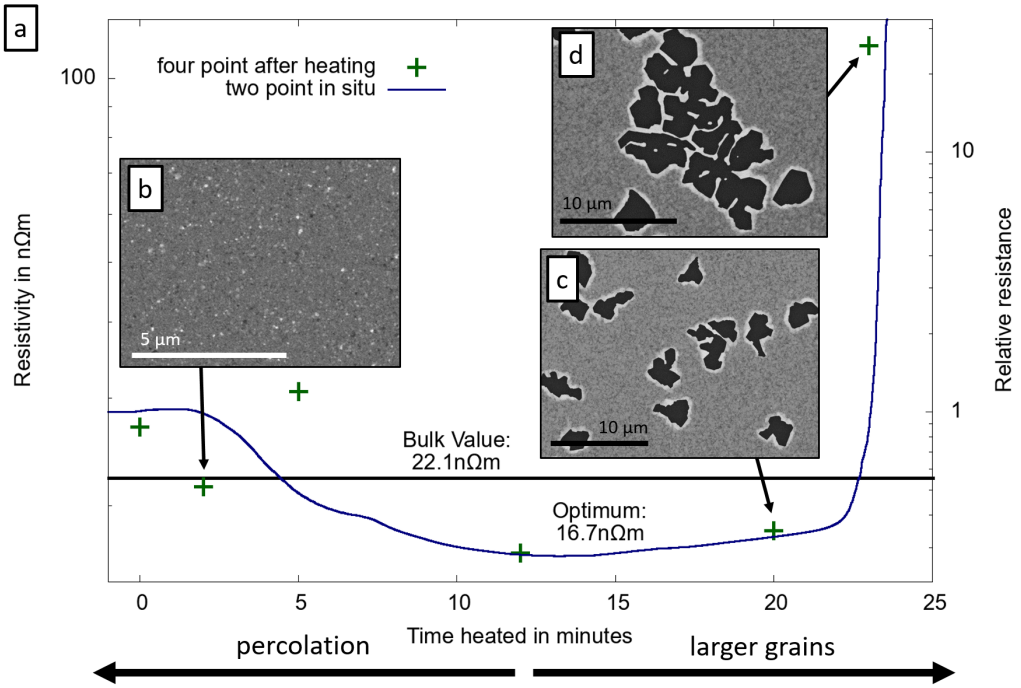

Figure 6.9: Resistivity measurement after heat treatment and correlating SEM images. ***(a)****: In situ resistance measurement and ex situ resistivity measurement.* ***(b)****: SEM image of the sample heated to* 76 °C*. The film has not changed much from the as deposited state and is continuous.* ***(c)****: Image of the thin film heated to* 650 °C*. Large holes are visible but the film is still continuous and can conduct electricity.* ***(c)****: The sample heated to* 698 °C *shows large holes and is partially dewetted enough to no longer carry electricity through parts of the thin film. This increases the resistance of the sample.*

figure B.1 that are used to determine the exact resistivity of the as deposited thin film) and an improvement relative to the resistivity of the untreated thin film can be seen. This improvement in conductivity is also supported by the good agreement of the *in situ* two point measurement with the *ex situ* four point measurement.

Picking apart the equation to calculate the resistivity value (introduced with equation 2.4 and shown again as equation 6.1) as shown in equation 6.2, we can see that there are only three parts that influence the end result – the resistance value, probe placement and shape factor.

$$\rho = \frac{U}{I} \cdot \frac{2\pi}{\ln \frac{r_{31} r_{24}}{r_{34} r_{21}}} \cdot t \cdot C(shape) \tag{6.1}$$

$$\rho = \text{resistance} \cdot (\text{probe placement}) \cdot (\text{shape factor}) \tag{6.2}$$

where :

r_{AB} = the distance between points A and B

$C(shape)$ = correction factor for thin film shape, found in literature

The resistance is determined by the fit of a line to the sweep of the four point measurement. This fit has a R^2 value of 0.924 for the measurement of the wafer heated to 76 °C and more than 0.973 for all other samples. The first correction is for the placement of the probes relative to each other on the thin film and determined mathematically [33]. The second factor is accounting for the limited size of the wafer and can be found in literature [34]. Both of theses corrections are based on one important assumption however: that the size of the thin film relative to the probe spacing is large. While this is the case when determining the resistivity of the untreated thin film, it is no longer true when measuring the resistance after heat treatment. There is less space on the heated samples to place the probes, because the samples had to be cut – from a square with a side length of more than 20 mm to a side length of 6 mm – to fit into the crucible of the heating stage. This limitation forces the probe placement to come closer to the edges of the thin film than the correction factors can account for and an error is introduced.

Despite the absolute values of the *ex situ* resistivity values being measured as below the bulk resistivity, the resistivity values are in relative accordance with each other as well as the *in situ* resistance measurement. This proves the reliability of the two point measurement to give an insight into the thin film properties while heating. With the *in situ* measurement the change in resistivity is accurately represented once the contact paste has fully cured and with very simple methods a direct insight into the thin film development can be gained.

Several ways are available to improve the accuracy of the electrical measurements. Better tooling and thinner wires allow a more precise placement of the contact points on the wafer. Similarly, a bigger wafer size would achieve the same effect on the probe spacing relative to the edge of the wafer. This could be achieved with a large hot plate that is properly insulated. Placing the contact points closer together and nearer to the center of the sample minimizes errors that are due to the measurement system. A heating stage with four electrical contacts can track the resistivity *in situ* during the heat treatment and remove the need for a correlation between the *in situ* measured resistance and the *ex situ* determined resistivity as was done in this work. This improves the reliability of the results.

An optimally conductive film has a very large grain size, as grain boundaries increase the resistivity [70, 71, 72, 73]. In this work an improvement in conductivity is visible when heating the thin film as well. This can be correlated with the increasing grain size, as seen in figure 6.10. The resistivity decreases from the measurement of the as deposited state to a lower value after 2 minutes of heating and an optimal value after 12 minutes of heating. The measurement after 20 minutes of heating shows a reduced resistivity when compared to the as deposited state, but a higher resistivity when compared to the optimal state, as the first influences of dewetting show their effect. Despite the measurement at 23 minutes showing the biggest grain size – and therefore minimizing the influence of these defects on the resistivity value – the resistivity is much higher than the measurements of the samples heated to lower temperatures. This is because the progressed dewetting behavior cuts off enough material of the thin film to counteract the improvement due to grain boundary removal by decreasing the cross sectional area that can conduct electricity. These counteracting phenomena – grain boundary removal due to grain growth and cross sectional area reduction due to dewetting – make it difficult to separate their respective influences at later stages of heating.

Figure 6.11 shows BSE SEM images of the samples heated for 2 minutes, 12 minutes and 23 minutes (insets 6.11**(b)**, 6.11**(c)** and 6.11**(d)**, respectively),

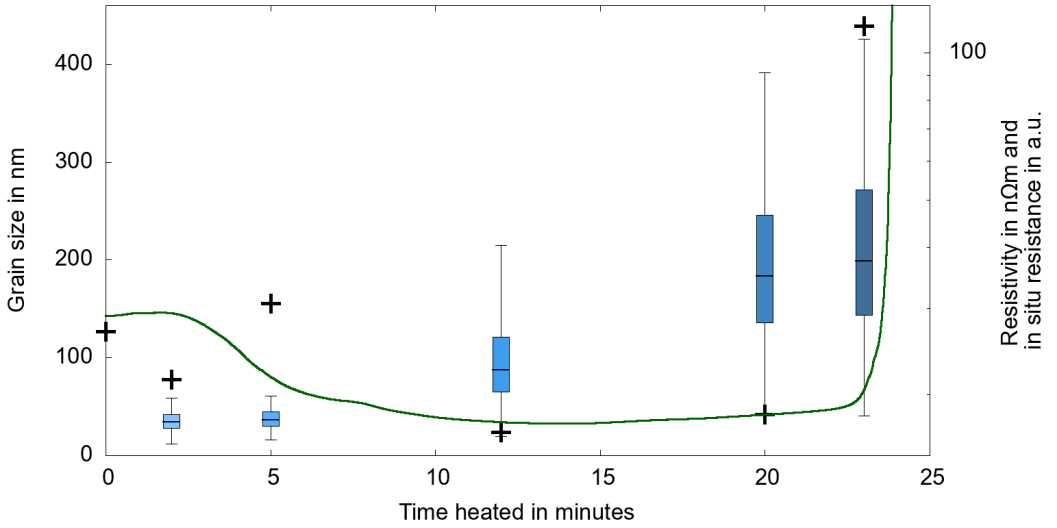

Figure 6.10: In situ resistance, ex situ resistivity and ex situ grains size measurements. The grain size increases with increasing temperature while the resistance decreases. At very high temperatures the dewetting effect reduces the cross section of the thin film and the resistance increases.

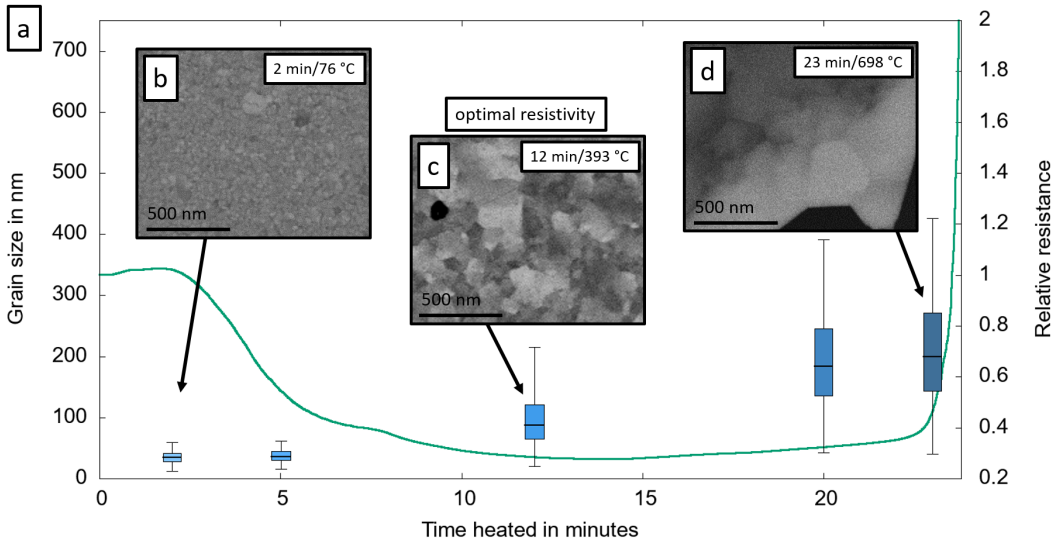

*Figure 6.11: Development of the grain size during heating, together with corresponding BSE images. **(a)**: Plot of the grain sizes and a reference curve of in situ measured resistance. **(b-d)**: BSE images after heating for 2, 12 and 23 minutes. Inset **(c)** shows the thin film in the state of minimal resistivity.*

as well as the grain size values and the *in situ* resistance measurement as reference (figure 6.11**(a)**). The thin film heated to 76 °C shows the small grains produced in the deposition process. They had no time or sufficiently high temperature to agglomerate yet and lead to a significant increase in resistivity due to electron scattering at the many grain boundaries [10, 11, 72]. The optimal conductivity is reached after heating to 393 °C and the corresponding microstructure is shown in figure 6.11**(c)**. The film shows the initial stages of hole formation and has much larger grains than the sample heated to 76 °C. It is still continuous in all parts and has the highest electrical conductivity of all samples measured. Figure 6.11**(d)** shows the microstructure of the sample heated to 698 °C. Despite further grain growth the reduced area coverage counteracts the gain in conductivity and causes the resistivity to rise.

Of special interest is the sample heated to 393 °C, which resulted in the lowest resistivity after cooling the sample again. In order to understand the influence of the heat treatment and grain size this sample will be further analysed.

There are no big holes at this stage of the heating process that would decrease the cross sectional area that can conduct electricity. Some small holes have formed that mark the beginning of the dewetting process. An example of the surface of the thin film can be seen in figure 6.12. The image recorded in the light microscope (image 6.12**(a)**) shows no difference when compared to the thin film in the as deposited state. When inspecting the gold layer in the SEM the impact of the heat treatment becomes apparent. The thin film has started to form holes that can be found throughout the sample (image 6.12**(b)**) but which are small in size (image 6.12**(c)**). A change in grain size is also apparent and the line intersect method confirms a growth of the average grain from 38 nm from the previous measurement after 5 minutes of heating to 102 nm at the resistivity minimum. A representative grain is marked and provided with a scale bar in image 6.12**(d)**.

The grain size is an important aspect next to the absence of large holes. The larger the grains are, the less grain boundaries can scatter the electrons and the higher the conductivity of the thin film [10, 11]. A grain size distribution of the wafer with the lowest resistivity can be seen in figure 6.13. While the thin

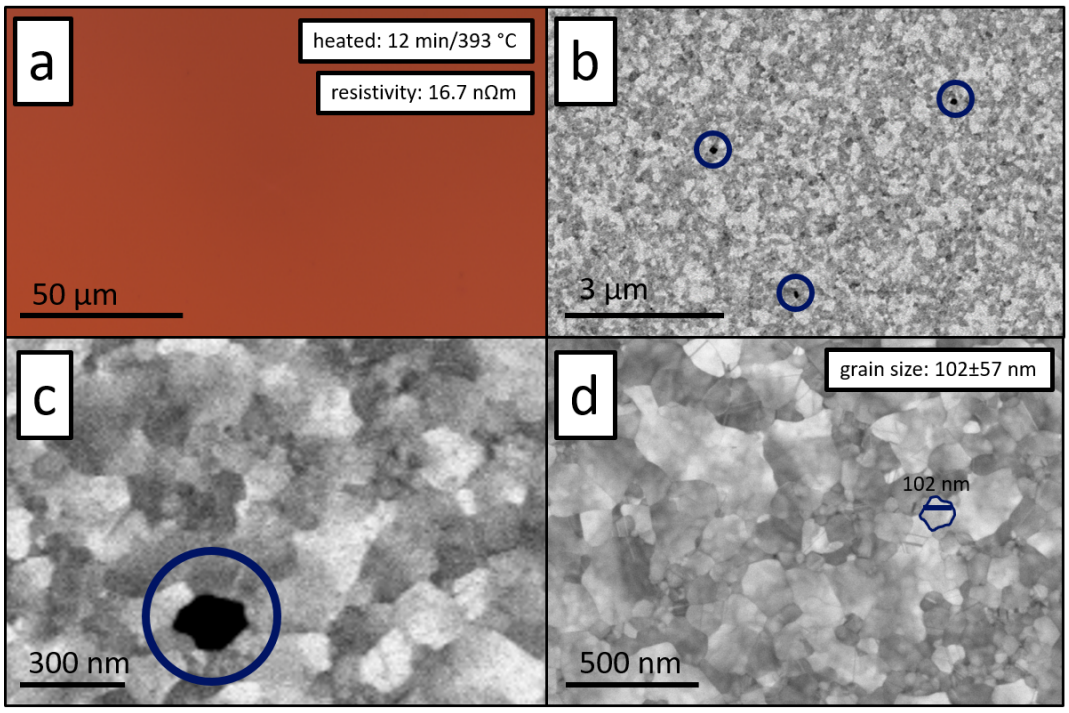

Figure 6.12: Optimum sample heated to 393 °C. ***(a)****: In situ light microscope image. No holes are visible.* ***(b)****: Overview of the thin film in the SEM. Holes (marked by circles) are rare at this stage in the dewetting process.* ***(c)****: Image of a single hole with high magnification. No fingering can be seen, the hole is still roughly circular.* ***(d)****: Continuous thin film showing the grain size after heating to* 393 °C. *An average grain is marked and provided with a scale bar.*

films heated to higher temperatures show even larger grains, the area coverage is decreased for those samples and the reduced cross sectional area works against the improvements of conductivity that are due to the increased grain size. This effect is not visible for the wafer with the least resistivity as there are no big holes formed yet.

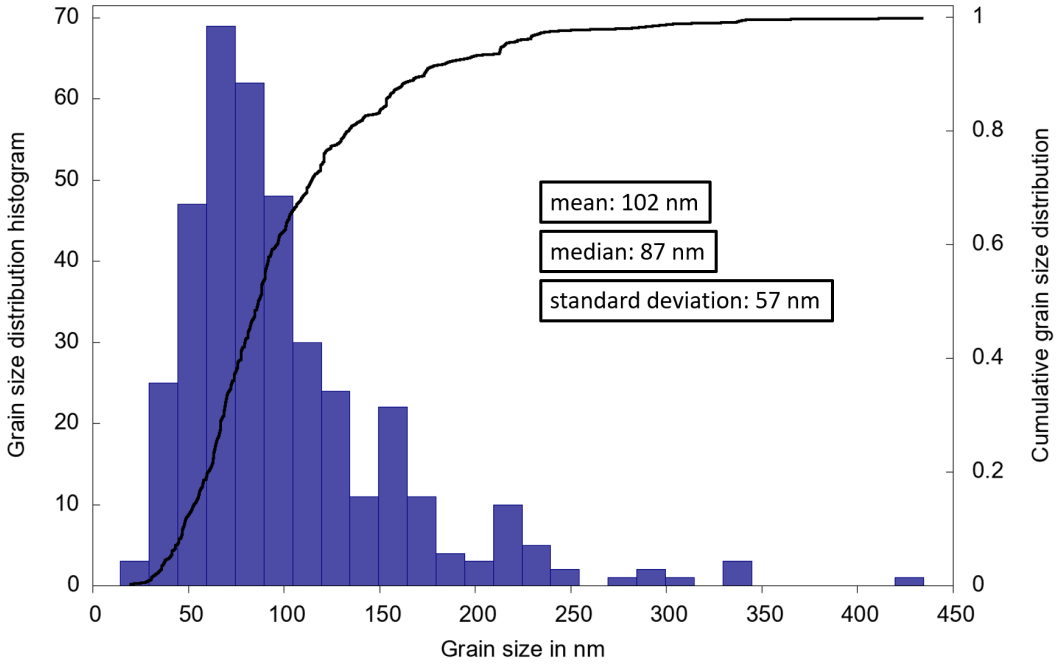

Figure 6.13: Grain size distribution of the thin film in the optimum state.

7 Summary and conclusion

In this work we looked at many different characteristics of thin films, their interactions and their development during heating. These separate influences are summed up and a conclusion formed for every investigated thin film property.

Using *in situ* light microscopy, the area coverage of a thin film is evaluated during heating while at the same time the electrical resistance in measured. To gain a minimal resistivity value, the substrate has to be covered in full, but a tradeoff can be reached if higher transmissivity is required.

The number of grain boundaries, and therefore the grain size, plays an important role in determining the resistivity of thin films [10, 11]. Grain size also increases with increasing temperature and heating duration [82]. The same effect of grain growth during the heat treatment was found in this work, as well as a correlation between grain size and resistivity. The conductivity improves until the counteracting effect of the reduced area coverage due to dewetting overcompensates the gain in conductivity due to growing grains. The larger the grains can be made in a continuous film, the lower the resistivity can get.

The thin films showed a strong alignment towards the [1 1 1] direction in the as deposited state. After the heat treatment this alignment was further improved. As there was no significant change in grain orientation observed in this work, the influence of the type of grain boundaries could not be investigated further.

In situ measured resistance shows a characteristic development during heating, with only slight variations occurring between the different samples. The least resistance was measured after heating to 393 °C within 12 minutes. Since the two point measurement that is used to determine the *in situ* resistance includes parasitic resistances from the contact points and the wires, a four point resistivity measurement is required to remove these influences. Nevertheless, the relative change in thin film resistivity is accurately represented by the simpler two point measurement.

Before and after heating the resistivity of the thin film was determined with

a four point measurement. The resulting resistivity and sheet resistance values correspond well to the measured *in situ* resistance after more than 10 minutes of heating – once the contact paste that is used to connect the sample in the heating stage is fully cured. The absolute values reported by this measurement are in the range of resistivity values for bulk gold as given in literature [66, 67, 68], and – more importantly – follow the *in situ* resistance measurement.

In summary this work demonstrates a direct correlation between the electrical properties of thin films and their microstructural evolution during heating. The interplay between grain coarsening and solid-state dewetting leads to first a reduction in resistance followed by a sharp increase. with the here presented *in situ* approach, the optimal heating time for a target resistance can be chosen. We expect that future developments also including the optical properties may further accelerate the rapid development of thin films with tailored properties.

8 Outlook

This work touches on a lot of different properties of thin films and thin film development under temperature influence. Aside from studying every one of these properties in detail there are many further topics one can take a closer look at.

The E-Beam was used to deposit the thin films because it provides a fine grain structure, which allows the study of the development of the grain sizes. There are other thin film deposition techniques available, however. Sputtering works by using accelerated plasma ions to eject material from a target metal which is then deposited on the substrate. As well as providing many parameters in the deposition process, sputtering also leads to a different thin film structure than evaporation and condensation of a metal. For example, the adhesion of the deposited layer is much stronger, because the impinging atoms have more energy to bond to the underlying substrate and the grain size in the as deposited state is bigger, because the deposited atoms can rearrange into bigger grains thanks to their high energy [25].

Silicon oxide and silicon nitride are good substrates for electric measurements, as these materials are not conductive themselves. Other materials can be used, such as polymers for testing the flexibility of the deposited thin film [85]. The interface between the thin film and the substrate plays an important role in the resistivity and is one contributing factor that increases the thin film resistivity above the bulk value [27]. Changing the substrate can influence the thin film structure, especially the interface and grain structure [86].

As can be seen in the SEM pictures, the created holes and remaining material do not form a perfect or regular net. Instead a lot of material is left as islands and does not contribute to the conductivity of the remaining thin film. One step to improve this drawback is to use a prepatterned substrate. Such a surface would provide local changes in bonding energy to the atoms in the deposited thin film, which will then dewet preferably at the prepared locations. Using this technique, a more consistent pattern of holes and material bridges can be created, and

therefore the amount of film that remains as islands can be reduced [9, 65, 87]. If no material is cut off from the current conducting path, the resistivity of the partially dewetted thin film will only increase minimally. By tuning the remaining morphology, the transparency can be optimized together with the conductivity, potentially resulting in flexible, transparent electrodes.

The thin film thickness used in this thesis was limited to 20 nm for the *in situ* experiments. A residual area coverage of no less than 70 % while still conducting electricity does not allow enough light to pass through for an efficient transparent electrode. One method to increase the transparency next to prepatterning is the deposition of thinner metal films. The less material the light has to pass through, the less light is attenuated and the more light can reach through the thin film. In literature, thin films with a thickness as low as 2 nm are investigated to produce transparent, conductive electrodes [8, 12, 88].

In this work, gold was used as the thin film material, because it does not oxidize over time. However, gold would not be an economic material to use in large quantities. It is therefore important to study different materials and their behavior during heating. Copper is used a lot in electronic applications due to its good conductivity and is therefore an interesting subject for these experiments. We already performed preliminary experiments with copper instead of gold. The resulting thin film is continuous and conducts electricity, but oxidizes in air and especially at higher temperatures. The thin film has to be treated carefully from deposition to dewetting in order to prevent the loss of conductivity due to oxide formation. When heating the copper thin film in ambient air without protective atmosphere, the thin film undergoes oxidation, first forming red Cu_2O and later blue CuO. The development can be seen in figure 8.1. It is necessary to prevent the formation of copper oxides to provide good conductivity [89].

A constantly increasing temperature was used when heating the samples in order to guarantee a dewetting of the thin film. Due to the dependence on temperature, the speed with which a thin film dewets increases exponentially with increasing temperature [90]. If the exact temperature is known at which the thin film decomposes reasonably quickly, an isothermal experiment, in which the tem-

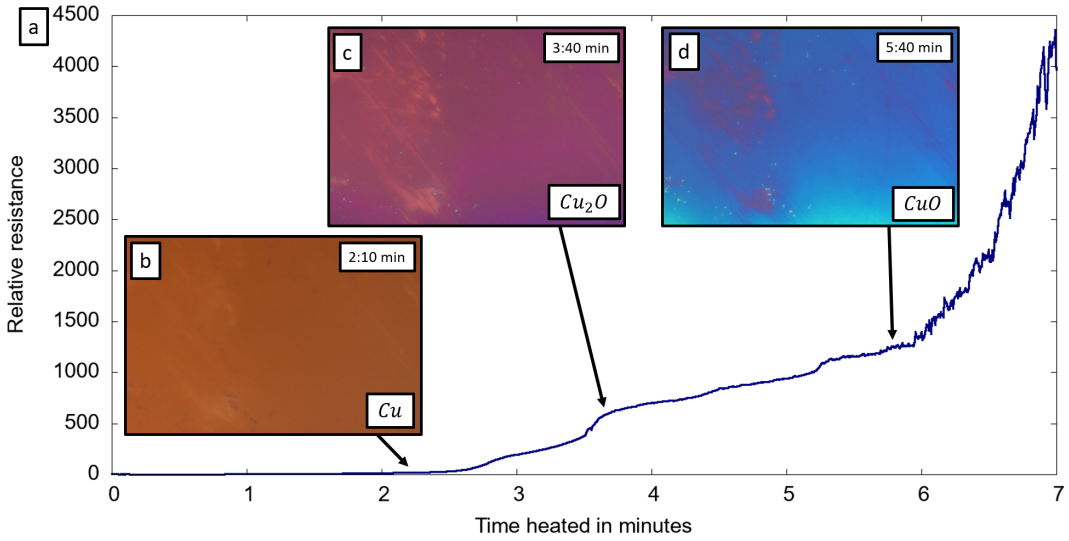

Figure 8.1: Development of a copper thin film when heated. ***(a)****: Relative change in resistance during heating. Oxidation reduces the conductivity of the thin film.* ***(b-d)****: The changing appearance of the copper thin film, from the brown color of the deposited copper to the red colors of* Cu_2O *and the blue appearance of the* CuO*.*

perature is raised quickly and then held constant, would improve the real world relevancy of the experiment. Many other works on the topic of solid-state dewetting use isothermal heating [9, 64, 90].

Because of the limitations of the heating stage only a two point measurement during heating was possible. This merely allows for a measurement of the resistance of the whole system, including contact points and contact wires. To measure the resistivity or sheet resistance of the thin film system *in situ*, a stage with four contact points is necessary. An *in situ* four point measurement would allow the direct and precise electrical characterisation of the thin film during heating and while the process of dewetting is taking place.

Appendix

A A note on sheet resistance and resistivity

In this work, I almost exclusively used the measure of resistivity to compare the thin films and quantify their electrical properties. This is in line with a lot of papers on the subject of fundamental physical properties of materials (e.g. [66, 70, 71]), as the resistivity is one such property. Many works on transparent electrodes however use sheet resistance instead of resistivity to determine the quality of the electrodes. Since many alternatives to thin film electrodes, like nanowire [6, 15], nanotrough [85] and connected particle networks [91] do not have a characteristic thickness, the intrinsic resistivity of the used material can not be directly converted to sheet resistance and is of no special interest. For thin films, the two properties can be easily transformed into each other with the equation 2.5:

$$R_{sq} = \frac{\rho}{t} \tag{1}$$

$$\begin{aligned} &where: \\ &R_sq = \text{thin film sheet resistance} \\ &\rho = \text{thin film resistivity} \\ &t = \text{thin film thickness} \end{aligned}$$

As this work focuses on the optimal treatment of thin films, the intrinsic property is of more interest and was therefore chosen to keep a consistent unit throughout the work. It should be pointed out, however, that the resistivity for the partially dewetted film does not increase as is shown in figure 5.17. Instead this value represents the resistivity of a 20 nm thin film with the same sheet resistance as the partially dewetted sample. The resistivity can not account for the thin film morphology changes.

B Determining the exact resistivity

While the plot shown in figure 5.14 was not used to determine the exact value of the resistivity for the untreated film, it shows how the resistivity of the thin films

with a thickness of 20 nm that were used in this work does not deviate strongly from the linear best fit. This means that films with such a low thickness do not show an abnormally high resistivity due to uneven film deposition.

In order to calculate the thin film resistivity, two correction factors are needed which I was unaware of when performing the first measurement. One is to correct for probe placement not in a straight line, as is shown in the difference between equation 2.3 and equation 2.4. This correction is purely mathematical and, given the exact probe positions, can be determined perfectly [33]. Another correction factor needed to calculate accurate thin film resistivities is to correct for the shape of the wafer. The equations used to calculate the resistivity from the resistance determined in the four point measurement are derived with the assumption that the thin film is infinitely large, compared to the probe spacing [32]. In real world applications this is never the case, but for large wafers and close probe spacing, the assumption is a good approximation. Since this is not the case for the measurements performed in this work, the correction factors found in literature have to be applied [34].

Another experiment was performed and the correction factors applied for every measurement. The results can be seen in figure B.1. Only thin films with a thickness of 80 nm, 100 nm and 120 nm were used. The best fit through this data results in the resistivity value of $(26.92 \pm 0.74)\,\mathrm{n\Omega\,m}$ mentioned in chapter 5.

When determining the resistivity after heat treatment, the limited space on the wafer is further restricted by the remaining contacts of the *in situ* two point measurement. In order to be able to apply the correction factors found in literature, a rectangular film is needed [33, 34]. This was achieved by scratching a rectangular perimeter in the remaining thin film, into which the contacts are placed. The experiment was performed under a stereo microscope in order to determine the exact probe placement.

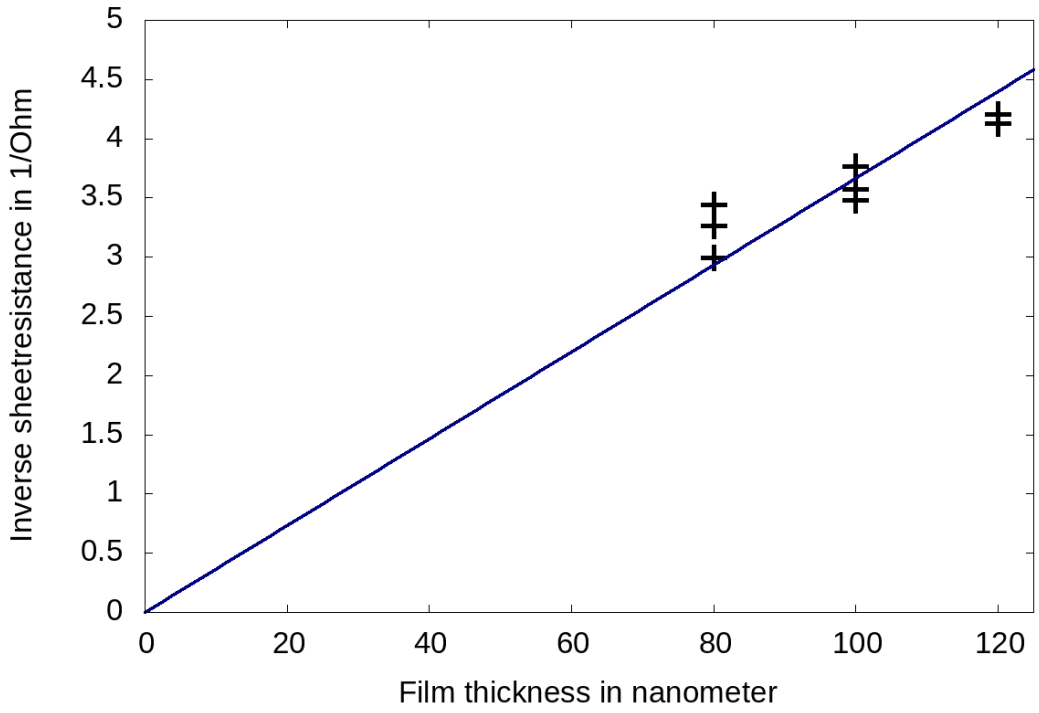

Figure B.1: The points used to determine the exact resistivity of the deposited thin film together with a linear best fit. The points were corrected to account for the increase in measured sheet resistance due to wafer shape and probe placement [33, 34]

List of figures

List of tables

Bibliography

[1] N. Settera et al. Ferroelectric thin films: Review of materials, properties, and applications. *Journal of Applied Physics*, 100, 2006.
— Cited on page 1.

[2] Y. Fu et al. Tini-based thin films in mems applications: a review. *Sensors and Actuators*, A(112):395–408, 2004.
— Cited on page 1.

[3] D. Tyler McQuade et al. Conjugated polymer-based chemical sensors. *Chemical Reviews*, 100:2537–2574, 2000.
— Cited on page 1.

[4] A. Stadler. Transparent conducting oxides — an up-to-date overview. *Materials*, 5(4):661–683, 2012.
— Cited on page 1.

[5] K.Saranya et al. Developments in conducting polymer based counter electrodes for dye-sensitized solar cells – an overview. *European Polymer Journal*, 66:207–227, 2015.
— Cited on page 1.

[6] J.-Y. Lee et al. Solution-processed metal nanowire mesh transparent electrodes. *Nano Letters*, 8(2):689–692, 2008.
— Cited on pages 1, 4, and 81.

[7] K. Ellmer. Past achievements and future challenges in the development of optically transparent electrodes. *Nature Photonics*, 6:809–817, 2012.
— Cited on page 1.

[8] G. Golan A. Axelevitch, B. Gorenstein. Investigation of optical transmission in thin metal films. *Physics Procedia*, 32:1–13, 2012.
— Cited on pages 1 and 78.

[9] C.V. Thompson. Solid-state dewetting of thin films. *Annual Review of Material Research*, 42:399–434, 2012.
— Cited on pages 1, 5, 6, 7, 46, 78, and 79.

[10] A.I. Olivia J.M. Camacho. Surface and grain boundary contributions in the electrical resistivity of metallic nanofilms. *Thin Solid Films*, 515(4):1881–1885, 2006.
— Cited on pages 1, 65, 67, 72, and 75.

[11] T. Sun et al. Classical size effect in oxide-encapsulated cu thin films: Impact of grain boundaries versus surfaces on resistivity. *Journal of Vacuum Science & Technology A*, 26:605–609, 2008.
— Cited on pages 1, 65, 67, 72, and 75.

[12] V.Pruneri S. Ghosh, T.L. Chen. High figure-of-merit ultrathin metal transparent electrodes incorporating a conductive grid. *Applied Physics Letters*, 96(041109), 2010.
— Cited on pages 1 and 78.

[13] D. Infante et al. Durable, superhydrophobic, antireflection, and low haze glass surfaces using scalable metal dewetting nanostructuring. *Nano Research*, 6(6):429–440, 2013.
— Cited on page 1.

[14] A. Aharony D. Stauffer. *Introduction to Percolation Theory*. Taylor & Francis, 2 edition, 1994.
— Cited on page 4.

[15] P. Lee et al. Highly stretchable and highly conductive metal electrode by very long metal nanowire percolation network. *Advanced Materials*, 24(25):3326–3332, 2012.
— Cited on pages 4 and 81.

[16] X. Yu C.H. Liu. Silver nanowire-based transparent, flexible, and conductive thin film. *Nanoscale Research Letters*, 6(75), 2011.
— Cited on page 4.

[17] T.J. McCarthy L. Gao. Wetting 101°. *American Chemical Socitey*, 25(24):14105–14115, 2009.
— Cited on page 5.

[18] D. Bonn et al. Wetting and spreading. *Reviews of Modern Physics*, 81:739–805, 2009.

— Cited on page 5.

[19] A. Kosinova et al. The role of grain boundary sliding in solid-state dewetting of thin polycrystalline films. *Scripta Materialia*, 82:33–36, 2014.
— Cited on page 5.

[20] R.V. Zucker et al. A model for solid-state dewetting of a fully-faceted thin film. *Comptes Rendus Physique*, 14(7):564–577, 2013.
— Cited on page 5.

[21] S.A. Safran D.J. Srolovitz. Capillary instabilities in thin films. ii. kinetics. *Journal of Applied Physics*, 60:255–260, 1986.
— Cited on page 7.

[22] Lord F.R.S. Rayleigh. On the instability of jets. *Proceedings of the London mathematical society*, 10:4–13, 1878.
— Cited on page 7.

[23] A. Biwas et al. Advances in top-down and bottom-up surface nanofabrication: Techniques, applications and future prospects. *Advances in Colloid and Interface Science*, 170:2–27, 2012.
— Cited on page 7.

[24] J. Valdez. *Atomic Layer Deposition (ALD): Fundamentals, Characteristics and Industrial Applications*. Nova Science Publishers, 2015.
— Cited on page 7.

[25] H.Kotera K. Wasa, I. Kanno. *Handbook of Sputter Deposition Technology: Fundamentals and Applications for Functional Thin Films, Nano-Materials and MEMS*. William Andrew, 2012.
— Cited on pages 7 and 77.

[26] K.S.S. Harsha. *Principles of physical vapor deposition of thin films*. Elsevier, 1 edition, 2006.
— Cited on pages 7 and 8.

[27] K. Fuchs. The conductivity of thin metallic films according to the electron theory of metals. *Proceedings of the Cambridge Philosophical Society*, 34:100–108, 1937.
— Cited on pages 7, 67, and 77.

[28] S.B. Soffer. Statistical model for the size effect in electrical conduction. *Journal of Applied Physics*, 38(4):1710–1715, 1967.
— Cited on page 7.

[29] M. Shatzkes A.F. Mayadas. Electrical-resistivity model for polycrystalline films: the case of arbitrary reflection at external surfaces. *Physical Review*, B(1):1382–1389, 1970.
— Cited on pages 7 and 67.

[30] G.S. Ohm. *Die galvanische Kette, mathematisch bearbeitet*. 1827.
— Cited on page 8.

[31] O. Aluf. *Optoisolation Circuits: Nonlinearity Applications in Engineering*. World Scientific, 2012.
— Cited on page 8.

[32] F.M. Smits. Measurement of sheet resistivities with the four-point probe. *Bell Systems Technical Journal*, 37:711–718, 1958.
— Cited on pages 11 and 82.

[33] S. Yilmaz. The geometric resistivity correction factor for several geometrical samples. *Journal of Semiconductors*, 36(8), 2015.
— Cited on pages 11, 69, 82, and 83.

[34] H. Topsoe. Geometric factors in four point resistivity measurement. *Haldor Topsoe Semiconductor Division*, pages 53–56, 1966.
— Cited on pages 11, 69, 82, and 83.

[35] M. Volgger. Lichtmikroskopie Theorie und Anwendung. https://www.univie.ac.at/mikroskopie/pdf/lichtmikroskopie.pdf, July 27th 2020.
— Cited on pages 13 and 14.

[36] J. Walker D. Halliday, R. Resnick. *Fundamentals of Physics*. Wiley, 9 edition, 2010.
— Cited on page 15.

[37] Lord F.R.S Rayleigh. Investigations in optics, with special reference to the spectroscope. *The London, Edinburgh, and Dublin Philosophical Magazine and Journal of Science*, 8(49):261–274, 1879.

— Cited on pages 14 and 16.

[38] W. Domke. *Werkstoffkunde und Werkstoffprüfung*. Cornelsen, 10 edition, 1986.
— Cited on page 18.

[39] Linkam TS1200E product information. https://www.linkam.co.uk/s/ts1000-_1200_1500_systems_v14-8blx.pdf, July 6th 2020.
— Cited on pages 19 and 20.

[40] G. Dehm, J. M. Howe, and J. Zweck. *In-situ Electron Microscopy: Applications in Physics, Chemistry and Materials Science*. Wiley, 2012.
— Cited on page 21.

[41] FEI Helios Nanolab 660 dualbeam FIB/SEM. https://www.fei.com/products/dualbeam/helios-nanolab, July 27th 2020.
— Cited on pages 21 and 22.

[42] L. de Broglie. On the theory of quanta, a translation of 'recherches sur la theorie des quanta', 1925.
— Cited on page 22.

[43] B. Hafner. Scanning electron microscopy primer, 2015.
— Cited on page 23.

[44] H. Seiler. Secondary electron emission in the scanningelectron microscope. *Journal of Applied Physics*, 54(11), 1983.
— Cited on page 23.

[45] L. Reimer. *Scanning Electron Microscopy*. Springer, 2 edition, 1998.
— Cited on page 24.

[46] A.J. Schwartz et al. *Electron Backscatter Diffraction in Materials Science*. Springer, 2 edition, 2009.
— Cited on page 25.

[47] W.L. Bragg W.H. Bragg. The reflection of x-rays by crystals. *Proceedings of the Royal Society London*, 88:428–438, 1913.
— Cited on page 25.

[48] EBSD Explained: From data acquisition to advanced analysis. https://nano.oxinst.com/downloads/ebsd-explained, September 4th 2020.

— Cited on page 26.

[49] FEI Titan Themis^3 300. https://www.fei.com/products/tem/themis, July 27th 2020.
— Cited on pages 27 and 28.

[50] H. Kohl L. Reimer. *Transmission Electron Microscopy*. Springer, 5 edition, 2007.
— Cited on pages 27 and 28.

[51] Winter-Vakuumtechnik Beam PVD (HVB 130). https://www.winter-vakuumtechnik.com/produkte/vakuumbeschichtungssysteme/, July 27th 2020.
— Cited on pages 29 and 30.

[52] J. Wirth. Microscopic studies of the aluminium induced crystallization of germanium, 2016.
— Cited on page 30.

[53] C.M. Hell. Korrelative in situ licht- und ex situ elektronenmikroskopie von festphasen-entnetzenden au dünnschichten unter verschiedenen atmosphären, 2015.
— Cited on page 30.

[54] Acheson Silver DAG 1415. https://www.agarscientific.com/acheson-silver-dag-1415-m, July 8th 2020.
— Cited on pages 31 and 55.

[55] PELCO Conductive Gold Paste. https://www.tedpella.com/technote_html/16022tn.pdf, July 8th 2020.
— Cited on pages 31 and 55.

[56] Keithley SMU Datasheet. https://www.tek.com/datasheet/series-2400-sourcemeter-instruments, July 6th 2020.
— Cited on page 32.

[57] OpenCV Website. https://opencv.org, July 6th 2020.
— Cited on pages 37 and 62.

[58] ImageJ Website. https://fiji.sc/, July 6th 2020.
— Cited on pages 38, 53, and 63.

[59] A. Kosinova et al. Mechanisms of solid-state dewetting of thin au films in different annealing atmospheres. *Acta Materialia*, 83:91–101, 2015.
— Cited on pages 40 and 58.

[60] O. Anderoglu et al. Thermal stability of sputtered cu films with nanoscale growth twins. *Journal of Applied Physics*, 103(094322), 2008.
— Cited on page 42.

[61] A. Misra X. Zhang. Superior thermal stability of coherent twin boundariesin nanotwinned metals. *Scripta Materialia*, 66:860–865, 2012.
— Cited on page 43.

[62] K. Lu X.H. Chen, L. Lua. Electrical resistivity of ultrafine-grained copper with nanoscale growth twins. *Journal of Applied Physics*, 102(083708), 2007.
— Cited on page 43.

[63] A.M. Gusak K.N. Tu. *Kinetics in Nanoscale Materials*. Wiley, 2014.
— Cited on page 44.

[64] R. Spolenak M. Müller. Dewetting of au and aupt alloy films: A dewetting zone model. *Journal of Applied Physics*, 113:094301, 2013.
— Cited on pages 44, 65, and 79.

[65] C.V. Thompson D. Kim, A.L. Giermann. Solid-state dewetting of patterned thin films. *Applied Physics Letters*, 95(251903), 2009.
— Cited on pages 46 and 78.

[66] R.A. Matula. Electrical resistivity of copper, gold, palladium, and silver. *Journal of Physical and Chemical Reference Data*, 8:1147–1298, 1979.
— Cited on pages 50, 53, 55, 67, 76, and 81.

[67] R.C. Munoz et al. Surface roughness and surface-induced resistivity of gold films on mica: Application of quantitative scanning tunneling microscopy. *Physical Review B*, 62(7):4686–4697, 2000.
— Cited on pages 50, 53, 67, and 76.

[68] E.J. Menke et al. Lithographically patterned nanowire electrodeposition. *Nature Materials*, 5:914–919, 2006.
— Cited on pages 50, 53, 67, and 76.

[69] G. Kästle et al. Size effect of the resistivity of thin epitaxial gold films.

Physical Reviews B, 70(16):165414, 2004.
— Cited on page 50.

[70] W. Ma et al. Electrical properties and reduced debye temperature of polycrystalline thin gold films. *Journal of Physics D: Applied Physics*, 43, 2010.
— Cited on pages 50, 65, 70, and 81.

[71] P. M. Th. M. van Attekum et al. Influence of grain boundaries and surface debye temperature on the electrical resistance of thin gold films. *Physical Review B*, 29(2):645–651, 1984.
— Cited on pages 50, 65, 70, and 81.

[72] Q.G Zhang et al. Influence of grain boundary scattering on the electrical and thermal conductivities of polycrystalline gold nanofilms. *Physical Review B*, 74:134109, 2006.
— Cited on pages 50, 65, 70, and 72.

[73] J.P. Chauvineau et al. Recrystallization of thin gold films: Influence on their electrical properties. *Journal of Vacuum Science & Technology*, 6(776), 1969.
— Cited on pages 50, 65, and 70.

[74] W.C. Mallard et al. Self-diffusion in silver-gold solid solution. *Physical Review*, 129(2):617–625, 1963.
— Cited on page 55.

[75] A. Herz et al. Solid-state dewetting of au–ni bi-layer films mediated through individual layer thickness and stacking sequence. *Applied Surface Science*, 444:505–510, 2018.
— Cited on page 57.

[76] D.L. Trimm A.E.B. Presland, G.L. Price. Hillock formation by surface diffusion on thin silver films. *Surface Science*, 29:424–434, 1972.
— Cited on page 57.

[77] N. Otsu. A threshold selection method from gray-level histograms. *EEE Transactions on Systems, Man, and Cybernetics*, 9(1):62–66, 1979.
— Cited on page 61.

[78] C.V. Thompson A.L. Giermann. Solid-state dewetting for ordered arrays of crystallographically oriented metal particles. *Applied Physics Letters*,

86(121903), 2005.
— Cited on page 65.

[79] Y.J. Oh et al. Cobalt nanoparticle arrays made by templated solid-state dewetting. *small*, 5:860–865, 2009.
— Cited on page 65.

[80] W.K. Choi et al. A combined top-down and bottom-up approach for precise placement of metal nanoparticles on silicon. *small*, 4:330–333, 2008.
— Cited on page 65.

[81] P.W. Voorhees. The theory of ostwald ripening. *Journal of Statistical Physics*, 38:231–252, 1985.
— Cited on page 65.

[82] F. Niekiel et al. Texture evolution and microstructural changes during solid-state dewetting: A correlative study by complementary in situ tem techniques. *Acta Materialia*, 115:230–241, 2016.
— Cited on pages 65 and 75.

[83] S. Bahamondes et al. Resistivity and hall voltage in gold thin films deposited on mica at room temperature. *Applied Surface Science*, 332:694–698, 2015.
— Cited on page 67.

[84] F. Cemin et al. Low electrical resistivity in thin and ultrathin copper layers grown by high power impulse magnetron sputtering. *Journal of Vacuum Science & Technology A*, 34, 2016.
— Cited on page 67.

[85] H. Wu et al. A transparent electrode based on a metal nanotrough network. *Nature Technology*, 8:421–425, 2013.
— Cited on pages 77 and 81.

[86] M. Ohring. *Material science of thin films*. 2 edition, 2002.
— Cited on page 77.

[87] et al. M. Theuring. Laser perforated ultrathin metal films for transparent electrode applications. *Optics Express*, 23(7):254–262, 2015.
— Cited on page 78.

[88] et al. B. O'Connor. Transparent and conductive electrodes based on unpat-

terned, thin metal films. *Applied Physics Letters*, 93(223304), 2008.
— Cited on page 78.

[89] et al. D.L.S. Valladares. Crystallization and electrical resistivity of cu_2o and cuo obtained by thermal oxidation of cu thin films on sio_2/si substrates. *Thin Solid Films*, 520:6368–6374, 2012.
— Cited on page 78.

[90] F. Niekiel et al. The process of solid-state dewetting of au thin films studied by in situ scanning transmission electron microscopy. *Acta Materialia*, 90:118–132, 2015.
— Cited on pages 78 and 79.

[91] S. Magdassi M. Layani, R. Berman. Printing holes by a dewetting solution enables formation of a transparent conductive film. *ACS Applied Materials & Interfaces*, 6(21):18668–18672, 2014.
— Cited on page 81.

Acknowledgment

First of all, I would like to thank Prof. Erdmann Spiecker for the opportunity to work on highly interesting topics at his Institute of Micro- and Nanostructure Research and to gain a lot of hands-on experience in electron microscopy in the process, first as a Hiwi and then within the scope of my Bachelor thesis. Likewise I appreciate the chance to get to know the academic work environment and especially to already attend and present at a conference as a student.

I would also like to thank Lilian Vogl for supervising this thesis, for always being available for questions and for her support throughout my work as a Hiwi.

A big thank you to Peter Denninger for his help a the SEM and the EBSD measurements and Johanna Schubert for her help at the EBeam. Thanks to Peter Schweizer for his valuable input and fruitful discussions. And thank you to Sebsatian Krauß for performing the AFM measurements.

I would also like to thank my fellow Hiwis for help with immediate questions and especially Nicolas Karpstein and Marco Moninger for their help with LaTeX when writing this thesis.

Finally I acknowledge the support of the Center for Nanoanalysis and Electron Microscopy (CENEM) as well as the GRK 1896 "In situ Microscopy".

Eidesstattliche Erklärung

Ich versichere, dass ich die Arbeit ohne fremde Hilfe und ohne Benutzung anderer als der angegebenen Quellen angefertigt habe und dass die Arbeit in gleicher oder ähnlicher Form noch keiner anderen Prüfungsbehörde vorgelegen hat und von dieser als Teil einer Prüfungsleistung angenommen wurde. Alle Ausführungen, die wörtlich oder sinngemäß übernommen wurden, sind als solche gekennzeichnet.

Erlangen, den ....

Julian Kauth